UNIVERSIDAD DE CONCEPCIÓN
FACULTAD DE CIENCIAS FÍSICAS Y MATEMÁTICAS

HONG-OU-MANDEL INTERFERENCE IN MULTIPORT PHOTONIC DEVICES

Por: Letícia Lira Tacca

Tesis presentada a la Facultad de Ciencias Físicas y Matemáticas de la Universidad de Concepción para optar al grado académico de Doctorado en Ciencias Físicas con Mención en Óptica Cuántica Experimental.

Abril de 2026
Concepción, Chile

Profesor Guía: Dr. Stephen Patrick Walborn

LA LUZ

Por los aires anda la Luz
que para verte, hijo, me vale.
Si no estuviese, todas las cosas
que te aman no te mirasen;
en la noche te buscarían,
todas gimiendo y sin hallarte.

Ella se cambia, ella se trueca
y nunca es cosa de saciarse.
Amar el mundo nos creemos,
pero amamos la Luz que cae.

La Bendita, cuando nacías,
tomó tu cuerpo para llevarte.
Cuando yo muera y que te deje,
¡síguela, hijo, como a tu madre!

— Gabriela Mistral

" En la búsqueda de la precisión, siempre cabe la posibilidad de descubrir algo inesperado y, en ocasiones, fundamental."

— Serge Aroche, *La Luz Revelada*

A Marisela Herrera

Agradecimientos

Son muchos los nombres de las personas que han pasado por mi vida durante estos últimos años aquí en Chile, todas ellas fundamentales a lo largo de este arduo proceso de doctorado.

En primer lugar, quiero agradecer a mi guía de tesis, Stephen Walborn, de quien siempre recibí apoyo, incentivo y confianza desde el primer día en estos largos cuatro años. Su acogida y sus enseñanzas me permitieron crecer enormemente en este amplio campo de la óptica cuántica experimental. Ha sido un gran honor haber tenido esta oportunidad. También agradezco a Lucas Céleri, mi antiguo supervisor de magíster en la UFG, por haber sido el puente que me llevó a cruzar la cordillera de los Andes para trabajar con Steve. Asimismo, agradezco a los profesores Gustavo Lima, Esteban Sepúlveda y Paulo Souto Ribeiro por todo su apoyo y enseñanzas.

Quiero agradecer profundamente a mis antiguos compañeros de laboratorio, quienes, aunque hoy estén lejos, con mucha paciencia me enseñaron todo lo que sé sobre experimentos con la luz: Santiago Gómez, Ítalo Machuca, Daniel Martínez y Mariana Navarro. Del mismo modo, agradezco a mis actuales y resilientes compañeros de laboratorio: Nelson, Jorge, Javier, Nayda, Felipe, Gustavo y Matías.

En especial, agradezco a Kei Sawada, Jorge Escandón, Adheris Contreras y Sebastián Ayala por ser grandes amigos y mi red de apoyo cuando más lo necesité.

Agradezco a mi familia por su apoyo, amor y paciencia, incluso a la distancia, y a todos los amigos y amigas que hice en este camino de crecimiento.

Agradezco muy especialmente a la persona más especial que tuve la suerte de conocer en este país: Marisela Herrera, quien me brinda amor y compañía cada día, despertando lo mejor de mí. Y a Popi, por supuesto. Nuestra familia es lo más valioso del mundo.

Finalmente, agradezco a la Agencia Nacional de Investigación y Desarrollo (ANID) y al Millennium Institute for Research in Optics (MIRO) por el financiamiento.

Resumen

La interferencia Hong–Ou–Mandel (HOM) es un efecto cuántico fundamental de dos fotones, central en el procesamiento de información cuántica fotónica, con aplicaciones que abarcan desde la computación cuántica hasta las comunicaciones seguras. Esta tesis extiende la interferencia HOM más allá de su formulación estándar de dos modos hacia dispositivos fotónicos multi-puerto, que constituyen una plataforma escalable para fenómenos de interferencia cuántica complejos.

Se revisan los fundamentos teóricos de la interferencia HOM y se analiza su generalización a arquitecturas interferométricas multi-puerto, donde emergen efectos de interferencia de mayor dimensionalidad. Se estudia el papel de la indistinguibilidad de los fotones y el impacto de las imperfecciones experimentales en la visibilidad de la interferencia.

Una contribución experimental central es la demostración de la caracterización del desfase temporal entre núcleos (inter-core skew) con precisión de sub-picosegundos en fibras multicore mediante interferencia HOM. Este resultado establece la interferencia HOM como una herramienta metrológica de alta resolución para cuantificar retardos temporales, con relevancia directa en la optimización de sistemas fotónicos multi-puerto y redes cuánticas basadas en fibra.

Finalmente, se abordan aplicaciones en comunicaciones cuánticas, mediante una breve revisión de la distribución de claves cuánticas independiente de dispositivos (DIQKD), incluyendo avances experimentales, implementaciones basadas en fuentes SPDC y sus limitaciones actuales. También se destacan las conexiones con MDI-QKD, subrayando el papel de la interferencia de dos fotones en protocolos de comunicación cuántica segura.

Esta tesis establece un vínculo entre la interferencia cuántica fundamental, las plataformas fotónicas escalables y las comunicaciones cuánticas, posicionando la interferencia HOM en sistemas multi-puerto como un recurso clave para futuras tecnologías cuánticas.

Abstract

Hong–Ou–Mandel (HOM) interference is a fundamental two-photon quantum effect at the core of photonic quantum information processing, with applications ranging from quantum computing to secure communication. This thesis extends HOM interference beyond its standard two-mode formulation to multiport photonic devices, providing a scalable platform for complex quantum interference.

We revisit the theoretical foundations of HOM interference and analyze its generalization to multiport interferometric architectures, where higher-dimensional interference effects arise. The role of photon indistinguishability and the impact of experimental imperfections on interference visibility are examined.

A central experimental contribution is the demonstration of sub-picosecond inter-core skew characterization in multicore fibers using HOM interference. This work establishes HOM interference as a high-resolution metrological tool for quantifying temporal delays, with direct relevance for the optimization of multiport and fiber-based quantum systems.

Finally, we discuss applications in quantum communication, with a brief review of Device-Independent Quantum Key Distribution (DIQKD), including experimental progress, SPDC-based implementations, and current limitations. Connections to Measurement-Device-Independent QKD (MDI-QKD) are also highlighted, emphasizing the role of two-photon interference in secure quantum protocols.

This thesis connects fundamental quantum interference, scalable photonic platforms, and quantum communication, positioning multiport HOM interference as a key resource for future quantum technologies.

Contents

List of Tables

List of Figures

Chapter 1

Introduction

The phenomenon of quantum interference of light constitutes one of the foundational pillars of modern optics and underlies a wide range of technological applications in quantum information, quantum computation, and quantum metrology [1, 2, 3]. In the classical description, light is treated as an electromagnetic wave. When two waves overlap, their electric fields superpose, leading to constructive or destructive interference in the observed intensity. This superposition gives rise to characteristic fringe patterns with alternating bright and dark regions, as exemplified by the canonical double-slit experiment originally demonstrated by Young [4].

Within the framework of quantum mechanics, light is described as a quantized electromagnetic field, whose elementary excitations are photons. In interference experiments, the relevant description is given in terms of probability amplitudes associated with different, indistinguishable propagation paths. When multiple paths are available, the quantum state of the light field coherently encompasses all such alternatives simultaneously. Interference arises from the superposition of these probability amplitudes, which may add or cancel in close analogy with classical wave interference [5]. Individual detection events occur discretely; however, after many repetitions of the experiment, a statistical distribution emerges that reproduces the expected interference pattern. Although the resulting patterns may closely resemble those observed in the classical regime, their physical interpretation is fundamentally distinct.

In the classical view, interference is an objective physical property of light, arising from the superposition of real, measurable electric and magnetic fields propagating through space, and it is independent of the act of observation. In contrast, quantum interference reflects the coherent superposition of alternative, indistinguishable histories of the system and is intrinsically linked to the measurement process. The availability of which-path information, even in principle, prevents the coherent combination of probability amplitudes and consequently suppresses interference [6]. Thus, in the quantum regime, interference is not merely a property of the field itself but a manifestation of the underlying quantum description and the information accessible through measurement.

A particularly striking manifestation of quantum interference arises in two-photon interference phenomena, where the interference cannot be explained in terms of classical fields. The paradigmatic example is Hong–Ou–Mandel (HOM) interference, in which two indistinguishable photons impinging simultaneously on a balanced beam splitter exhibit a suppression of coincidence detections at the output ports [7]. This effect originates from the destructive interference between two-photon probability amplitudes corresponding to different but indistinguishable detection pathways, and it has no classical analogue. As a result, HOM interference has become a central tool for probing photon indistinguishability, temporal correlations, and coherence properties of quantum states of light [8, 9, 10, 11].

Beyond its fundamental significance, two-photon interference provides a powerful resource for precision metrology in complex photonic systems. In particular, multicore optical fibers (MCFs) exhibit inter-core group delay differences, commonly referred to as inter-core skew (ICS), which arise from residual variations in propagation constants and dispersion among the different cores [12, 13]. Accurate characterization of this skew is essential for a wide range of applications, including space-division multiplexed communications, coherent signal processing, and synchronization of parallel optical channels, where even picosecond-level delays can significantly degrade system performance and compromise coherent and interference-based processes [14, 15, 16]. Interferometric techniques based on quantum interference, and in particular Hong–Ou–Mandel interference, offer a direct and highly sensitive approach to measuring relative delays between optical paths, enabling the precise determination of inter-core skew without requiring absolute timing references. From this perspective, the investigation of HOM interference in MCFs is not only relevant for understanding quantum effects in complex media, but also establishes a novel metrological tool for characterizing and optimizing advanced fiber platforms.

In addition to its relevance for quantum metrology, HOM interference plays a crucial role in quantum communication protocols such as measurement-device-independent quantum key distribution (MDI-QKD) [17, 18], and photonic quantum information processing, where it underpins linear optical quantum computing [19] and high-dimensional protocols [20]. In recent years, increasing attention has been devoted to the investigation of HOM interference in complex photonic platforms, such as multimode and multicore optical fibers, which offer enhanced capacity, scalability, and integration potential [21, 22]. In these systems, additional degrees of freedom, such as spatial modes or distinct fiber cores, introduce new challenges related to mode dispersion, temporal distinguishability, and coherence preservation, while simultaneously enabling novel functionalities.

The investigation of device-independent quantum key distribution (DI-QKD) constitutes a central motivation for the Chapter 5, which is based on an extensive review paper that we published recently [23]. From an experimental standpoint, the implementation of DI-QKD protocols remains highly demanding, as it requires the simultaneous closure of detection and locality loopholes while maintaining high-visibility quantum interference and low-loss transmission. In this context, the Hong–Ou–Mandel effect plays a pivotal role, as it provides a sensitive probe of photon indistinguishability, which is a fundamental resource for generating the high-quality entanglement required in DI-QKD schemes. Moreover, multicore fiber platforms emerge as a promising architecture to address these challenges, enabling stable and scalable distribution of quantum states across multiple spatial modes with intrinsic phase stability and reduced footprint. The interplay between HOM interference and MCF-based implementations thus establishes a concrete experimental pathway toward DI-QKD, motivating a comprehensive review of the state of the art, key limitations, and emerging strategies in this field.

This thesis develops a unified experimental and conceptual framework connecting multicore fiber platforms, precise temporal metrology, and quantum interference phenomena. It begins with the fundamental principles of two-photon interference and the Hong–Ou–Mandel effect in Chapter 2, establishing the central role of photon indistinguishability and timing control. Chapter 3 presents the implementation of Hong–Ou–Mandel interference in multicore fiber platforms, detailing their architecture and the mechanisms that enable controlled two-photon interference across distinct spatial modes. Building upon this foundation, Chapter 4 investigates inter-core skew in multicore fibers as both a limiting factor and a resource, developing measurement and compensation strategies that enable high-visibility interference across spatially multiplexed channels. Finally, in the Chapter 5 the discussion is broadened to device-independent quantum key distribution, where the stringent requirements on interference visibility, synchronization, and loss highlight the relevance of the techniques developed throughout this work. Taken together, the chapters of this thesis demonstrate how advances in fiber-based photonic platforms and precise temporal control can support the realization of robust and scalable quantum communication technologies.

Chapter 2

Theoretical Foundations on Hong-Ou-Mandel Interference

2.1 Introduction

Hong–Ou–Mandel (HOM) interference constitutes one of the most fundamental and experimentally accessible manifestations of multi-photon quantum interference [24, 25, 26]. First demonstrated in 1987 [7], the effect revealed a striking deviation from classical optical behavior: when two indistinguishable photons enter the two input ports of a balanced beam splitter, coincidence detections at the outputs are suppressed [27, 28]. This phenomenon, commonly referred to as photon bunching, arises not from interference of classical electromagnetic fields, but from the coherent superposition of indistinguishable two-photon probability amplitudes [29, 30].

Unlike first-order interference, which can often be interpreted within a classical wave framework, HOM interference is intrinsically a second-order quantum effect [31]. It probes exchange symmetry and the indistinguishability of bosonic particles at the level of joint detection events [32]. The observable quantity, the coincidence probability, directly reflects the overlap of the photons' quantum states across all degrees of freedom, including temporal, spectral, spatial, and polarization modes [33]. In this sense, HOM interference provides an operational measurement of photon indistinguishability and serves as a sensitive diagnostic tool for characterizing single-photon sources and propagation-induced decoherence [34, 35, 36].

Beyond its foundational significance, HOM interference has become a central primitive in photonic quantum information science [37, 38]. The same symmetry-sensitive projection mechanism underlies linear-optical Bell-state measurements [39], entanglement swapping [40], measurement-device-independent quantum key distribution [41], and probabilistic entangling gates in linear optical quantum computing [42]. In quantum communication architectures, two-photon interference between independent sources [43] enables phase-insensitive entanglement generation at remote stations, a key requirement for scalable quantum networks [44].

The objective of this chapter is to establish a rigorous theoretical framework for HOM interference that connects its operator-based quantum description [3], its probabilistic interpretation in terms of detection amplitudes, and its operational role in quantum technologies. Particular emphasis is placed on quantifying partial distinguishability [45], deriving the visibility of the HOM dip [46], and understanding how realistic imperfections, such as temporal delay, spectral mismatch, and decoherence, affect interference contrast [47].

This framework is essential for the analysis of the experimental systems considered in this thesis, where two-photon interference occurs in complex photonic platforms, including multicore optical fibers [48, 49]. In such environments, dispersion, mode-dependent delays, and environmental perturbations introduce nontrivial distinguishability effects that directly impact interference visibility and entanglement fidelity [50]. A precise theoretical treatment of HOM interference therefore provides the foundation for interpreting experimental results and for assessing the feasibility of quantum communication protocols in realistic fiber-based networks.

2.2 Quantum Mechanical Formalism

HOM interference is most naturally described within the framework of quantum optics using the formalism of second quantization [31, 5], where optical fields are represented by mode operators acting on a Fock space [1]. Within this approach, interference phenomena arise from the coherent transformation of multi-photon quantum states under linear optical elements, such as beam splitters.

2.2.1 Optical modes and field operators

We consider two optical modes, labeled a and b, corresponding to the two input ports of a BS. These modes are described by bosonic annihilation and creation operators, $\hat{a}, \hat{a}^\dagger$ and $\hat{b}, \hat{b}^\dagger$, which satisfy the canonical commutation relations [1, 5]

$$[\hat{a}, \hat{a}^\dagger] = 1, \qquad [\hat{b}, \hat{b}^\dagger] = 1, \qquad [\hat{a}, \hat{b}] = [\hat{a}, \hat{b}^\dagger] = 0. \tag{2.2.1}$$

The vacuum state $|0\rangle$ is defined as the state annihilated by all annihilation operators. Single- and multi-photon states are generated through the repeated application of creation operators on the vacuum.

2.2.2 Initial two-photon input state

The canonical HOM configuration consists of one photon entering each input port of the BS. The corresponding two-photon input state is written as [7]

$$|\psi_{\text{in}}\rangle = \hat{a}^\dagger \hat{b}^\dagger |0\rangle = |1_a, 1_b\rangle, \tag{2.2.2}$$

where the photons are assumed to be indistinguishable in all degrees of freedom except for the spatial mode. This assumption is essential for the observation of ideal HOM interference [7, 51] and will be relaxed in subsequent sections.

2.2.3 Beam splitter as an unitary transformation

One photon experiences a relative delay τ before entering the BS (see Fig. 2.2.1a), introducing partial distinguishability [25]. For $\tau = 0$, the photons are indistinguishable and coincidence detections are suppressed due to destructive two-photon interference, as shown in Fig. 2.2.1b. As τ increases, distinguishability grows and the coincidence probability rises, giving rise to the characteristic HOM dip.

A lossless beam splitter is described by a unitary transformation acting on the mode operators [52, 1]. For a balanced (50:50) BS, this transformation can be written as

$$\begin{pmatrix} \hat{a}_{\text{out}} \\ \hat{b}_{\text{out}} \end{pmatrix} = \frac{1}{\sqrt{2}} \begin{pmatrix} 1 & i \\ i & 1 \end{pmatrix} \begin{pmatrix} \hat{a}_{\text{in}} \\ \hat{b}_{\text{in}} \end{pmatrix}. \tag{2.2.3}$$

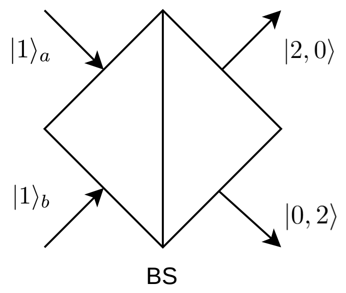

(a) Two photons interfere at a beam splitter with a relative delay τ.

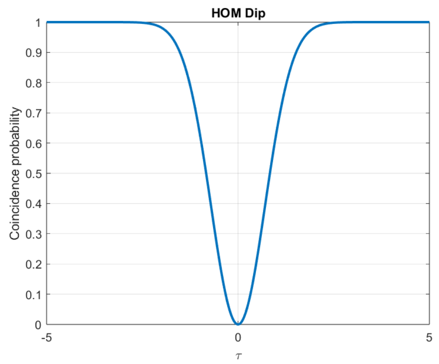

(b) Coincidence probability as a function of delay τ, showing the HOM dip.

Figure 2.2.1: HOM interference with temporal delay.

Equivalently, the transformation of the creation operators is given by

$$\hat{a}^\dagger \to \frac{1}{\sqrt{2}}\left(\hat{a}^\dagger_{\text{out}} + i\hat{b}^\dagger_{\text{out}}\right), \tag{2.2.4}$$

$$\hat{b}^\dagger \to \frac{1}{\sqrt{2}}\left(i\hat{a}^\dagger_{\text{out}} + \hat{b}^\dagger_{\text{out}}\right). \tag{2.2.5}$$

This unitary transformation preserves the bosonic commutation relations and ensures photon-number conservation.

2.2.4 Output State

Applying the BS transformation to the initial two-photon input state yields the output state

$$|\psi_{\text{out}}\rangle = \frac{1}{2}\left(\hat{a}^\dagger_{\text{out}} + i\hat{b}^\dagger_{\text{out}}\right)\left(i\hat{a}^\dagger_{\text{out}} + \hat{b}^\dagger_{\text{out}}\right)|0\rangle. \tag{2.2.6}$$

Expanding this expression and making use of the commutation relations for the creation operators, one obtains

$$|\psi_{\text{out}}\rangle = \frac{i}{\sqrt{2}}\left(|2_a, 0_b\rangle + |0_a, 2_b\rangle\right). \tag{2.2.7}$$

Notably, the terms corresponding to one photon in each output port cancel exactly [7, 25], leading to a vanishing probability amplitude for coincidence detections.

2.2.5 Physical interpretation and origin of the HOM effect

The suppression of coincidence events is the defining signature of HOM interference. This effect does not arise from classical field interference, but from destructive interference between two-photon probability amplitudes. In particular, two indistinguishable two-photon amplitudes [25, 51] contribute to the output state: both photons being transmitted (TT) and both being reflected (RR). These amplitudes interfere destructively in the coincidence channel, acquiring a relative phase that results in their complete cancellation, and leading to complete suppression of events with one photon in each output port.

This behavior highlights the intrinsically quantum nature of HOM interference: although photons are detected as individual particles, the interference occurs at the level of the two-photon quantum state, giving rise to correlations with no classical analogue [7, 53].

2.2.6 Remarks on generality and extensions

The operator-based formalism presented here provides a compact and general description of HOM interference and serves as a foundation for more realistic experimental scenarios. In practice, photons possess finite temporal and spectral wave packets, and partial distinguishability [53, 51] leads to incomplete interference. Moreover, the formalism can be extended to include additional modes, higher photon-number states, and non-ideal beam splitter transformations.

These aspects are addressed in the following sections, where a probabilistic description of HOM interference is developed and the impact of its distinguishability and decoherence is analyzed in detail.

2.3 Probabilistic Model of HOM Interference

While the operator formalism provides a compact description of Hong–Ou–Mandel interference in terms of quantum state transformations, a complementary and experimentally transparent understanding is obtained from a probabilistic model based on probability amplitudes [25, 54]. In this approach, coincidence rates are derived directly from the coherent superposition of alternative two-photon detection pathways [55, 56]. This framework is particularly well suited for incorporating realistic features such as finite temporal and spectral bandwidths, partial distinguishability, and propagation-induced delays [57, 33, 58].

2.3.1 Two-photon detection probability amplitudes

We consider two single photons entering the two input ports of a balanced BS, each described by a normalized temporal wave packet [57, 33]. In the time domain, the single-photon states can be written as

$$|1\rangle_a = \int \mathrm{d}t\, \phi_a(t)\, \hat{a}^\dagger(t)|0\rangle, \qquad |1\rangle_b = \int \mathrm{d}t\, \phi_b(t)\, \hat{b}^\dagger(t)|0\rangle, \tag{2.3.1}$$

where $\phi_a(t)$ and $\phi_b(t)$ are the temporal mode functions, satisfying the normalization condition

$$\int \mathrm{d}t\, |\phi_{a,b}(t)|^2 = 1, \tag{2.3.2}$$

which reflects the single-photon wavepacket normalization in continuous-mode quantum optics [58, 59].

The joint detection of one photon at each output port of the beam splitter can occur via two indistinguishable alternatives: (i) photon a is transmitted while photon b is reflected, or (ii) photon a is reflected while photon b is transmitted. The total probability amplitude for coincidence detection is given by the coherent sum of these two alternatives [54, 55, 56].

2.3.2 Coincidence probability and interference term

For a balanced BS, the coincidence probability can be written as

$$P_{\text{coin}} = \frac{1}{2}\left(1 - \left|\int \mathrm{d}t\, \phi_a(t)\phi_b^*(t)\right|^2\right), \tag{2.3.3}$$

which expresses the coincidence rate in terms of the overlap of the single-photon temporal modes [27, 33]. This expression assumes pure single-photon states and ideal photon-number-resolving detection [57]. The second term in this expression represents the interference contribution arising from the overlap of the two-photon probability amplitudes [60, 61]. When the photons are perfectly indistinguishable, $\phi_a(t) = \phi_b(t)$, the overlap integral equals unity and the coincidence probability vanishes. Conversely, when the photons are fully distinguishable, the overlap integral vanishes and the coincidence probability approaches the classical value of 1/2 [62].

2.3.3 Temporal delay and spectral representation

A relative temporal delay τ between the two photons modifies the temporal mode function according to

$$\phi_b(t) \rightarrow \phi_b(t-\tau), \tag{2.3.4}$$

which directly affects the temporal overlap between the photons [57, 33]. The overlap integral then becomes

$$\Lambda(\tau) = \int \mathrm{d}t\, \phi_a(t)\phi_b^*(t-\tau), \tag{2.3.5}$$

and characterizes the degree of indistinguishability as a function of delay [27, 60]. The coincidence probability can be expressed as

$$P_{\mathrm{coin}}(\tau) = \frac{1}{2}\left(1 - |\Lambda(\tau)|^2\right), \tag{2.3.6}$$

which gives rise to the characteristic Hong–Ou–Mandel dip [33, 63].

In the spectral domain, the overlap function may be written as

$$\Lambda(\tau) = \int \mathrm{d}\omega\, |\Phi(\omega)|^2 e^{-i\omega\tau}, \tag{2.3.7}$$

assuming identical spectral amplitudes $\Phi_a(\omega) = \Phi_b(\omega) = \Phi(\omega)$, which shows that the temporal overlap is given by the Fourier transform of the spectral intensity [33, 63]. This formulation explicitly highlights the role of the spectral bandwidth in determining the width of the HOM interference dip [27, 61].

2.3.4 Degree of indistinguishability

The quantity

$$\mathcal{I} = |\Lambda(0)|^2 \tag{2.3.8}$$

is commonly referred to as the degree of indistinguishability between the two photons [25, 27, 64]. It quantifies the extent to which the photons overlap in all relevant degrees of freedom, including temporal, spectral, spatial, and polarization modes [65, 26].

In realistic experimental conditions, imperfect mode overlap, spectral mismatch, or polarization misalignment result in $0 < \mathcal{I} < 1$, leading to a reduced visibility of the HOM dip [66, 35, 67]. The coincidence probability at zero delay is then given by

$$P_{\text{coin}}(0) = \frac{1}{2}(1 - \mathcal{I}), \tag{2.3.9}$$

which directly relates the coincidence rate to the photon indistinguishability and the visibility of the interference dip [63, 25].

2.3.5 Visibility for Two-Photon Interference

In classical interferometry, such as with a Mach–Zehnder interferometer (MZI) [68], the visibility (or contrast) of interference fringes is conventionally defined as [5, 69]

$$V_{\text{classical}} = \frac{I_{\max} - I_{\min}}{I_{\max} + I_{\min}}, \tag{2.3.10}$$

where $I_{\max}$ and $I_{\min}$ denote the maximum and minimum intensities of the interference pattern. The denominator normalizes the modulation depth with respect to the average intensity, ensuring that $0 \leq V \leq 1$. This definition is appropriate for sinusoidal interference that oscillates symmetrically around a fixed mean value.

The HOM effect, however, represents a qualitatively different phenomenon [7, 25]. Rather than producing oscillatory fringes, it manifests as a *destructive suppression* of the coincidence probability relative to a fixed classical baseline. We denote this baseline as $P_{\text{coin}}(\infty)$, which corresponds to the coincidence probability when the photons are fully distinguishable (e.g., by introducing a delay much longer than the coherence time or by making their polarizations orthogonal). In this regime, no two-photon interference occurs and the photons behave independently [24, 70].

Applying the classical visibility formula directly to an HOM dip would therefore be inappropriate. If one were to use $P_{\text{coin}}(\infty) + P_{\text{coin}}(0)$ in the denominator, the normalization would itself depend on the degree of indistinguishability, since $P_{\text{coin}}(0)$ varies with interference strength. This would obscure the operational meaning of visibility as the fractional suppression of coincidences relative to the classical reference level.

Instead, the HOM visibility is defined with respect to the classical baseline [25, 24]:

$$V_{\mathrm{HOM}} = \frac{P_{\mathrm{coin}}(\infty) - P_{\mathrm{coin}}(0)}{P_{\mathrm{coin}}(\infty)}. \tag{2.3.11}$$

Here, $P_{\mathrm{coin}}(0)$ denotes the coincidence probability at zero delay, where the photons are optimally overlapped in all degrees of freedom. This definition yields $V_{\mathrm{HOM}} = 0$ for fully distinguishable photons, and $V_{\mathrm{HOM}} = 1$ for perfectly indistinguishable photons in an ideal interferometer.

Operationally, a visibility of $V = 0.8$, for example, indicates that quantum interference suppresses the coincidence probability by 80% relative to the classical distinguishable limit [71]. This definition aligns directly with the theoretical description of HOM interference in Eq. 2.3.9.

For two single-photon states described by density operators $\rho_a = \sum_{ij} \rho_{ij}^{(a)} |i\rangle\langle j|$ and $\rho_b = \sum_{ij} \rho_{ij}^{(b)} |i\rangle\langle j|$, the coincidence probability reads [72, 73]

$$P_{\mathrm{coin}} = \frac{1}{2} \left(1 - \mathrm{Tr}[\rho_a \rho_b]\right). \tag{2.3.12}$$

In the fully distinguishable limit, the internal states are orthogonal and $\mathrm{Tr}[\rho_a \rho_b] = 0$, yielding $P_{\mathrm{coin}}(\infty) = \frac{1}{2}$. At zero delay, the coincidence probability becomes $P_{\mathrm{coin}}(0) = \frac{1}{2}(1 - \mathrm{Tr}[\rho_a \rho_b])$. Substituting these expressions into the definition of the HOM visibility of Eq. 2.3.11 immediately gives [25, 74]

$$V = \mathrm{Tr}[\rho_a \rho_b]. \tag{2.3.13}$$

The quantity $\mathrm{Tr}[\rho_a \rho_b]$ is the Hilbert–Schmidt inner product of two density operators. Since density operators are positive semidefinite and have unit trace, this overlap satisfies

$$0 \leq \mathrm{Tr}[\rho_a \rho_b] \leq 1. \tag{2.3.14}$$

The lower bound follows from positivity, while the upper bound is reached if and only if $\rho_a = \rho_b$ and both states are pure. Consequently, the HOM visibility is naturally bounded between 0 and 1 and provides a direct operational measure of photon indistinguishability.

In experiments, one typically measures coincidence *count rates* $C(\tau)$, which are proportional to the coincidence probability [75, 76]:

$$C(\tau) = R\,P_{\text{coin}}(\tau), \tag{2.3.15}$$

where R is the effective pair generation and detection rate. Since visibility is a ratio, this proportionality cancels, and the same expression in Eq. (2.3.11) applies equally to measured count rates.

In practice, measured coincidences often include accidental background contributions C_{bg} that do not participate in the interference. After background subtraction, the net visibility becomes [72, 77]

$$V_{\text{net}} = \frac{P_{\text{coin}}(\infty) - P_{\text{coin}}(0)}{P_{\text{coin}}(\infty) - P_{\text{bg}}}, \tag{2.3.16}$$

where $P_{\text{bg}} = C_{\text{bg}}/R$.

Throughout this work, unless otherwise stated, "visibility" refers to the definition in Eq. (2.3.11), corresponding to the raw suppression factor relative to the distinguishable baseline.

2.3.6 Gaussian wave-packet model

To obtain an explicit analytical expression for the HOM interference pattern, it is convenient to model the photons as Gaussian wave packets [5]. In the spectral domain, the single-photon amplitude is written as

$$\Phi(\omega) = \frac{1}{(2\pi\sigma_\omega^2)^{1/4}} \exp\left[-\frac{(\omega-\omega_0)^2}{4\sigma_\omega^2}\right], \tag{2.3.17}$$

where ω_0 is the central angular frequency and σ_ω characterizes the spectral bandwidth.

The corresponding temporal mode function is obtained via Fourier transform [5, 25] and reads

$$\phi(t) = \frac{1}{(2\pi\sigma_t^2)^{1/4}} \exp\left(-\frac{t^2}{4\sigma_t^2}\right), \tag{2.3.18}$$

with $\sigma_t = 1/(2\sigma_\omega)$.

Introducing a relative temporal delay τ between the two photons, the overlap function becomes [33, 78]

$$\Lambda(\tau) = \int \mathrm{d}t\, \phi(t)\phi^*(t-\tau) = \exp\left(-\frac{\tau^2}{8\sigma_t^2}\right). \tag{2.3.19}$$

The coincidence probability as a function of delay is therefore given by

$$P_{\mathrm{coin}}(\tau) = \frac{1}{2}\left[1 - \exp\left(-\frac{\tau^2}{4\sigma_t^2}\right)\right], \tag{2.3.20}$$

which corresponds to a Gaussian-shaped HOM dip whose width is determined by the photon coherence time [25, 79, 66, 80].

2.3.7 Fisher Information and Sensitivity of the HOM Interferometer

While the visibility of the HOM dip quantifies the degree of two-photon interference, it does not fully characterize the sensitivity of the interferometer to small variations of physical parameters. In many practical scenarios, such as temporal delay estimation or dispersion characterization, the relevant figure of merit is not the depth of the dip, but how rapidly the coincidence probability changes with the parameter of interest. This sensitivity is rigorously quantified by the Fisher information, a central concept in estimation theory and quantum metrology [81, 82, 83].

We consider the estimation of a parameter τ (e.g., relative temporal delay) from coincidence measurements. The measurement outcomes are binary: either a coincidence event occurs or it does not. The corresponding probabilities are given by

$$P_{\mathrm{coin}}(\tau), \qquad P_{\mathrm{no\ coin}}(\tau) = 1 - P_{\mathrm{coin}}(\tau). \tag{2.3.21}$$

For a given statistical model $P(x|\tau)$, the (classical) Fisher information is defined as [81, 82]

$$\mathcal{F}(\tau) = \sum_x \frac{1}{P(x|\tau)}\left(\frac{\partial P(x|\tau)}{\partial \tau}\right)^2, \tag{2.3.22}$$

where the sum runs over all possible measurement outcomes x. In the present case, this reduces to

$$\mathcal{F}(\tau) = \frac{1}{P_{\text{coin}}(\tau)} \left(\frac{\partial P_{\text{coin}}(\tau)}{\partial \tau} \right)^2 + \frac{1}{1 - P_{\text{coin}}(\tau)} \left(\frac{\partial P_{\text{coin}}(\tau)}{\partial \tau} \right)^2 . \tag{2.3.23}$$

Using the Gaussian model derived in Eq. 2.3.20, the derivative with respect to τ is

$$\frac{\partial P_{\text{coin}}}{\partial \tau} = \frac{\tau}{4\sigma_t^2} \exp\left(-\frac{\tau^2}{4\sigma_t^2} \right) . \tag{2.3.24}$$

Substituting into the definition of $\mathcal{F}(\tau)$ yields

$$\mathcal{F}(\tau) = \frac{1}{P_{\text{coin}}(\tau) \left[1 - P_{\text{coin}}(\tau)\right]} \left(\frac{\partial P_{\text{coin}}(\tau)}{\partial \tau} \right)^2 . \tag{2.3.25}$$

This expression reveals that the Fisher information depends on two competing factors: the slope of the HOM dip, encoded in $\partial_\tau P_{\text{coin}}(\tau)$, and the statistical weight of the measurement outcomes through the factor $P_{\text{coin}}(\tau) \left[1 - P_{\text{coin}}(\tau)\right]$. This structure is generic in parameter estimation problems and reflects the trade-off between signal slope and statistical noise [83].

A key feature is that the Fisher information vanishes at $\tau = 0$, despite the fact that this is the point of maximum interference visibility. At zero delay, the coincidence probability reaches a minimum and becomes locally flat, implying that small variations in τ produce negligible changes in the observed signal. Consequently, the HOM interferometer is not most sensitive at the bottom of the dip. This behavior has been widely recognized in HOM-based metrology, where maximum sensitivity occurs away from the point of perfect indistinguishability [80, 84].

Instead, the Fisher information is maximized at finite values of τ, near the region where the slope of the interference curve is steepest. For the Gaussian model, this occurs on the sides of the HOM dip, at delays on the order of the photon coherence time σ_t. This behavior highlights an important distinction: maximum indistinguishability (and thus maximum visibility) does not coincide with maximum parameter sensitivity.

The Fisher information provides a direct connection to the precision limits of parameter estimation through the Cramér–Rao bound,

$$\Delta\tau \geq \frac{1}{\sqrt{N\,\mathcal{F}(\tau)}}, \tag{2.3.26}$$

where N is the number of independent measurement trials. This bound establishes the HOM interferometer as a metrological tool, whose ultimate precision is governed by the Fisher information and its quantum generalization [82, 83].

In practical implementations, factors such as reduced visibility, background counts, and detector inefficiencies modify $P_{\text{coin}}(\tau)$ and therefore degrade the achievable Fisher information. As a result, optimizing HOM-based measurements for metrological applications requires not only maximizing indistinguishability, but also engineering the spectral and temporal structure of the photons to enhance the slope of the interference feature in the region of operation.

This analysis reinforces the interpretation of HOM interference as a parameter-dependent measurement process and provides a quantitative framework for assessing its performance in quantum metrology and sensing applications. Recent works have explicitly demonstrated that HOM-based schemes can achieve high-precision estimation and that the achievable sensitivity scales with the Fisher information of the interference pattern [85, 84].

2.4 A key application of HOM effect: Bell-State Measurements

The HOM effect provides the physical mechanism underlying linear-optical Bell-state measurements (BSMs) [86, 87]. While the previous section described the probabilistic interference of two indistinguishable photons at a beam splitter, we now show how this interference enables projection onto maximally entangled two-qubit states.

2.4.1 Bell Basis

For two qubits encoded, for example, in photon polarization or dual-rail modes, the maximally entangled Bell states are defined as [88]

$$\left|\Phi^{\pm}\right\rangle = \frac{1}{\sqrt{2}}\left(|00\rangle \pm |11\rangle\right), \tag{2.4.1}$$

$$\left|\Psi^{\pm}\right\rangle = \frac{1}{\sqrt{2}}\left(|01\rangle \pm |10\rangle\right). \tag{2.4.2}$$

These four states form an orthonormal basis of the two-qubit Hilbert space. A Bell-state measurement corresponds to a projective measurement in this basis [3, 86].

In quantum networking and entanglement swapping protocols, the BSM plays a central role: it transfers entanglement between subsystems by projecting two incoming qubits onto one of the four Bell states [89, 90].

2.4.2 Linear-Optical Implementation

In practice, deterministic discrimination of all four Bell states using only linear optics, photon counting, and no ancillary photons is impossible [91, 92]. This limitation arises from the bosonic symmetry of photons and the linearity of optical transformations.

As established in Sec. 2.2, two indistinguishable photons bunch due to bosonic symmetry, leading to suppression of coincidence events. This behavior enables discrimination between symmetric and antisymmetric two-photon states [25, 28].

For polarization encoding, a standard linear-optical BSM consists of a beam splitter followed by polarization-resolving detectors at each output port [86, 93], as shown in Fig. 2.4.1. Due to its antisymmetry under particle exchange, the Bell state

$$\left|\Psi^{-}\right\rangle = \frac{1}{\sqrt{2}}(|01\rangle - |10\rangle) \tag{2.4.3}$$

remains invariant (up to phase) under the BS transformation and results in one photon exiting each output port [86]. As a result, it produces coincidence detections in distinct output ports. In contrast, the symmetric Bell states $|\Psi^{+}\rangle$ and $|\Phi^{\pm}\rangle$ lead to photon bunching and cannot be fully distinguished from one another using only linear optics [91]. At a fundamental level, HOM interference is

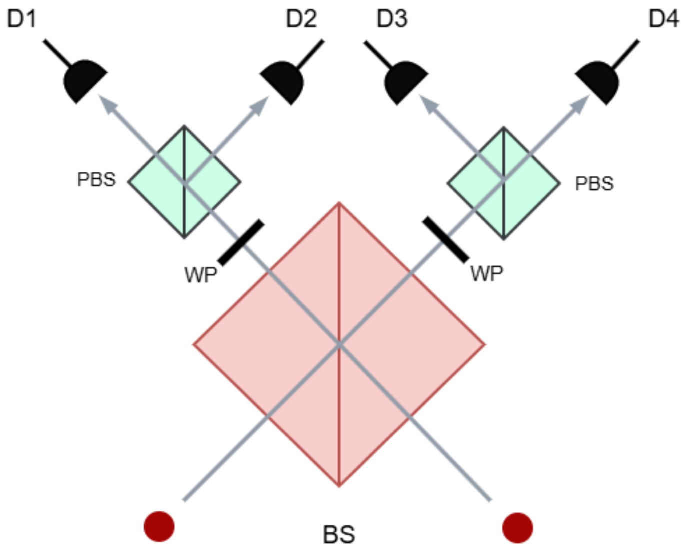

Figure 2.4.1: Typical experimental implementation for polarization-encoded optical Bell measurement. BS - beam splitter, WP - waveplate, PBS - polarizing beam splitter, D - single-photon detector.

a direct consequence of bosonic exchange symmetry combined with linear mode mixing at the beam splitter.

Consequently, a linear-optical setup without ancillary photons can unambiguously identify at most two of the four Bell states. The maximum theoretical success probability for discriminating Bell states with linear optics is therefore [91, 92]

$$P_{\mathrm{BSM}}^{\max} = \frac{1}{2}. \tag{2.4.4}$$

This 50% bound is fundamental and directly impacts the efficiency of entanglement swapping and event-ready protocols (see Chapter 5).

2.4.3 Physical Mechanism of Linear-Optical Bell-State Measurements

The probabilistic two-photon interference described above constitutes the physical mechanism underlying linear-optical Bell-state discrimination [25, 37]. A beam splitter does not by itself "measure" entanglement; rather, it mixes optical modes in such a way that two-photon probability amplitudes interfere. When the photons are indistinguishable in all degrees of freedom except for the encoded qubit (e.g., polarization or dual-rail mode), this interference faithfully implements a projection onto symmetric and antisymmetric two-photon subspaces [67].

In particular, perfect indistinguishability ensures that the BS transformation depends only on the exchange symmetry of the joint quantum state [74]. The antisymmetric Bell state remains separable into one photon per output port, while symmetric states exhibit photon bunching [86]. Any residual distinguishability introduces which-path information, weakens the interference, and consequently reduces the reliability of Bell-state discrimination [94].

In quantum communication architectures, the BSM serves as an entanglement mediator [89, 95]. Two photons arriving from distant sources interfere at a central station, and a successful coincidence event projects the remote systems into an entangled state. Importantly, the measurement outcome is classical information that can be communicated to remote parties, thereby enabling heralded entanglement generation [90] (see Chapter 5).

While the intrinsic 50% success probability limits efficiency, it does not compromise the validity of the projected entangled state [91]. Instead, it reduces the rate at which successful entanglement events occur. This probabilistic character becomes a key design constraint in quantum repeaters and device-independent quantum key distribution (more details in Sec.5.7), where entanglement generation rates must compete with memory decoherence and transmission losses [90, 37].

In summary, the Bell-state measurement provides the operational bridge between HOM interference at the physical level and long-distance entanglement distribution at the protocol level. It transforms two locally prepared photon–qubit correlations into remote entanglement and thereby enables entanglement swapping and event-ready quantum communication schemes [89, 95].

2.5 Operational Applications

HOM interference is more than a fundamental demonstration of two-photon quantum behavior: it constitutes an operational resource enabling a wide range of quantum technologies [25]. At its core, HOM interference implements a symmetry-sensitive projection arising from bosonic exchange and linear mode mixing. The measurable quantity, the coincidence probability, directly reflects the overlap of photonic wave functions [33]. This overlap-dependent projection mechanism underlies its diverse applications [37].

2.5.1 High-Dimensional Entanglement

When photons are encoded in degrees of freedom of dimension $d > 2$, such as time bins, frequency bins, spatial modes, or orbital angular momentum, the HOM interference visibility becomes sensitive to multidimensional mode overlap [28, 96]. In this regime, the beam splitter acts as a projector onto symmetric and antisymmetric subspaces of a high-dimensional Hilbert space [97].

Consequently, HOM measurements provide a practical tool for certifying and characterizing high-dimensional entanglement [98, 99]. Because the interference contrast depends on overlap across all encoded modes, it allows direct access to coherence properties beyond qubit systems [98]. In integrated and multicore photonic platforms, spatial-mode encoding naturally enables such high-dimensional interference [37, 100].

2.5.2 Quantum State Characterization

Because the HOM interference pattern depends on the overlap function $\Lambda(\tau)$, it provides access to the spectral and temporal structure of single-photon states [25, 33]. Analysis of the dip shape, depth, and symmetry enables [63, 101, 102]:

- Estimation of photon purity [63, 101];
- Reconstruction of joint spectral amplitudes [102, 75];
- Quantification of partial distinguishability [103, 104];
- Detection of decoherence effects [104, 105].

HOM interferometry thus offers a resource-efficient alternative to full quantum state tomography, particularly for high-dimensional and multimode photonic states [106, 105].

2.5.3 Linear Optical Quantum Information Processing

In linear optical quantum computing, HOM interference provides the effective interaction mechanism between otherwise non-interacting photons [107, 108]. The destructive interference responsible for coincidence suppression enables conditional state transformations when combined with post-selection [107, 109].

Probabilistic entangling gates, such as CNOT and CZ operations, exploit this projection onto symmetric or antisymmetric two-photon subspaces [110, 109]. Gate fidelity is directly linked to photon indistinguishability, making HOM visibility a quantitative benchmark for photonic quantum processors [108, 111].

2.5.4 Quantum Metrology

The coincidence probability depends sensitively on relative temporal delay and spectral phase [112, 103]. As a result, the HOM dip provides a high-resolution probe of optical path-length differences and dispersion [113, 67].

Small variations in delay, refractive index, or spectral phase translate into measurable changes in coincidence rates [114, 115]. Unlike classical interferometry, HOM interference does not require first-order phase stability between the sources, making it particularly suitable for characterizing dispersive or multimode photonic systems [25, 67].

2.5.5 Quantum Communication

HOM interference enables two-photon interference between independent sources without phase stabilization [116, 95]. This property is central to measurement-device-independent quantum key distribution (MDI-QKD) and entanglement swapping protocols (see Chapter 5) [41, 89, 40].

In such architectures, successful interference events herald entanglement generation or key establishment [40, 93]. The achievable rate and fidelity depend directly on indistinguishability, making HOM visibility a practical performance metric for long-distance quantum networks [108, 25]. Spatial multiplexing in multicore fibers further extends these capabilities by enabling parallel interference channels [117, 118].

Figure 2.5.1 summarizes the operational role of HOM interference in some subareas. The beam splitter implements a symmetry-sensitive projection whose outcome depends on photonic mode overlap [25]. This projection mechanism forms the common physical foundation underlying applications in quantum communication, computing, metrology, and state characterization [37].

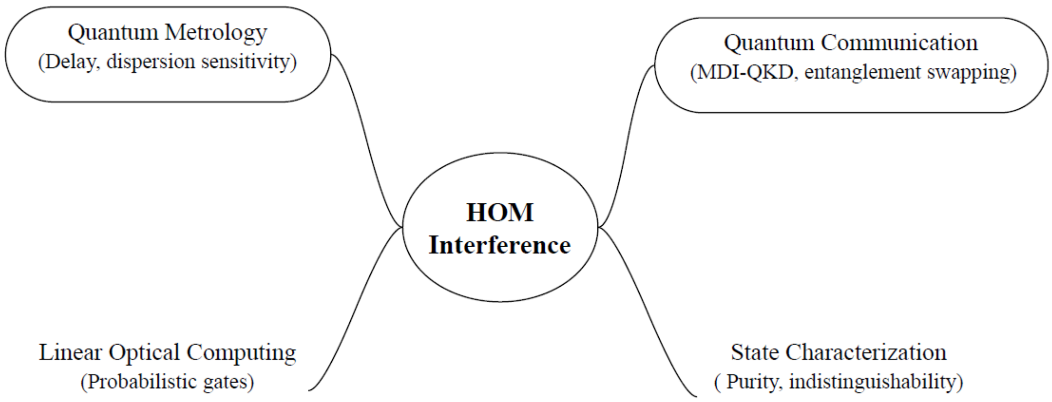

Figure 2.5.1: Schematic overview of the operational role of HOM interference across quantum technologies, highlighting the applications on Quantum Metrology and Quantum Communication, the main focus of this thesis.

Summary

Across these diverse applications, HOM interference emerges as a unifying operational principle that connects fundamental quantum mechanics to practical quantum technologies. Its implementation in scalable photonic platforms, such as multicore fibers, opens promising pathways toward high-dimensional quantum information processing, precision metrology, and robust quantum communication networks. Moreover, HOM interference constitutes a fundamental symmetry-based primitive upon which a broad class of photonic quantum protocols are constructed.

Chapter 3

Multicore Fiber Platform for Scalable Quantum Interference

3.1 Stable Multiport Quantum Interference in Fiber

Scalable quantum photonic architectures require interferometric networks capable of coherently mixing multiple spatial modes with high stability and low loss [119, 120]. While bulk-optics interferometers have played a central role in foundational quantum optics experiments [121], their scalability is fundamentally limited by mechanical instability, alignment complexity, and long-term phase drift [122]. As the dimensionality of the Hilbert space increases—for instance in path-encoded qudit systems or multiport interference networks—these limitations become increasingly restrictive [123]. A compact, intrinsically phase-stable, and fiber-integrated platform is therefore essential for advancing large-scale quantum information processing [124].

Multiport interference generalizes the conventional two-mode beam splitter to higher-dimensional unitary transformations [125]. Such transformations are required in a variety of quantum protocols, including high-dimensional state manipulation [126], multi-photon interference experiments [24], entanglement distribution across spatial modes [127], and linear-optical quantum information processing [128, 129]. In particular, the Hong–Ou–Mandel effect in multiport devices provides a sensitive probe of photon indistinguishability and temporal correlations, extending the two-photon interference paradigm to higher-dimensional mode structures [7, 130]. The visibility and symmetry of these interference patterns depend critically on precise control of relative optical delays between spatial channels [131].

Multicore optical fibers (MCFs) provide a natural hardware platform for implementing stable multiport interferometers in a compact geometry [132]. In weakly coupled MCFs, several single-mode cores are embedded within a common cladding, allowing spatial multiplexing of optical modes while maintaining strong mechanical and thermal correlation among them [133]. Because all cores share the same physical environment, differential phase drifts are significantly reduced compared to independent fiber paths [134]. This common-cladding architecture therefore offers enhanced passive stability, which is particularly advantageous for two-photon interference experiments requiring sub-picosecond temporal precision [135].

Beyond stability, the intrinsic parallelism of MCFs enables controlled spatial mode transformations through engineered inter-core coupling regions [136]. By designing appropriate coupling lengths and core arrangements, one can implement symmetric multiport beam splitters directly within the fiber platform [125]. These devices realize well-defined unitary transformations without the need for free-space alignment or cascaded discrete components [137]. As a result, MCF-based multiport interferometers constitute a scalable and fiber-compatible alternative to bulk or chip-based interferometric networks [138].

In this thesis, the multicore fiber platform serves as the experimental infrastructure for precision temporal metrology based on multiport HOM interference. The central objective of this chapter is to define and characterize the 4×4 multicore fiber beam splitter used throughout the subsequent analysis. We establish its physical architecture, derive the corresponding unitary transformation, and model two-photon interference within this device. Particular emphasis is placed on the sensitivity of multiport HOM interference to differential group delays between cores. In the following chapter, this sensitivity will be exploited to extract inter-core skew with high precision, using the platform developed here as the underlying experimental basis.

3.2 Multicore Fiber Architecture

MCFs are waveguiding structures in which multiple single-mode cores are embedded within a common cladding [22]. Each core supports an independent spatial channel while sharing the same mechanical, thermal, and environmental conditions. This architecture enables spatial multiplexing of optical modes with enhanced passive stability compared to bundles of discrete fibers. In the context of quantum interference experiments, such common-mode stability is essential for preserving phase coherence and minimizing differential path-length fluctuations between channels [139].

In this work, we focus on *weakly-coupled* MCFs [133], where the cores are sufficiently separated such that inter-core crosstalk during propagation is strongly suppressed. Under this condition, each core can be treated as an independent single-mode waveguide over the relevant fiber lengths, and controlled mode mixing occurs only in engineered coupling regions such as multicore beam splitters.

3.2.1 Weakly-Coupled Multicore Fibers

In weakly-coupled MCFs, as shown in Fig. 3.2.1, the core-to-core separation is chosen to minimize evanescent coupling between adjacent modes along the propagation direction [21]. Typical center-to-center core spacings exceed several tens of micrometers, ensuring that power transfer between cores is negligible over kilometer-scale lengths. As a result, inter-core crosstalk remains far below levels that would degrade quantum interference visibility, allowing each core to function as a well-isolated spatial mode.

From a waveguide perspective, each core is designed to be single-mode at the operating wavelength, with closely matched effective refractive indices across all cores. Residual variations in core geometry or refractive index profile arising from fabrication tolerances lead to small differences in effective index and group velocity. These differences manifest as *differential group delay* between cores, commonly referred to as inter-core skew (see Chapter 4). Although typically on the order of femtoseconds to picoseconds per meter, such delays are directly relevant for two-photon interference experiments involving broadband photons, whose coherence times can be comparably short [140].

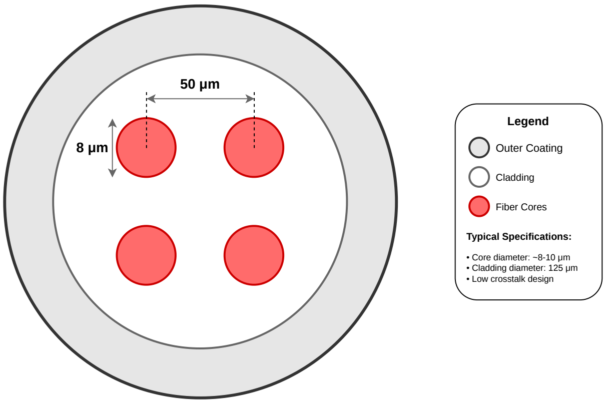

Figure 3.2.1: Multicore Fiber Cross-Section

The weakly-coupled regime is therefore characterized by a trade-off: while large core separation suppresses unwanted crosstalk, it does not eliminate differential propagation delays. Understanding and quantifying these delays is a central objective of this thesis and motivates the use of HOM interference as a precision temporal probe.

3.2.2 Phase Stability and Environmental Robustness

A defining advantage of MCFs over independent fiber paths is their intrinsic phase stability. Because all cores are embedded within a single cladding, they experience nearly identical environmental perturbations, including temperature fluctuations, mechanical stress, and acoustic vibrations. These perturbations primarily induce common-mode phase shifts, while differential phase fluctuations between cores are strongly suppressed.

This property is particularly advantageous for quantum interference experiments, where relative phase stability on timescales of minutes to hours is often required. In contrast, interferometers constructed from separate fibers typically require active stabilization to compensate for independent thermal expansion and mechanical drift [141]. In MCFs, the common-cladding geometry significantly reduces the need for such stabilization, enabling long-term measurements of two-photon interference with high reproducibility [142].

3.2.3 Multiplexing Interfaces and Fan-In/Fan-Out Devices

Interfacing single-mode fibers with multicore fibers requires specialized multiplexing (MUX) and demultiplexing (DEMUX) devices, commonly referred to as fan-in and fan-out components [143]. These devices map individual single-mode fiber inputs onto specific cores of the MCF and perform the inverse operation at the output, as shown in Fig. 3.2.2. For quantum applications, the performance of these interfaces is critical, as insertion loss, mode-dependent loss, and residual crosstalk directly impact interference visibility and count rates.

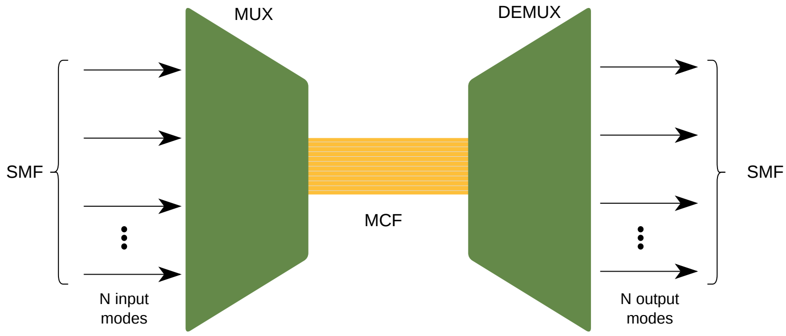

Figure 3.2.2: MUX/DEMUX schematics for NxN input-output modes.

In the experiments presented in this thesis, fan-in and fan-out devices are designed to preserve spatial mode purity and polarization alignment across all channels. Imperfections at these interfaces can introduce imbalance between cores, leading to asymmetric splitting ratios in downstream multiport devices and reducing the symmetry of multi-photon interference patterns. While such effects do not prevent HOM interference, they must be carefully characterized to ensure that deviations from ideal behavior are correctly attributed to physical effects such as inter-core skew rather than to interface artifacts.

Taken together, the weakly-coupled multicore fiber architecture provides a set of well-defined spatial channels with enhanced phase stability, controlled loss characteristics, and intrinsic differential delays. These properties make MCFs particularly well suited for implementing stable multiport interferometers and for performing precision temporal measurements based on two-photon quantum interference. In the following section, we build upon this architecture to introduce the 4×4 multicore fiber beam splitter that forms the core interferometric element of our experimental platform.

3.3 The 4×4 Multicore Fiber Beam Splitter

The central interferometric element of the experimental platform is a symmetric 4×4 multicore fiber beam splitter (MCF-BS) [125]. This device implements a coherent transformation between four spatial modes supported by distinct fiber cores. Unlike bulk multiport interferometers constructed from cascaded beam splitters and phase shifters, the MCF-BS realizes the required unitary transformation within a compact fiber-integrated geometry through controlled inter-core coupling [144].

3.3.1 Physical Implementation via Evanescent Coupling

The 4×4 multicore fiber beam splitter is realized by inducing controlled evanescent coupling between adjacent cores over a finite interaction length, as we can see in Fig. 3.3.1. Outside this region, the cores are sufficiently separated to operate in the weakly coupled regime, ensuring independent single-mode propagation [145]. Within the coupling section, the inter-core spacing is reduced such that the evanescent tails of the guided modes overlap, enabling coherent power exchange.

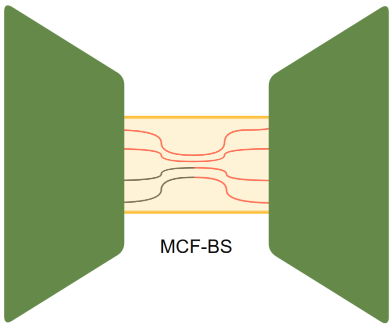

Figure 3.3.1: Multicore beam splitter (MCF-BS) between MUX/DEMUX devices in green, showing evanescent coupling.

The coupling dynamics are accurately described within coupled-mode theory (CMT), as developed in guided-wave perturbation theory [146, 147, 148]. In a weakly guiding fiber, the electric field may be expressed as a superposition of guided modes,

$$\mathbf{E}(x, y, z) = \sum_m a_m(z)\, \mathbf{e}_m(x, y)\, e^{i\beta_m z}, \tag{3.3.1}$$

where $\mathbf{e}_m(x, y)$ denotes the transverse mode profile of core m, β_m is the corresponding propagation constant, and $a_m(z)$ is a slowly varying amplitude.

When the cores are brought into proximity, the refractive index profile of each core acts as a perturbation to its neighbors. Under the slowly varying envelope approximation, CMT yields the coupled differential equations

$$\frac{da_m}{dz} = -i\beta_m a_m - i\sum_{n\neq m} \kappa_{mn} a_n, \tag{3.3.2}$$

where κ_{mn} is the coupling coefficient between modes m and n. Physically, κ_{mn} is determined by the spatial overlap of the evanescent fields and can be expressed as an overlap integral of the modal profiles weighted by the refractive index perturbation. Its magnitude decreases approximately exponentially with increasing core separation.

Equation (3.3.2) can be written compactly in matrix form as

$$\frac{d\mathbf{a}}{dz} = -i\mathbf{H}_{\text{eff}}\mathbf{a}, \tag{3.3.3}$$

where $\mathbf{a} = (a_1, a_2, a_3, a_4)^T$ and $\mathbf{H}_{\text{eff}}$ is an effective Hermitian coupling matrix containing the propagation constants along the diagonal and the inter-core coupling coefficients in the off-diagonal elements. The solution after an interaction length L is

$$\mathbf{a}(L) = e^{-i\mathbf{H}_{\text{eff}}L}\mathbf{a}(0). \tag{3.3.4}$$

Thus, the coupling region implements a unitary transformation

$$\mathbf{U} = e^{-i\mathbf{H}_{\text{eff}}L}, \tag{3.3.5}$$

which preserves optical power and quantum coherence.

For the symmetric 4×4 BS considered here, the device geometry is engineered such that the propagation constants β_m are nearly identical across all cores. Also, the dominant coupling coefficients between selected core pairs are equal in magnitude, and the interaction length L is chosen to produce balanced mode mixing.

Under these symmetry conditions, the exponential of the effective coupling matrix approximates a balanced unitary transformation, often modeled as a Hadamard or discrete Fourier transform matrix, yielding equal magnitude amplitudes at all output ports [125]. Small deviations from ideal symmetry arise from fabrication tolerances and residual birefringence but do not alter the fundamentally unitary and coherent nature of the transformation.

Importantly, because the coupling occurs within a monolithic fiber structure, the relative phases accumulated in the interaction region are intrinsically stable. The multiport therefore realizes a compact, mechanically robust interferometer whose transformation is determined by the engineered coupling matrix rather than by cascaded discrete optical elements.

3.3.2 Unitary Transformation

In the ideal symmetric case, the 4×4 multicore beam splitter implements the unitary transformation [125]

$$\mathbf{U}_{BS} = \frac{1}{2}\begin{bmatrix} 1 & 1 & 1 & 1 \\ 1 & 1 & -1 & -1 \\ 1 & -1 & 1 & -1 \\ 1 & -1 & -1 & 1 \end{bmatrix}, \tag{3.3.6}$$

which is equivalent to a normalized four-dimensional Hadamard matrix [149]. This transformation evenly redistributes the amplitude of each input mode across all output modes while introducing relative phase shifts that determine the interference structure.

The unitarity condition

$$\mathbf{U}_{BS}^{\dagger}\mathbf{U}_{BS} = \mathbf{I} \tag{3.3.7}$$

ensures photon-number conservation and guarantees that the transformation preserves quantum coherence [5].

A defining feature of the matrix in Eq. (3.3.6) is its symmetry: all input modes contribute equally in magnitude to every output mode, while the relative signs determine constructive or destructive interference in multi-photon processes. This symmetry gives rise to a structured pattern of enhanced and suppressed coincidence probabilities in two-photon interference experiments, as derived in the next section.

In practice, the implemented transformation deviates slightly from the ideal symmetric unitary due to unavoidable fabrication and operational imperfections. These include non-uniform coupling coefficients between different core pairs arising from small variations in core spacing or refractive index contrast, mode-dependent insertion losses introduced at fan-in/fan-out interfaces and splicing points, residual birefringence leading to polarization-dependent phase shifts within the coupling region, and small differential propagation phases accumulated before and after the interaction section due to path-length mismatches or group index variations. Although these effects perturb the exact symmetry of the ideal transformation, they remain sufficiently small to preserve the overall unitary and coherent character of the multiport, and can be experimentally characterized and compensated during calibration.

These deviations modify the effective unitary transformation to

$$\mathbf{U}_{\text{eff}} = \mathbf{D}_{\text{out}}\, \mathbf{U}_{BS}\, \mathbf{D}_{\text{in}}, \tag{3.3.8}$$

where $\mathbf{D}_{\text{in}}$ and $\mathbf{D}_{\text{out}}$ represent diagonal phase and amplitude matrices accounting for input and output imperfections. Although such imperfections alter the detailed coincidence structure, the fundamental multiport interference mechanism remains intact provided that coherence between spatial modes is preserved.

The 4×4 MCF-BS thus serves as the core interferometric element of the experimental platform. Its symmetry properties define the interference signatures expected for indistinguishable photons, while deviations from ideal behavior provide insight into physical effects such as imbalance and inter-core skew. In the following section, we derive the two-photon interference model associated with this multiport transformation.

3.4 Theoretical Model of Two-Photon Interference in a 4×4 Multiport

The HOM formalism developed in Chapter 2 is now extended to the case of a symmetric 4×4 multiport. The objective is to derive the coincidence probabilities associated with two-photon interference and to establish the characteristic suppression and enhancement structure that forms the experimental signature of indistinguishability.

Throughout this section, we consider two photons injected into distinct input modes of the multiport. Without loss of generality, we take the photons to enter input ports 1 and 3.

3.4.1 Two-Photon Input State and Operator Transformation

The input state is a two-photon Fock state occupying spatial modes 1 and 3,

$$|\Psi_{\text{in}}\rangle = \hat{a}_1^\dagger \hat{a}_3^\dagger |0\rangle = |1_1, 0_2, 1_3, 0_4\rangle . \tag{3.4.1}$$

The multiport transformation is described by the unitary matrix $\mathbf{U}$ introduced in Section 3.3. The creation operators transform as

$$\hat{a}_j^\dagger = \sum_{k=1}^{4} U_{kj}^* \, \hat{b}_k^\dagger, \tag{3.4.2}$$

where $\hat{a}_j^\dagger$ and $\hat{b}_k^\dagger$ correspond to the input and output spatial modes, respectively. Substituting into the input state yields the output state

$$|\Psi_{\text{out}}\rangle = \left(\sum_{i=1}^{4} U_{i1}^* \hat{b}_i^\dagger \right) \left(\sum_{j=1}^{4} U_{j3}^* \hat{b}_j^\dagger \right) |0\rangle . \tag{3.4.3}$$

Expanding the product produces a coherent superposition of all two-photon occupation terms across the four output modes. Coincidence probabilities are obtained by projecting this state onto distinct output pairs (i, j) with $i \neq j$.

3.4.2 Coincidence Probabilities for Indistinguishable Photons

For indistinguishable photons, the two-photon amplitude associated with detecting one photon in output port i and one in port j $(i \neq j)$ is given by the coherent sum of the two possible paths:

$$A_{ij} = U_{i1}U_{j3} + U_{i3}U_{j1}. \tag{3.4.4}$$

No additional normalization factor appears because the photons occupy distinct input modes and the output operators commute.

The corresponding coincidence probability is

$$P_{ij}^{\text{ind}} = |A_{ij}|^2 = |U_{i1}U_{j3} + U_{i3}U_{j1}|^2 \,. \tag{3.4.5}$$

The interference term arises from the cross-product

$$2\,\mathrm{Re}\left(U_{i1}U_{j3}U_{i3}^{*}U_{j1}^{*}\right),$$

which may be positive or negative depending on the relative phases of the matrix elements.

For the ideal symmetric 4×4 unitary

$$U_{mn} = \frac{1}{2}H_{mn},$$

where $H_{mn} = \pm 1$ is the normalized Hadamard matrix, each element satisfies $|U_{mn}|^2 = 1/4$.

Evaluating Eq. (3.4.5) yields two distinct classes of coincidence outcomes:

- **Enhanced pairs (constructive interference):**

$$P_{ij}^{\text{ind}} = \frac{3}{16}.$$

- **Suppressed pairs (destructive interference):**

$$P_{ij}^{\text{ind}} = \frac{1}{16}.$$

Thus, the multiport produces a non-uniform coincidence landscape: certain detector pairs exhibit increased probability relative to the classical case, while others are suppressed. This structured redistribution of coincidence events constitutes the multiport generalization of the HOM effect.

3.4.3 Distinguishable Photon Case

When the photons are fully distinguishable (e.g., large temporal delay), the interference term vanishes. The coincidence probability reduces to the incoherent sum of independent alternatives:

$$P_{ij}^{\mathrm{dist}} = |U_{i1}U_{j3}|^2 + |U_{j1}U_{i3}|^2. \tag{3.4.6}$$

For the symmetric unitary, each term contributes 1/16, yielding

$$P_{ij}^{\mathrm{dist}} = \frac{1}{8}, \tag{3.4.7}$$

independent of the detector pair (i, j).

The distinguishable-photon case therefore produces a uniform coincidence distribution across all output pairs. This flat distribution serves as the classical baseline for visibility calculations. The HOM visibility for a given detector pair, introduced before in Eq. 2.3.11, is now written as

$$\mathcal{V}_{ij} = \frac{P_{ij}^{\mathrm{dist}} - P_{ij}^{\mathrm{ind}}}{P_{ij}^{\mathrm{dist}}}. \tag{3.4.8}$$

For suppressed channels,

$$\mathcal{V}_{ij} = \frac{1/8 - 1/16}{1/8} = \frac{1}{2},$$

while enhanced channels exhibit negative visibility of the same magnitude, reflecting constructive interference.

The plot in Fig. 3.4.1 shows the simulated coincidence probabilities for two indistinguishable photons passing through a 4×4 BS, exhibiting characteristic bunching (dips) and anti-bunching (peaks) behavior. The Gaussian envelope in the plot models the temporal overlap of the photon wave packets, which governs the visibility of these interference effects and directly determines the photons' degree of indistinguishability.

In summary, the symmetric 4×4 multiport transforms the standard HOM dip into a structured interference pattern characterized by analytically predictable coincidence probabilities of 3/16 and 1/16 for indistinguishable photons, compared to a uniform 1/8 distribution in the distinguishable limit. This theoretical structure provides the quantitative benchmark for the experimental measurements presented in Chapter 4.

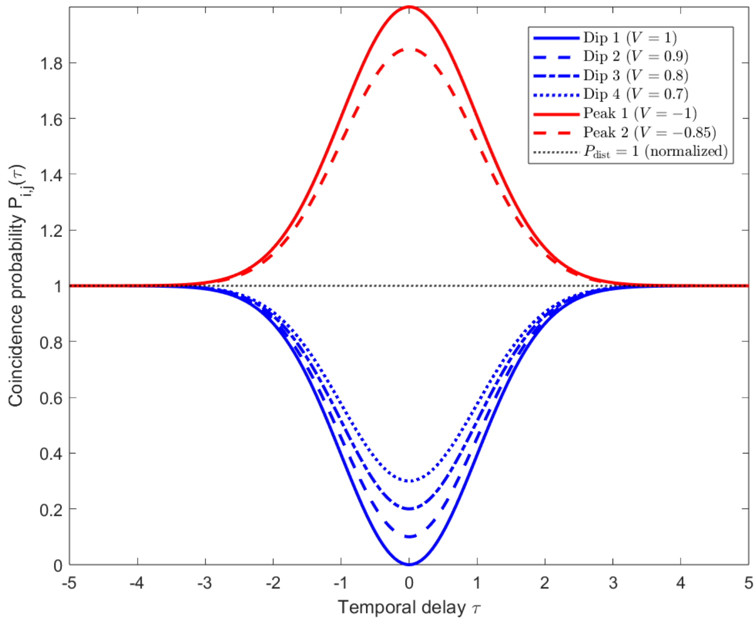

Figure 3.4.1: Simulated multiport HOM interference for different output pairs. Suppressed channels (destructive interference) exhibit dips, while enhanced channels (constructive interference) exhibit peaks, reflecting the coexistence of negative and positive interference contributions in a symmetric multiport transformation. The curves are normalized such that the distinguishable-photon baseline is set to $P_{\rm dist} = 1$, enabling direct comparison of visibilities across channels. In the physical 4×4 system, these correspond to $P_{i,j}^{\rm dist} = 1/8$, $P_{i,j}^{\rm ind} = 1/16$ (suppressed) and 3/16 (enhanced). Visibilities are set to distinct values for clarity. In the ideal symmetric case, suppressed pairs have $V = +1/2$ and enhanced pairs have $V = -1/2$ relative to the uniform classical baseline $P^{\rm dist} = 1/8$.

3.4.4 Fisher information for coincidence measurements

The sensitivity of HOM interference to temporal delay can be rigorously quantified using the Fisher information framework (see Sec. 2.3.7). For a binary detection outcome (coincidence or no-coincidence) in output channel (k, l), the Fisher information for estimating the delay τ is

$$F_{kl}(\tau) = \frac{1}{P_{kl}(\tau)\,[1 - P_{kl}(\tau)]} \left(\frac{dP_{kl}(\tau)}{d\tau} \right)^2 . \tag{3.4.9}$$

The coincidence probability as a function of temporal delay is

$$P_{kl}(\tau) = P_{kl}^{\rm dist}\,[1 - V_{kl}\,G(\tau)]\,, \tag{3.4.10}$$

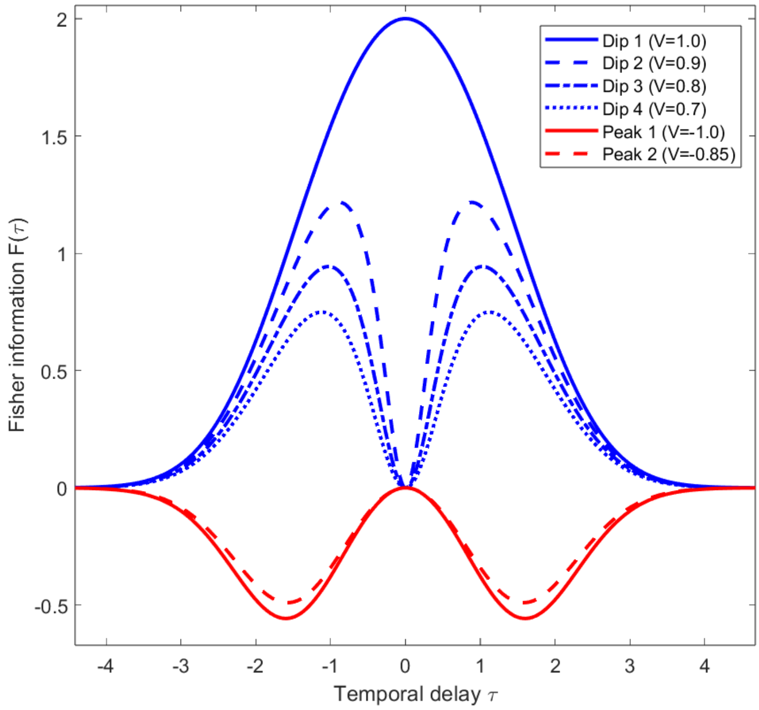

Figure 3.4.2: Fisher information as a function of temporal delay for the simulated multiport HOM interference from Fig. 3.4.1.

where V_{kl} is the effective visibility (positive for dips, negative for peaks) and $G(\tau) = \exp(-\tau^2/2\sigma_\tau^2)$ is the Gaussian envelope set by the photon coherence time σ_τ.

Substituting Eq. (4.3.1) and evaluating the derivative yields

$$F_{kl}(\tau) = \frac{\left(P_{kl}^{\mathrm{dist}}\right)^2 V_{kl}^2 \frac{\tau^2}{\sigma_\tau^4} e^{-\tau^2/\sigma_\tau^2}}{\left[P_{kl}^{\mathrm{dist}}(1 - V_{kl}e^{-\tau^2/2\sigma_\tau^2})\right]\left[1 - P_{kl}^{\mathrm{dist}}(1 - V_{kl}e^{-\tau^2/2\sigma_\tau^2})\right]}. \tag{3.4.11}$$

The Fisher information vanishes at $\tau = 0$ – despite the coincidence rate being extremal there – because $dP/d\tau = 0$ at the dip center. It is maximized at a finite delay corresponding to the steepest slope of the interference curve, as illustrated in Fig. 3.4.2. Maximizing the leading factor $\tau^2 e^{-\tau^2/\sigma_\tau^2}$ gives the optimal operating point

$$\tau_{\mathrm{opt}} \approx \pm\sigma_\tau, \tag{3.4.12}$$

i.e., the highest sensitivity is achieved when the relative delay equals one photon coherence time.

3.5 Experimental Implementation

This section describes the experimental realization of the 4×4 multiport interference platform. The objective is to implement the theoretical model developed in Section 3.4 under controlled and stable laboratory conditions, enabling precise measurement of two-photon interference and inter-core temporal offsets.

The experimental platform integrates three main subsystems: (i) a pulsed photon-pair source based on spontaneous parametric down-conversion (SPDC), (ii) a Mach–Zehnder-type interferometer (MZI) in which a multicore fiber implements a fixed four-mode unitary transformation, and (iii) a time-resolved single-photon detection and coincidence analysis stage. Together, these subsystems form a coherent architecture for investigating two-photon interference in a multiport linear optical network.

3.5.1 Photon-Pair Source

Photon pairs are generated via Type-II spontaneous parametric down-conversion in a periodically poled potassium titanyl phosphate (PPKTP) crystal, as shown in Fig. 3.5.1. The nonlinear interaction is driven by a mode-locked Ti:Sapphire ultrafast laser (Mai Tai One Box) operating at a central wavelength of 775 nm with a repetition rate of 80 MHz and a maximum average output power of 3 W. In practice, the pump power delivered to the nonlinear crystal is on the order of 100 mW. The beam is routed through a set of mirrors and polarization optics, including polarizing beam splitters (PBS) and wave plates, allowing precise attenuation and control of the transmitted power. Additional coupling losses in free-space and fiber stages further reduce the optical power incident on the crystal. This controlled attenuation ensures operation in the spontaneous regime (pair-generation probability per pulse $p \ll 1$), suppressing higher-order multi-pair emission while maintaining stable coincidence rates.

In the low-gain regime, the SPDC process produces photon pairs satisfying energy conservation [150, 151],

$$\omega_p = \omega_s + \omega_i, \tag{3.5.1}$$

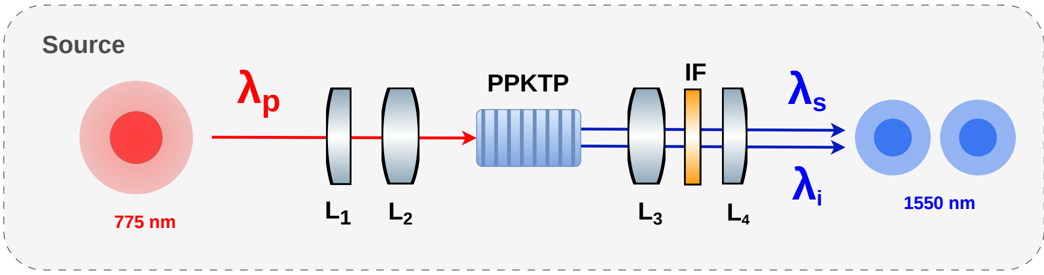

Figure 3.5.1: SPDC source.

with degenerate emission at 1550 nm. The biphoton state can be written as

$$|\psi\rangle \approx |0\rangle + \gamma \int d\omega_s d\omega_i \, f(\omega_s, \omega_i) \hat{a}_s^\dagger(\omega_s) \hat{a}_i^\dagger(\omega_i) |0\rangle, \tag{3.5.2}$$

where $f(\omega_s, \omega_i)$ is the joint spectral amplitude determined by the pump envelope and phase-matching function.

After generation, residual pump light is removed, and the orthogonally polarized signal and idler photons are separated using a PBS. Spectral filtering and single-mode fiber coupling are employed to improve spectral purity and spatial mode overlap, which are essential for high-visibility two-photon interference.

3.5.2 Mach–Zehnder-Type Multicore Interferometer

The interferometric stage is formed by directing the signal and idler photons into two spatially distinct arms prior to injection into the multicore fiber. This configuration is equivalent to a Mach–Zehnder interferometer, where the MCF acts as the recombination element implementing a four-mode unitary transformation $U \in U(4)$ [152].

A variable optical delay line in one arm introduces a controllable temporal offset τ between the photons. Temporal overlap is achieved when $\tau = 0$, enabling HOM interference within the MCF network.

By scanning the relative delay τ and assuming Gaussian spectral profiles, two-photon interference curves are obtained:

$$C(\tau) = C_0 \left[1 - V \exp\left(-\frac{\tau^2}{2\sigma^2} \right) \right], \tag{3.5.3}$$

where V is the measured visibility and σ is related to the photon coherence time.

The interferometer therefore serves both as a platform for multiport quantum interference and as a sensitive probe of spectral purity, temporal overlap, and differential propagation effects within the multicore device.

3.5.3 Single-Photon Detection and Timing Electronics

The output modes of the multicore interferometer are monitored using superconducting nanowire single-photon detectors (SNSPDs) optimized for 1550 nm operation [153]. SNSPDs provide high system detection efficiency, low dark count rates, and timing jitter typically below 100 ps, enabling high signal-to-noise ratio coincidence measurements.

Detection events are amplified and recorded using a time-tagging module with picosecond resolution. Operating in free-running mode, the SNSPDs allow continuous acquisition without gating synchronized to the pump laser.

Coincidences between detector pairs are identified within a temporal window Δt, and the coincidence rate is computed as

$$R_{ij} = \frac{N_{ij}}{T}, \tag{3.5.4}$$

where N_{ij} is the number of coincidence events detected during integration time T.

Accidental coincidences arise primarily from multi-pair emission and scale approximately as

$$R_{\text{acc}} \propto R\, p^2 \eta_i \eta_j, \tag{3.5.5}$$

with $R = 80$ MHz the repetition rate. Because SNSPD dark count rates are negligible compared to true coincidence rates, accidental contributions are dominated by higher-order SPDC events.

3.5.4 Integrated System Operation

A schematic representation of the complete experimental system is shown in Fig. 3.5.2. The diagram is organized from left to right, following the propagation of the optical field. The complete experimental system operates as a unified two-photon interferometric platform. The photon-pair source defines the spectral and temporal properties of the quantum state; the Mach–Zehnder-type interferometer controls relative arrival time and spatial mode mixing; and the SNSPD-based detection stage resolves output correlations with sub-coherence-time precision.

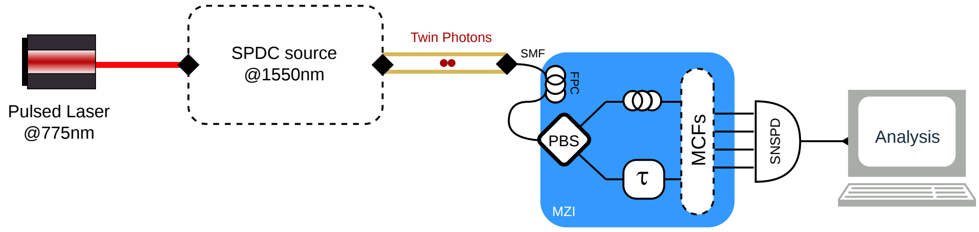

Figure 3.5.2: Pulsed 775 nm light from a Mai Tai One Box pumps a nonlinear crystal to generate Type-II SPDC photon pairs at 1550 nm. After polarization separation and relative delay control τ, photons are injected into a multicore fiber implementing a four-mode unitary transformation. Output modes are detected by SNSPDs, and time-tagged coincidences yield two-photon interference patterns.

By scanning the temporal delay and recording coincidence rates across different output port combinations, the experiment provides quantitative access to:

- photon indistinguishability via HOM visibility,
- symmetry and fidelity of the implemented unitary transformation,
- sensitivity to differential propagation delays within the multicore fiber.

This architecture enables controlled investigation of multiport quantum interference and establishes the experimental foundation for subsequent characterization and metrological analysis.

Summary

In this chapter, we have established a comprehensive framework for implementing stable multiport quantum interference using multicore optical fibers. Motivated by the need for scalable and phase-stable interferometric architectures, we introduced multicore fibers as a natural platform for coherently manipulating multiple spatial modes within a compact and environmentally robust structure.

We first described the physical principles underlying weakly coupled multicore fibers, emphasizing their ability to provide parallel single-mode channels with strong common-mode stability. The presence of residual differential group delay between cores was identified as a key physical parameter, setting the stage for its characterization through quantum interference techniques.

Building on this architecture, we introduced the 4×4 multicore fiber beam splitter as the central interferometric element of the platform. Using coupled-mode theory, we showed how controlled evanescent coupling within a finite interaction region gives rise to a well-defined unitary transformation. In the symmetric regime, this transformation approximates a balanced multiport operation, enabling uniform amplitude redistribution across spatial modes while preserving quantum coherence.

We then developed a theoretical model for two-photon interference in the multiport device, extending the Hong–Ou–Mandel formalism to a four-mode system. The analysis revealed a structured coincidence landscape characterized by enhanced and suppressed detection probabilities, arising from the coherent superposition of indistinguishable two-photon paths. This behavior constitutes a direct generalization of the HOM effect and provides a sensitive probe of both photon indistinguishability and the symmetry of the implemented unitary transformation.

Finally, we described the experimental implementation of the platform, integrating a pulsed SPDC photon-pair source, a Mach–Zehnder-type interferometric configuration, and high-efficiency single-photon detection. This system enables precise control of temporal overlap and direct measurement of multiport interference patterns, establishing a robust experimental basis for quantitative analysis.

Overall, the multicore fiber platform developed in this chapter provides a scalable, stable, and fiber-integrated approach to multiport quantum interference. The combination of intrinsic phase stability, controlled mode mixing, and sensitivity to temporal delays makes this system particularly well suited for precision metrology applications.

In the following chapter, we exploit these properties to perform high-precision measurements of inter-core skew, using multiport Hong–Ou–Mandel interference as a sensitive temporal probe.

Chapter 4

Sub-picosecond Inter-core Skew Characterization in Multicore Fibers via Hong–Ou–Mandel Interference

4.1 Introduction

Multicore fibers (MCFs) have emerged as a key enabling technology for next-generation optical communication systems and quantum photonic networks, offering a scalable route to increased capacity through space-division multiplexing (SDM), while simultaneously enabling the distribution of quantum states across spatially distinct channels within a single cladding [14, 22].

In classical optical communications, MCFs support petabit-class transmission [154], joint-core coherent detection, and radio-over-fiber applications requiring precise timing synchronization across cores [155, 156]. Recent demonstrations include submarine multicore systems [157], high-capacity long-haul links [158], and advanced enabling components [159].

In the quantum domain, the shared cladding of MCFs provides intrinsic phase stability, enabling high-dimensional entanglement distribution [160, 161], parallel quantum channels [162, 163], and integrated multiport photonic circuits [21, 125]. Additionally, correlated noise across cores has enabled sub-femtosecond stabilization in quantum networks [164].

A key parameter limiting performance in both classical and quantum applications is the *inter-core skew* (ICS), defined as the differential group delay (DGD) between signals propagating in different cores. ICS arises from variations in effective refractive index, stress-induced birefringence, and environmental perturbations.

In SDM systems, ICS increases digital signal processing complexity and degrades joint-core processing [155, 156], while in quantum systems it introduces temporal distinguishability, reducing interference visibility. Importantly, ICS does not accumulate deterministically; instead, it is dominated by stochastic variations [165], making accurate measurement essential.

Conventional measurement techniques such as correlation optical time-domain reflectometry (C-OTDR) [166, 167] and white-light interferometry [168, 165] are limited to resolutions of 10–20 ps. These are insufficient for sub-picosecond applications.

In this chapter, we demonstrate that two-photon Hong-Ou-Mandel interference [7] in a fiber-integrated 4×4 multiport beam splitter provides ICS measurement with a demonstrated precision of ± 0.11 ps and a fundamental Cramér–Rao precision limit in the femtosecond range. We use photon pairs from spontaneous parametric down-conversion (SPDC) through a commercial four-core fiber (Fibercore SM-4C1500(8.0/125)/001) and a fiber-integrated MCF beam splitter [125]. The position of each HOM dip or peak directly encodes the differential group delay between a core pair; Gaussian fits across all twelve input combinations yield the complete ICS profile, and the root-mean-square skew over lengths from 7.7 m to 1300 m provides the first direct multi-length validation of the expected $\sigma_\tau \propto \sqrt{L}$ scaling. HOM interferometry requires no phase stabilization—the coincidence dip depends only on the second-order temporal envelope, immune to first-order path fluctuations [169]—making it robust for measurements through long installed fibers where classical interferometric methods would require active stabilization [170, 63]. It is precisely this phase-insensitivity that enabled the multi-length scaling demonstration reported here: perturbation-sensitive classical methods are impractical for long installed fibers, and prior ICS measurements have not fitted the $\sqrt{L}$ dependence across a range of fiber lengths [12].

4.2 Inter-core Skew: Physical Origin and Scaling

4.2.1 Definition and Physical Interpretation

Inter-core skew quantifies the temporal delay difference between optical signals propagating through different cores of an MCF [12], as illustrated in Fig. 4.2.1. ICS originates from core-to-core variations in group velocity arising from small structural or refractive index differences between cores, stress-induced birefringence, and environmental perturbations such as bending or temperature fluctuations [171].

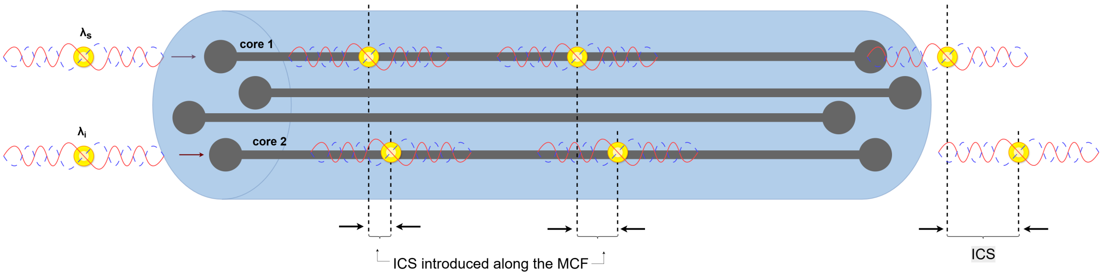

Figure 4.2.1: Illustration of ICS accumulation in a MCF. Identical pulses propagate (here from left to right) through different cores of the MCF. Because both pulses have the same frequency spectrum, any accumulated differential delay arises solely from core-dependent group velocity variations.

A signal propagating through core k of an MCF of length L accumulates an absolute group delay

$$\tau_k(L) = \frac{L n_{g,k}}{c}, \tag{4.2.1}$$

where $n_{g,k}$ is the group refractive index of core k, and c is the speed of light in vacuum. The ICS between cores j and k is the *difference* of these absolute delays,

$$\tau_{jk}(L) \equiv \tau_j(L) - \tau_k(L) = \frac{L}{c}(n_{g,j} - n_{g,k})\,. \tag{4.2.2}$$

Note that $\tau_{jk} = -\tau_{kj}$; throughout this chapter we report the magnitude $|\tau_{jk}|$.

4.2.2 Stochastic Accumulation and Random-Walk Model

A purely deterministic refractive-index mismatch would produce an ICS scaling linearly with L. Experiments consistently show that this simple scaling is not observed [165]. Rather, ICS is dominated by stochastic, spatially-varying imperfections that produce local positive and negative contributions to the differential delay. Lee *et al.* [165] found that splicing rotations designed to cancel ICS were unsuccessful, providing direct evidence of the random character of ICS accumulation.

This behavior can be modeled by treating each absolute delay as a one-dimensional zero-mean random walk along the fiber. The pairwise difference $\tau_{jk} = \tau_j - \tau_k$ is then itself a zero-mean random walk whose RMS grows as

$$\sigma_\tau(L) = \kappa\sqrt{L}, \tag{4.2.3}$$

with κ the intrinsic ICS coefficient of the fiber (units: ps/$\sqrt{\text{km}}$). This square-root scaling is formally analogous to the random-walk model of polarization mode dispersion (PMD) in single-mode fibers [172, 173, 171], and is consistent with ICS measurements reported in homogeneous MCFs [12], though a direct multi-length fit to the scaling law had not previously been demonstrated.

4.2.3 Measurement Strategy

To go from pairwise delays to the RMS ICS, we use the fact that a four-core fiber there are $\binom{4}{2} = 6$ unordered core pairs. For each pair (j, k) we perform measurements with both input orderings, yielding two delay-stage positions d_{jk} and d_{kj} (12 ordered measurements in total). Taking the half-difference (Eq. 4.2.7) cancels the common arm imbalance δ (see below) and gives the 6 unsigned ICS magnitudes $|\tau_{jk}|$, one per unordered pair. Their RMS,

$$\sigma_\tau(L) = \sqrt{\frac{1}{6}\sum_{\{j,k\}} |\tau_{jk}|^2}, \tag{4.2.4}$$

characterizes the spread of delays across the core ensemble at length L. The measured RMS also includes a fixed, length-independent contribution from single-mode fiber pigtails and fan-in/fan-out connectors at the interferometer inputs. We therefore fit

$$\sigma_\tau(L) = \kappa\sqrt{L} + c, \tag{4.2.5}$$

where c is a length-independent offset and κ provides an intrinsic, setup-independent measure of fiber-induced ICS.

To extract the ICS estimate, we must cancel out the offsets due to arm-length differences. Let the two SMF interferometer input arms have fixed delays δ_{I} and δ_{II} arising from different SMF pigtail lengths, and define the arm imbalance $\delta \equiv \delta_{\mathrm{II}} - \delta_{\mathrm{I}}$. Let the delay stage position be d (in arm I). For input pair (j, k), the HOM dip appears at delay position d_{jk} satisfying

$$\delta_{\mathrm{I}} + d_{jk} + \tau_j = \delta_{\mathrm{II}} + \tau_k, \tag{4.2.6}$$

giving $d_{jk} = \delta + \tau_{jk}$. Swapping inputs gives $d_{kj} = \delta - \tau_{jk}$. Taking the half-difference eliminates δ:

$$\tau_{jk} = \frac{d_{jk} - d_{kj}}{2}. \tag{4.2.7}$$

This is the ICS extracted for each of the 6 unordered core pairs using both input orderings. The sum $d_{jk} + d_{kj} = 2\delta$ provides a consistency check on the arm imbalance.

4.3 Multiport HOM interference in a 4×4 beam splitter

4.3.1 Coincidence probability and Visibility

In the HOM experiment we use a 4×4 multiport beam splitter, which implements a unitary transformation well-described by a normalized 4×4 real Hadamard matrix [125]. The input photon creation operators $\hat{a}_k^\dagger$ transform to output operators $\hat{b}_l^\dagger = \sum_k U_{lk} \hat{a}_k^\dagger$, where the $U_{lk} = \pm 1/2$, as seen in Chapter 3.

For two photons in input modes i and j with relative delay τ, the coincidence probability between output ports k and l is

$$P_{kl}(\tau) = P_{kl}^{\mathrm{dist}} \big[1 - V_{kl}\, G(\tau)\big], \tag{4.3.1}$$

where V_{kl} is the effective channel visibility and $G(\tau) = \exp(-\tau^2/2\sigma_\tau^2)$ is the Gaussian envelope set by the photon coherence time σ_τ. The sign of V_{kl} is determined by the relative signs of the Hadamard matrix elements for ports k and l: channels for which $U_{ki}U_{lj}$ and $U_{li}U_{kj}$ share the same sign give destructive interference (bunching dip, $V_{kl} > 0$); opposite signs give constructive interference (anti-bunching peak, $V_{kl} < 0$). For a Fock-state input the ideal visibility magnitude is $|V_{kl}| = 1$ for both types.

4.3.2 Extraction of ICS from HOM Dips

In the presence of ICS, a differential group delay τ_{jk} between the two input cores shifts the HOM feature center by exactly τ_{jk} along the delay axis without altering its shape or width. ICS therefore extracted from the position of the dip or peak, making the method somewhat insensitive to loss imbalance, spectral distinguishability, or multi-photon noise, which affect visibility but not center position. Performing HOM measurements for all 12 input core-pair combinations yields the complete differential delay profile of the fiber.

4.4 Precision limits

In this experiment τ_{jk} is unknown and can be much larger than the dip width σ_τ, so the measurement is performed by scanning the delay stage and locating the dip center by Gaussian fitting. The precision limit of center estimation for a Gaussian profile is set by the Cramér–Rao bound (CRB) [174]. As seen in Sec. 2.3.7, for binary coincidence trials, the Fisher information is

$$F_{kl}(\tau) = \frac{1}{P_{kl}(\tau)\,[1 - P_{kl}(\tau)]} \left(\frac{dP_{kl}(\tau)}{d\tau}\right)^2 . \tag{4.4.1}$$

Since the delay τ_{jk} is located by accumulating data over different delay positions, the total Fisher information is obtained through the integral $\mathcal{I}_F = \int_{-\infty}^{\infty} F_{kl}(u)\,du$, which holds since the scan range $\mathcal{R} \gg \sigma_\tau$ and the step size is much smaller than σ_τ [174, 175]. Substituting the Gaussian dip model Eq. (4.3.1), the scan CRB for locating the dip center with N total coincidence counts is [174]

$$\Delta\tau_{\mathrm{CRB}} = \frac{\sigma_\tau}{\sqrt{N_{\mathrm{eff}}\, J_F}}, \tag{4.4.2}$$

where $N_{\mathrm{eff}} = N\,\sigma_\tau/\mathcal{R}$ is the effective count density within one dip width and $J_F = \sigma_\tau\,\mathcal{I}_F$ is a dimensionless shape factor. Narrower dips (broader photon spectrum) improve precision by reducing σ_τ, and $J_F \propto V^2$, so higher visibility monotonically improves precision. For the SPDC measurements reported here, the scan range is $\mathcal{R} = 1.8\,\mathrm{ps}$ and coincidence counts per scan range from $N \approx 1.5 \times 10^5$

to 3.5×10^5, giving effective count densities $N/\mathcal{R} \approx 8\times10^4$ to $2\times10^5\,\mathrm{ps}^{-1}$. Summing over all six output pairs with $\bar{V} \approx 0.92$ and $\sigma_\tau \approx 0.25\,\mathrm{ps}$, the per-channel Cramér–Rao bound ranges from 0.93 to 1.94 fs. The conservative precision estimate of $\pm0.11\,\mathrm{ps}$ reported below is thus about two orders of magnitude above the fundamental quantum limit, which could be approached with more precise delay control. We note that the demonstrated $\pm0.11\,\mathrm{ps}$ precision is more than adequate for the random-walk scaling measurement reported in Section 4.6; the Fisher information analysis motivates future experiments targeting the femtosecond regime.

4.5 Experimental implementation

4.5.1 Photon-pair source and interferometer

The experimental setup is shown in Fig. 4.5.1. Photon pairs were generated via type-II SPDC in a periodically poled $KTiOPO_4$ (PPKTP) crystal pumped by a mode-locked laser at 775 nm with repetition rate $f_{\mathrm{rep}} = 80\,\mathrm{MHz}$ and $\sim70\,\mathrm{mW}$ average power. Degenerate photon pairs centered at 1550 nm were separated by a polarizing beam splitter (PBS) and spectrally filtered by a 30 nm interference filter (IF) before coupling into single-mode fibers (SMFs).

The photons were routed through a modified Mach–Zehnder interferometer (TPI) with a variable free-space delay line providing up to 15 mm path difference ($\approx 50\,\mathrm{ps}$). Both photons were injected into the MCF of length L via the MUX, and then sent to interfere in the MCF-BS. To study ICS as a function of length, the measurement was repeated for six separate fiber segments ($L = 7.7, 12.7, 49.7, 72.7, 114.7$, and 187.7 m); each segment is an independently handled cut of Fibercore SM-4C1500(8.0/125)/001 four-core fiber [176] with a square core arrangement, 50 μm nominal core spacing, 125 μm cladding diameter, and mode field diameter of 7.4–8.5 μm at 1550 nm (single-mode operating window 1520–1650 nm). Inter-core crosstalk during propagation is negligible, so that mode mixing occurs only in the engineered beam-splitter coupling region.

The multiport beam splitter is a 4×4 MCF-BS implementing the unitary Hadamard transformation via evanescent coupling between the four cores over a finite interaction length, as described and characterized in Refs. [125, 177]. Input

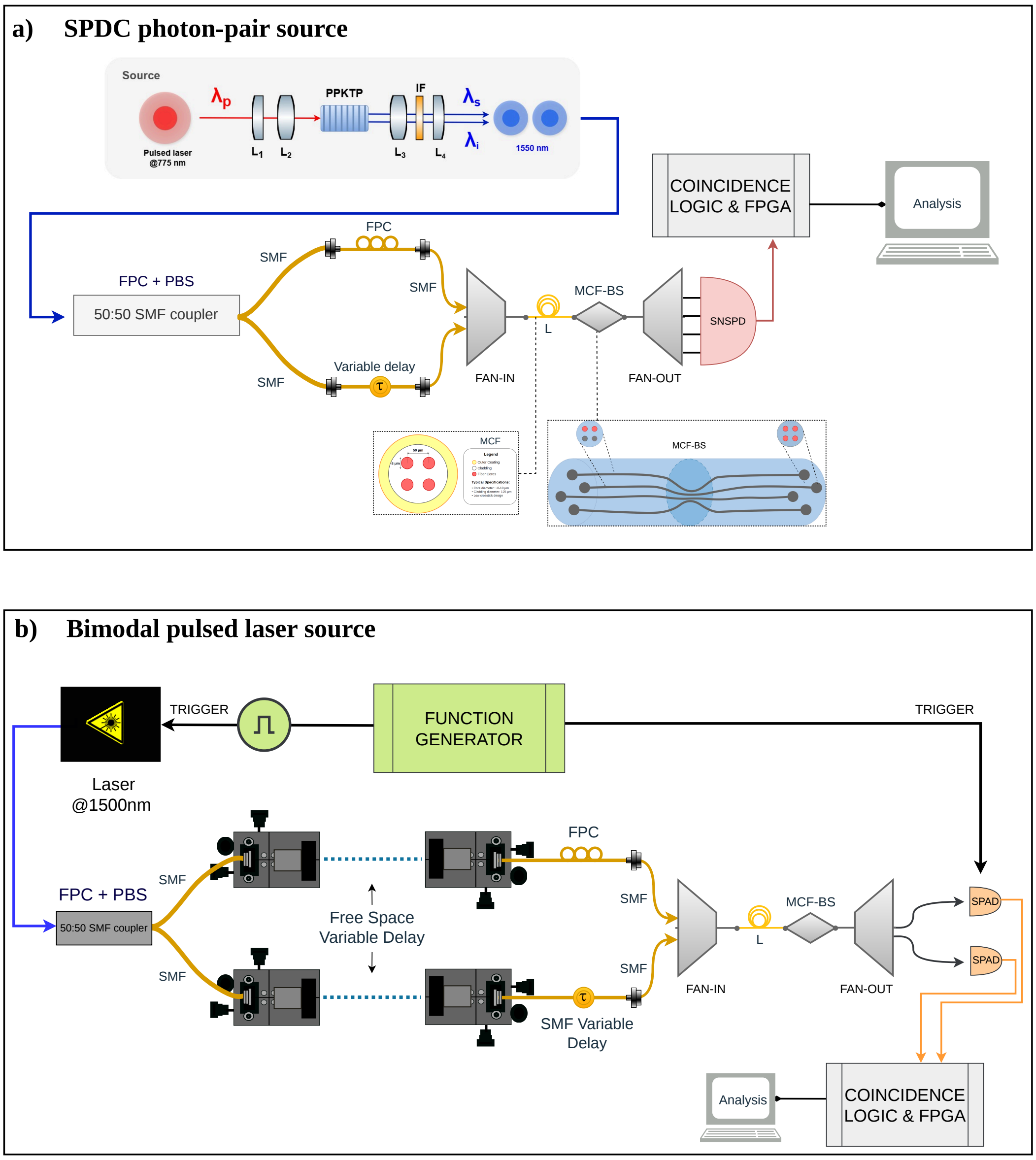

Figure 4.5.1: a) Experimental setup for HOM interference using SPDC source. The photons are coupled into SMFs, separated by a variable delay τ, and injected into the four-core MCF via a FAN-IN. Coincidence counts are registered by SNSPDs and an FPGA. b) Experimental setup for HOM interference using a weak laser source. Additional optical delay lines were added. See text for additional details.

and output cores are interfaced via fiber-optic MUX and DEMUX fan-in/fan-out devices, as shown in Fig. 4.5.1.

The four output modes were detected by superconducting nanowire single-photon detectors (SNSPDs). Coincidence events were registered by an FPGA counting system. For the pulsed SPDC source, accidental coincidences accumulate at the rate $R_{\mathrm{acc}} = (R_A \cdot R_B)/f_{\mathrm{rep}}$, where R_A and R_B are the single-channel detection rates. Accidentals have been subtracted from all SPDC data.

The $\approx 100\,\mathrm{ps}$ delay range sets a practical upper bound on observable ICS: core pairs whose differential delays exceed this limit will not show an HOM feature within the scan. This explains the progressive reduction in visible dip/peak combinations at longer fiber lengths (Section 4.6). The delay line was extended to $> 10\,\mathrm{cm}$ ($> 670\,\mathrm{ps}$) to enable measurements at the longer installed fiber lengths at the cost of increased losses; results are reported in Section 4.6.

4.5.2 Bimodal pulsed laser source for long installed fibers

For the field-installed 1300 m fiber segment, ICS is still measured via HOM two-photon interference, but using a pulsed laser source in place of SPDC. This substitution is necessary because the SPDC source becomes impractical at this length due to channel losses, which are large and dominated not by fiber propagation but by MCF-to-MCF connectors and splices. The bulk of the 10.70 dB of channel loss arises from butt-coupled MCF connectors (individual insertion loss 0.3–3.1 dB, requiring manual rotational alignment of the square core pattern before each connection), fusion splices, and the DEMUX fan-out. For SPDC, both photons must survive their respective arms independently, so a per-arm loss of $\sim 11\,\mathrm{dB}$ reduces coincidence rates by a factor of ~ 160, making measurements impractical.

The setup is shown schematically in Fig. 4.5.1(b). A single $\sim 300\,\mathrm{ps}$ telecom laser pulse is split at the SMF coupler into two arms; both arms traverse the MCF under test (one per core), accumulate the inter-core delay τ_{jk}, and recombine at a second SMF coupler acting as the HOM beam splitter. The two outputs are detected by InGaAs SPADs triggered by the function generator driving the laser at $f_{\mathrm{rep}} = 1\,\mathrm{MHz}$.

The laser has a multi-mode longitudinal mode structure visible as a sinusoidal beating of the fast single count oscillations along the delay axis. The beat period is $T_{\text{beat}} \approx 10\,\text{ps}$, corresponding to a mode spacing $\delta\nu \approx 100\,\text{GHz}$ ($\approx 0.8\,\text{nm}$ at $1550\,\text{nm}$).

Two-photon decomposition and the 50% visibility ceiling. The physics of this measurement is most clearly understood by considering the two-photon component of the coherent pulse, which dominates the coincidence signal. When a two-photon pulse is split at the input $50:50$ coupler, two outcomes are equally likely: (i) one photon takes each arm (probability $\frac{1}{2}$), leading to standard HOM interference at the output coupler; (ii) both photons take the same arm (probability $\frac{1}{2}$), forming a $|2,0\rangle$ or $|0,2\rangle$ state that produces N00N-state interference at the output coupler with fringe period $\lambda/2 \approx 775\,\text{nm}$ in path length. The coincidence probability is a combination of both contributions: $P_{\text{coinc}}(\tau) = \frac{1}{2}P_{\text{HOM}}(\tau) + \frac{1}{2}P_{\text{N00N}}(\tau)$. The N00N fringes oscillate at period $\lambda/2 \approx 775\,\text{nm}$, sensitive to sub-wavelength optical path fluctuations. Ambient thermal and mechanical drifts during the $\approx 30\,\text{s}$ integration at each delay point cause path-length excursions of several micrometers, sweeping through multiple fringe cycles and averaging the N00N contribution to its mean: $\langle P_{\text{N00N}}\rangle = \frac{1}{2}$. The HOM envelope width $\sigma_\tau c \approx 120\,\mu\text{m}$ is four orders of magnitude larger than $\lambda/2$, so the same drift is entirely negligible for the HOM term. The measured coincidence rate therefore becomes

$$R_c(\tau) = R_c^{\infty}\left[\frac{1}{2} + \frac{1}{2}\left(1 - G_{\text{HOM}}(\tau)\right)\right] = R_c^{\infty}\left[1 - \frac{1}{2}\,G_{\text{HOM}}(\tau)\right], \tag{4.5.1}$$

where $G_{\text{HOM}}(\tau)$ is the HOM envelope (Gaussian modulated by the bimodal beats). The maximum visibility is therefore $V_{\max} = 50\%$, and is unchanged by the bimodal spectrum. The bimodal beats enter through $G_{\text{HOM}}(\tau)$:

$$G_{\text{HOM}}(\tau) = \cos^2\!\left(\frac{\pi\tau}{T_{\text{beat}}}\right)\exp\left(-\frac{\tau^2}{2\sigma_{\text{pulse}}^2}\right), \tag{4.5.2}$$

where $\sigma_{\text{pulse}} \approx 127\,\text{ps}$ for a transform-limited $\sim 300\,\text{ps}$ pulse. The ICS between a core pair shifts the entire pattern by τ_{jk}. In practice, a coarse delay scan is first performed to identify the beat period at which fringe visibility is maximum, locating τ_{jk} to within $\sim T_{\text{beat}}$. A fine-step scan is then performed over a single beat period centered on this maximum, and a fit to the $\cos^2$ envelope of Eq. (4.5.2) extracts the fringe-center position, giving τ_{jk} with an effective precision $\sigma_{\text{eff}} \approx T_{\text{beat}}/2\pi \approx 1.6\,\text{ps}$, far below the $\sim$300 ps pulse width.

The laser power is adjusted so that link attenuation reduces the mean photon number to $\mu_{\text{eff}} \approx 0.5$ photons/pulse per arm at the detectors, the regime where the two-photon decomposition above applies. This corresponds to $R_A \approx R_B \approx 50\,000$ cps per detector and $R_{\text{coinc}} \approx 2600$ cps, regardless of which link is under test. We note that here the same connector losses that render SPDC impractical thus serve as a natural attenuator. Dark-count accidentals ($\lesssim$0.01 cps) were negligible.

We therefore present two complementary measurement regimes: (A) short laboratory fibers (7.7–187.7 m) using SPDC photon pairs and (B) long field-deployed fibers (1300 m) using the pulsed laser.

4.6 Results and discussion

4.6.1 Multiport HOM interference, visibilities, and dip-center extraction

As an example of the extracted data using HOM interference of SPDC photon pairs, Fig. 4.6.1(a) shows coincidence rates for a $L = 12.7$ m MCF segment and one input core-pair combination (a_3, a_4) as a function of relative delay τ. The coincidence curves display the characteristic multiport HOM landscape: four output pairs (AC, AD, BC, BD) show bunching dips and two pairs (AB, CD) show anti-bunching peaks, in quantitative agreement with the predictions for the Hadamard transformation described in Section 4.3. The dip-center positions are extracted by fitting each coincidence curve to a Gaussian,

$$y = a + b \exp\left(-\frac{(x-d)^2}{2\sigma_\tau^2}\right), \tag{4.6.1}$$

where d gives the dip-center delay, σ_τ is the width, b is the amplitude, and a is the baseline. The visibility is $V = |b|/a$, and the center position d is insensitive to visibility degradation from loss or spectral effects.

As shown in Fig. 4.6.2, the Fisher information exhibits pronounced peaks at delay values corresponding to the steepest regions of the HOM interference curves, where

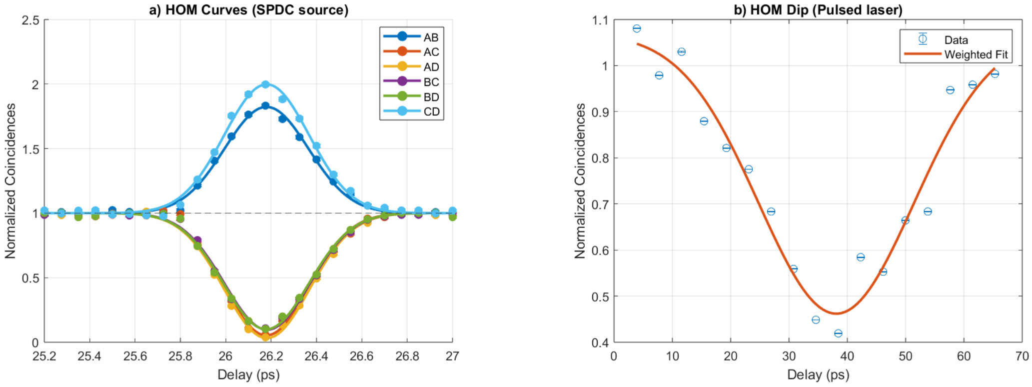

Figure 4.6.1: HOM interference data. (a) Normalised coincidence counts for all six output pairs as a function of relative delay for a 12.7 m MCF, input combination a_3,a_4, using the SPDC source. Solid lines are Gaussian fits. Statistical error bars are smaller than the data points and not visible at this scale. Coincidence curves show bunching dips (AC, AD, BC, BD) and anti-bunching peaks (AB, CD) as predicted by the 4×4 Hadamard transformation. Fit parameters and visibilities are listed in Table 4.6.1. (b) Coincidence rate as a function of relative delay for the 1300 m installed fiber, input combination a_3,a_4 for a single pair of outputs, using the bimodal pulsed laser source. The modulated envelope reflects the $\cos^2$ beat structure of Eq. (4.5.2); the solid line is a fit used to extract τ_{jk}.

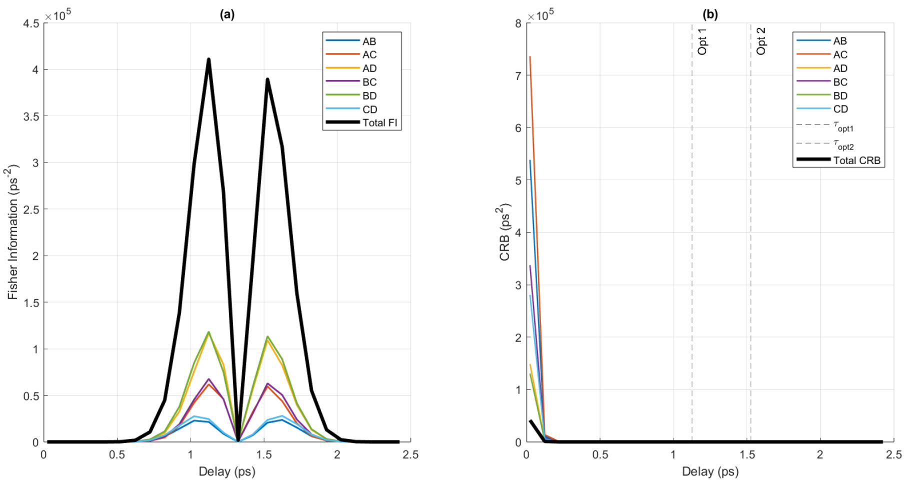

Figure 4.6.2: (a) Fisher information (FI) as a function of the relative delay for all output channel pairs, along with the total FI (black line). The FI peaks at the points of maximum slope of the HOM interference features, indicating optimal sensitivity for delay estimation. (b) Corresponding Cramér–Rao bound (CRB) as a function of delay for each channel pair and for the total FI. The minimum of the CRB identifies the optimal operating points for precision measurements.

Table 4.6.1: Measured Gaussian fit parameters of HOM interference for all six output channel pairs, for inputs 3–4 in the $L = 12.7\,\mathrm{m}$ fiber. Uncertainties are statistical fit uncertainties σ_{fit} only; the delay-stage positioning uncertainty σ_{cal} is not included here (see text).

Channel	Type	Visibility	d (ps)	σ_τ (ps)
AB	peak	0.823 ± 0.018	0.262 ± 0.007	0.247 ± 0.006
AC	dip	0.947 ± 0.023	0.261 ± 0.007	0.247 ± 0.007
AD	dip	0.968 ± 0.019	0.267 ± 0.006	0.252 ± 0.006
BC	dip	0.903 ± 0.017	0.265 ± 0.006	0.251 ± 0.006
BD	dip	0.900 ± 0.018	0.266 ± 0.006	0.251 ± 0.006
CD	peak	0.998 ± 0.021	0.264 ± 0.007	0.250 ± 0.006
Mean		0.92 ± 0.06	0.264 ± 0.001	0.250 ± 0.002

the sensitivity to temporal variations is maximized. Conversely, the Cramér–Rao bound, being inversely proportional to the FI, reaches its minimum at these same operating points, indicating the highest achievable precision in delay estimation. The combined contribution of all output channels significantly enhances the total FI, leading to a substantial reduction of the global CRB compared to individual channels. This demonstrates the advantage of multi-channel detection in optimizing measurement sensitivity and approaching the fundamental precision limits.

The FI computed directly from the experimental count data scales with the total number of detected events; therefore, it is normalized by the total counts to allow comparison with theoretical predictions. This yields an effective Fisher information per event of $F = 0.66 \pm 0.05$ ps^{-2}, which is consistent with the expected $1/\sigma_\tau^2$ scaling for a coherence time of 0.25 ps, accounting for the reduction due to non-unit visibility. This agreement indicates that the measurement operates close to the coherence-limited regime. Correspondingly, the Cramér–Rao bound sets a minimum achievable uncertainty of $\Delta\tau_{\mathrm{CRB}} \approx 1/\sqrt{F} \sim 1.2$ ps per event.

To illustrate the effect of ICS on two-photon interference, we present in Fig. 4.6.3 the full set of HOM measurements obtained for all 12 input channel pairs at a fixed fiber length of L=7.71m. While high-visibility interference is observed in all cases, the temporal position of the HOM dip varies systematically between different channel combinations. This shift directly reflects differential group delays induced by ICS, which accumulate over the fiber length and lead to relative temporal mismatches at the beamsplitter.

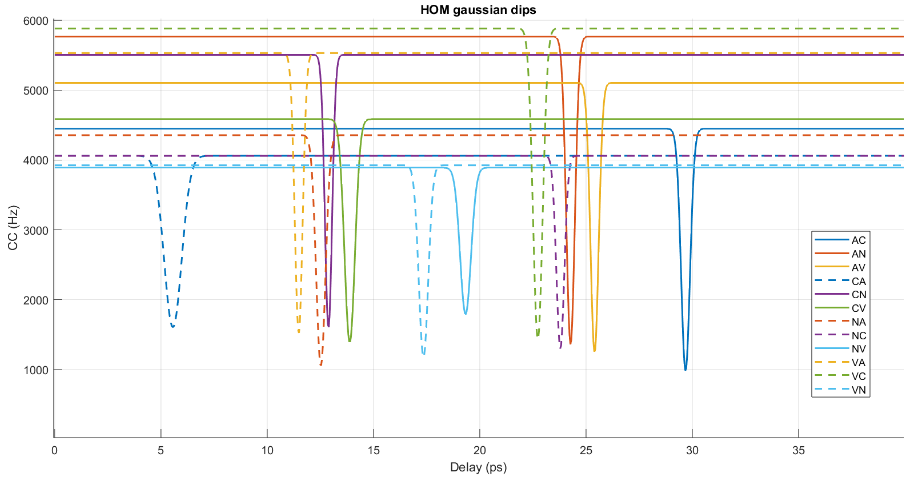

Figure 4.6.3: HOM interference measurements for all 12 input channel pairs at a fixed fiber length of L=7.71m. Each curve shows the total coincidence counts as a function of relative temporal delay. The displacement of the dip centers across different channel combinations reveals the effect of ICS, which introduces relative arrival-time offsets between photons propagating through distinct cores.

The fit data is shown in Table 4.6.1. The visibilities range from 82% to near 100%, with a mean of $\bar{V} = 92 \pm 6\%$ after accidental subtraction, close to the ideal $|V| = 1$ expected for a Fock-state input. Deviations from ideal arise from residual photon distinguishability, fan-in/fan-out asymmetries, and imperfect beam-splitter split ratios. The mean coherence time $\sigma_\tau = 0.250 \pm 0.002\,\mathrm{ps}$ confirms the expected value from the 30 nm spectral filter. Gaussian fits of all six output channels yield consistent dip-center positions ($\bar{d} = 0.264 \pm 0.001\,\mathrm{ps}$), as expected since the dip position depends only on the input core pair (Table 4.6.1).

We now quantify the uncertainty on these extracted values. The $\pm 0.002\,\mathrm{ps}$ fit precision σ_{fit} is the purely statistical uncertainty from averaging over six output channels. The dominant contribution to the dip-position uncertainty is the delay-stage positioning uncertainty $\sigma_{\mathrm{cal}} = 0.15\,\mathrm{ps}$, taken as a conservative upper bound from the manufacturer-specified delay stability of the General Photonics VDL-002 delay line. These two contributions combine as $\sigma_d = (\sigma_{\mathrm{fit}}^2 + \sigma_{\mathrm{cal}}^2)^{1/2} \approx 0.15\,\mathrm{ps}$ for each dip position, as listed in Table 4.6.2. Since the ICS is extracted via the half-difference of two independent readings (Eq. 4.2.7), the propagated uncertainty on each τ_{jk} is $\sigma_{\tau_{jk}} = \sigma_d/\sqrt{2} \approx 0.11\,\mathrm{ps}$. The demonstrated precision of $\pm 0.11\,\mathrm{ps}$ is thus a consequence of the delay stage rather than photon statistics, and could be substantially improved toward the femtosecond CRB with interferometrically calibrated delay control.

Table 4.6.2: Extracted HOM dip positions d_{ij} for all 12 ordered input channel pairs of the MCF at $L = 12.7\,\mathrm{m}$ and $L = 49.7\,\mathrm{m}$. Uncertainties reflect $\sigma_d = (\sigma_{\mathrm{fit}}^2 + \sigma_{\mathrm{cal}}^2)^{1/2} \approx 0.15\,\mathrm{ps}$, dominated by the delay-stage positioning uncertainty. The ICS for each unordered pair is obtained as $\tau_{ij} = |d_{ij} - d_{ji}|/2$.

Input pair	d_{ij} (ps), $L = 12.7\,\mathrm{m}$	d_{ij} (ps), $L = 49.7\,\mathrm{m}$
1–2	13.73 ± 0.15	31.57 ± 0.15
1–3	16.22 ± 0.15	12.67 ± 0.15
1–4	23.88 ± 0.15	6.62 ± 0.15
2–1	23.98 ± 0.15	7.31 ± 0.15
2–3	21.40 ± 0.15	32.67 ± 0.15
2–4	29.06 ± 0.15	60.51 ± 0.15
3–1	21.62 ± 0.15	27.42 ± 0.15
3–2	16.49 ± 0.15	38.63 ± 0.15
3–4	26.53 ± 0.15	17.15 ± 0.15
4–1	14.15 ± 0.15	31.07 ± 0.15
4–2	8.88 ± 0.15	41.51 ± 0.15
4–3	11.30 ± 0.15	22.64 ± 0.15

The extracted dip positions d_{ij} for all 12 input combinations for fibers with $L = 12.7\,\mathrm{m}$ and $L = 49.7\,\mathrm{m}$ are listed in Table 4.6.2. Each pair is measured in both input orderings; the half-difference (Eq. 4.2.7) yields the ICS τ_{jk}, given in Table 4.6.3, along with propagated uncertainties and RMS values. The RMS ICS increases from $12.20 \pm 0.045\,\mathrm{ps}$ at 12.7 m to $17.47 \pm 0.045\,\mathrm{ps}$ at 49.7 m, reflecting the cumulative accumulation of inter-core skew with propagation length.

Table 4.6.3: Inter-core skew (ICS) magnitudes $\tau_{ij} = |d_{ij} - d_{ji}|/2$ for each unordered core pair at $L = 12.7\,\mathrm{m}$ and $L = 49.7\,\mathrm{m}$. Individual ICS uncertainties $\sigma_{\tau_{jk}} = \sigma_d/\sqrt{2} \approx 0.11\,\mathrm{ps}$; RMS uncertainty $\sigma_{\mathrm{RMS}} = \sigma_{\tau_{jk}}/\sqrt{6} \approx 0.045\,\mathrm{ps}$.

Pair i-j	$\lvert\tau_{ij}\rvert$ (ps), $L = 12.7\,\mathrm{m}$	$\lvert\tau_{ij}\rvert$ (ps), $L = 49.7\,\mathrm{m}$
1–2	10.25 ± 0.11	24.26 ± 0.11
1–3	5.41 ± 0.11	14.75 ± 0.11
1–4	9.73 ± 0.11	24.45 ± 0.11
2–3	4.91 ± 0.11	5.97 ± 0.11
2–4	20.18 ± 0.11	18.99 ± 0.11
3–4	15.24 ± 0.11	5.49 ± 0.11
RMS	12.20 ± 0.045	17.47 ± 0.045

4.6.2 Random-walk scaling of ICS with fiber length

Figure 4.6.4 shows the RMS ICS $\sigma_\tau(L)$ as a function of $\sqrt{L}$ for fiber lengths $L = 7.7, 12.7, 49.7, 72.7, 114.7, 187.7$ m measured with SPDC (regime A, Section 4.5.2). At longer lengths, some core-pair combinations no longer exhibit HOM features within the original delay scan range (≈ 100 ps): 10 of 12 input pairs were observable at $L = 72.7$ m, 7 at $L = 114.7$ m, and only 1 on an installed $L = 187.7$ m fiber (not shown). This is a direct consequence of ICS exceeding the TPI delay-line range and is consistent with the $\kappa\sqrt{L}$ scaling. To access these longer lengths it was necessary to extend the free-space delay line, adding approximately -6 dB of coupling loss per photon and providing a further practical motivation for the pulsed-laser approach, which was used to test a field-deployed $L \approx 1300$ m fiber (red data point). The shortest point at $L = 7.7$ m corresponds to the MCF fiber contained within the MUX fan-in and MCF-BS devices. The data follow the Eq. (4.2.5), confirming the stochastic random-walk model. A weighted linear fit gives

$$\kappa = 1.54 \pm 0.08 \text{ ps}/\sqrt{\text{m}} = 48.7 \pm 2.5 \text{ ps}/\sqrt{\text{km}}, \qquad c = 9.76 \pm 1.2 \text{ ps}.$$

The value $\kappa = 48.7\,\text{ps}/\sqrt{\text{km}}$ is > 50 larger than typical PMD coefficients for single-mode fiber (0.1–1 $\text{ps}/\sqrt{\text{km}}$), confirming that the measured effect is genuine inter-core differential group delay rather than a polarization-related artifact. Expressed as a skew per unit length, $\kappa = 48.7 \pm 2.5\,\text{ps}/\sqrt{\text{km}}$ corresponds to 0.049 ± 0.003 ns/km at $L = 1$ km, consistent with reported ICS values of 0.06–0.2 ns/km for other four-core and seven-core fiber designs [178, 166]. The length-independent intercept $c = 9.76$ ps is attributed to step-function ICS offsets at each butt-coupled MCF connector junction, where independently manufactured fiber sections present a fixed, random differential group-index mismatch.

While $\sqrt{L}$ scaling is expected for purely stochastic accumulation, finite sample size or correlated perturbations may lead to deviations. To account for this, we also fit a general power-law model $\sigma_\tau(L) = A\,L^\alpha$, which reduces to the stochastic case for $\alpha = 0.5$ and to deterministic linear scaling for $\alpha = 1$. The exponent α is estimated via weighted least-squares regression in log–log space, with weights defined from propagated uncertainties, $\sigma_{y,i} = \sigma_{\text{ICS},i}/(\text{ICS}_i \ln 10)$, and additional down-weighting applied to length points with fewer accessible core-pair combinations.

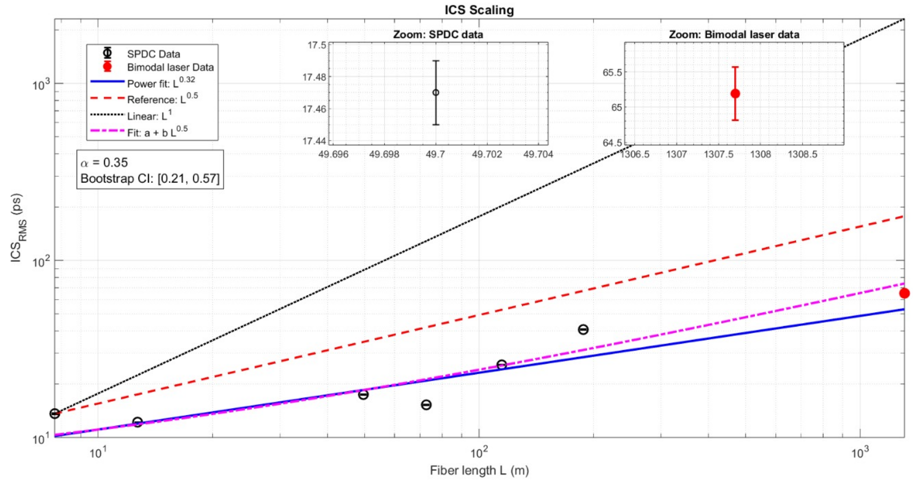

Figure 4.6.4: Scaling of the $\mathrm{ICS}_{\mathrm{RMS}}$ as a function of fiber length L in log-log scale for all measured lengths L. Experimental measurements (markers with error bars) are fitted using Eq. (4.2.5) (dot-dashed pink line) and a weighted power-law model ICS $\propto L^{\alpha}$ (solid blue line). The shaded region represents the propagated uncertainty of the fit in log space. Reference scalings $L^{0.5}$ (dashed red) and L^{1} (dotted black) are shown for comparison. A bootstrap resampling analysis ($N = 5000$) yields a 95% confidence interval for $\alpha = 0.35$ with a 95% CI [0.21,0.57].The point estimate α is biased below 0.5 by the physical offset c in the underlying model (see text). Data at 1300 m were obtained using the bimodal pulsed laser source (regime B; Section 4.5.2).

This procedure yields a point estimate $\alpha = 0.32$, which should be interpreted with care: the power-law model $A\,L^{\alpha}$ contains no intercept, so when the true behavior includes a physical offset $c \neq 0$ (as in this case), the exponent is biased toward lower values. This explains why the constrained $\sqrt{L} + c$ model provides a visually superior fit despite having the same number of free parameters. The data are nevertheless well described by both models, with the power-law fit yielding a higher goodness of fit ($R^2 \approx 0.97$) compared to the $\sqrt{L} + c$ model ($R^2 \approx 0.93$).

To assess robustness, we perform a non-parametric bootstrap analysis ($N = 5000$ resampled datasets), obtaining $\alpha = 0.35$ with a 95% confidence interval $[0.21, 0.57]$ (percentile method), which includes the theoretical value $\alpha = 0.5$. Therefore, the null hypothesis of standard $\sqrt{L}$ scaling cannot be rejected at the 95% confidence level.

4.6.3 Comparison with classical ICS measurement methods

Table 4.6.4 contextualizes our results within the existing literature on ICS characterization. The key comparison is in precision: C-OTDR achieves $\lesssim 20$ ps resolution after Gaussian fitting of the correlation peak [166], while our HOM method achieves ± 0.11 ps from dip-center fitting, a factor of ~ 180 improvement in demonstrated precision. The fundamental CRB for the measurements reported here (per-channel values of 0.93–1.94 fs; Section 4.4) is more than four orders of magnitude below the demonstrated precision, indicating that substantially greater precision is in principle achievable with an improved delay calibration.

Table 4.6.4: Comparison of ICS characterization methods. Skew column definitions vary by method. C-OTDR and cross-correlation entries give an average or maximum $|\tau_{jk}|/L$ per core pair. The HOM/SPDC entry gives the random-walk coefficient κ (units ps/$\sqrt{\text{km}}$) from fitting the RMS over all six unordered pairs. The HOM/laser entry gives the mean $|\tau_{jk}|/L$ averaged over all six unordered pairs (see note ^{e}). Direct numerical comparison across rows is therefore qualitative. Precision: demonstrated single-measurement resolution for each method. C-OTDR: correlation OTDR. WLI: white-light interferometry.

Method	Cores	L	Skew	Precision	Ref.
C-OTDR	7	10 km	0.18 ns/km	$\lesssim 20$ ps	[166]
C-OTDR	7	1 km	1.2 ns/km	$\lesssim 20$ ps	[166]
C-OTDR	19	5 km	0.66 ns/km	$\lesssim 20$ ps	[166]
C-OTDR	19	25 km	1.2 ns/km	$\lesssim 20$ ps	[166]
MPS^a	19	5 km	± 300 ps (drift)	$\sim$ns	[166]
WLI	4	short	—^{b}	sub-ps	[168]
WLI+splice^b	4	—	—^{b}	sub-ps	[165]
Cross-corr.^{c}	7	53.7 km	$\lesssim 0.5$ ns/km	sub-ps	[12]
Temp. OTDR	19	—	± 60 ps/40 K	$\sim$ps	[179]
HOM/SPDC	**4**	**7.7–187.7 m**	$\boldsymbol{\kappa = 48.7 \pm 2.5}$ ps/$\sqrt{\text{km}}$	**±0.11** ps; CRB $\sim$fs	**here**
HOM/laser^e	**4**	**1.3 km**	**0.049 ns/km** (mean)	**0.70 ps**	**here**

^{a}MPS: modulation phase shift. Only one core can be measured at a time, so consecutive measurements are separated by thermal drift of several hundred ps, preventing reliable differential skew characterisation.
^{b}WLI references characterize skew at fixed lengths or demonstrate stochastic accumulation qualitatively; neither κ nor absolute skew magnitudes were reported.
^{c}Cross-correlation of 10 Gb/s OOK waveforms [12]. Skew entry is the maximum observed $|\tau_{jk}|/L$ (between the most disparate core pair); the mean over cores relative to the centre core is ~ 100 ps/km for homogeneous MCFs. Precision applies to dynamic skew tracking; static absolute delays are determined to ns-level accuracy.
^{d}Rotated-splice compensation fails, confirming that ICS accumulation is stochastic [165].
^{e}HOM/laser skew is the mean $|\tau_{jk}|/L$ averaged over all six unordered core pairs at $L = 1300$ m, the metric most directly comparable to literature average-skew figures.
Fiber: Fibercore SM-4C1500(8.0/125)/001 for this work.

Summary

We have demonstrated sub-picosecond measurement of inter-core skew (differential group delay) in a commercially available four-core multicore fiber (Fibercore SM-4C1500) using Hong–Ou–Mandel two-photon interference in a fiber-integrated 4×4 multiport beam splitter. ICS is extracted from HOM dip and peak center positions across all twelve input core-pair combinations, with a demonstrated precision of ± 0.11 ps per measurement, limited by the delay-stage positioning uncertainty, and a fundamental Cramér–Rao bound in the femtosecond range that could be approached with improved delay control.

The RMS ICS grows as $\sigma_\tau(L) = (48.7 \pm 2.5\,\mathrm{ps}/\sqrt{\mathrm{km}})\sqrt{L} + (9.76 \pm 1.2)\,\mathrm{ps}$ over lengths from 7.7 m to 187.7 m, providing the first direct validation of the stochastic random-walk scaling of ICS in a four-core fiber across a length range inaccessible to classical methods. Extension of the scaling curve to $L = 1300$ m using the bimodal pulsed laser source is consistent with the $\sqrt{L}$ model, though a generalised power-law fit cannot conclusively rule out sub-diffusive scaling with the current dataset.

For classical SDM transmission, the demonstrated precision far exceeds digital signal processing buffer requirements, enabling per-span ICS monitoring compatible with deployed telecom infrastructure at 1550 nm. For quantum networks, the ability to characterize ICS with sub-picosecond resolution enables compensation of timing mismatch before it degrades photon interference in MCF-based links, and the complementary pulsed-laser regime extends this capability to field-deployed fibers with high channel loss. The Fisher information framework established here provides a systematic basis for optimizing photon bandwidth, scan parameters, and delay calibration to approach the CRB in future experiments.

Chapter 5

Experimental Pathways to Device-Independent Quantum Key Distribution

Author Contribution Statement

This chapter is partially based on the review article by Ghoreishi et al. (Physics Reports, 2025) [23]. The author of this thesis contributed directly to the development of that work, and the specific contributions are outlined below.

The author was involved in the bibliographic review of experimental implementations of Device-Independent Quantum Key Distribution (DIQKD) and Measurement-Device-Independent QKD (MDI-QKD), including the organization of results and the construction of a timeline of key developments.

The author also contributed to the introductory sections on DIQKD, including text development, as well as the design of figures and graphical elements, and participated in the discussion of experimental limitations of DIQKD protocols.

In addition, the author contributed to the section on entanglement sources, particularly those based on Spontaneous Parametric Down-Conversion (SPDC), reflecting their research expertise in this area.

Finally, the author participated in the literature review on scalable quantum networks, helping to contextualize future research directions.

5.1 Introduction and Conceptual Roadmap

Device-independent quantum key distribution (DI–QKD) represents the most stringent form of quantum cryptography: the secrecy of the generated key is certified directly from observed measurement statistics, without requiring a detailed and trusted model of the internal functioning of the devices used in the protocol [180, 181]. Security is instead inferred from the violation of a Bell inequality [182, 183], which certifies the presence of nonlocal quantum correlations and bounds the potential information available to an adversary.

The objective of this chapter is to bridge the abstract theoretical framework of DI–QKD with its experimental realization [184]. We begin with a concise overview of standard quantum key distribution protocols [185, 186] and motivate the transition toward device independence [180]. We then introduce the minimal theoretical framework underlying DI–QKD, including Bell inequalities [182, 183] and entropy accumulation [181].

Subsequently, we analyze the experimental constraints and architectures required for loophole-free implementations [187], with particular emphasis on event-ready schemes and entanglement swapping [188], linear-optical Bell-state measurements, and Hong–Ou–Mandel (HOM) interference as an operational resource [7]. Finally, we review recent experimental demonstrations and discuss the challenges toward scalable implementations [184, 189, 190].

5.2 Conventional QKD and Its Practical Limitations

Quantum key distribution (QKD) enables two distant parties, conventionally named Alice and Bob, to establish a shared secret key whose security is guaranteed by fundamental principles of quantum mechanics [191]. Unlike classical key agreement protocols, whose security relies on computational assumptions, QKD can provide information-theoretic security against an adversary with unbounded computational power. The central idea is that any eavesdropping attempt necessarily disturbs the quantum states exchanged between the legitimate users, leaving detectable traces in the observed statistics.

QKD protocols can be broadly classified into two main categories: *prepare-and-measure* protocols and *entanglement-based* protocols. While these approaches are conceptually distinct, they are closely related at a theoretical level and can often be shown to be equivalent under suitable assumptions, as formalized in security proofs such as that of Shor and Preskill [192].

5.2.1 Prepare-and-Measure Protocols

In prepare-and-measure (P&M) QKD, Alice prepares quantum states according to a prescribed ensemble and sends them to Bob through a quantum channel, who measures them using randomly chosen measurement. The prototypical example is the BB84 protocol, originally proposed by Bennett and Brassard [185], in which Alice encodes classical bits into non-orthogonal quantum states drawn from two mutually unbiased bases. Bob measures each incoming state in one of these bases, and after the quantum transmission, Alice and Bob publicly compare their basis choices and retain only the events where they match (see Fig. 5.2.1).

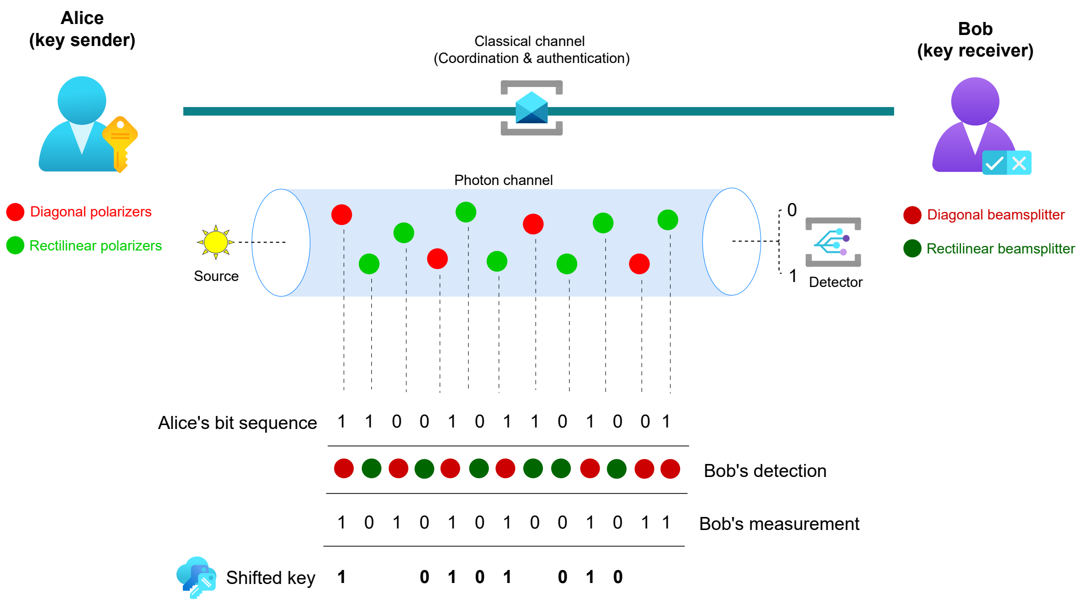

Figure 5.2.1: *Quantum Key Distribution*: Alice transmits photons to Bob through a quantum channel with the raw key material and both use a classical channel for coordination and authentication. A subset of measurement results is publicly compared to detect eavesdropping through the observed error rate. If the error rate is below a predefined threshold, the remaining data forms the sifted key. Error correction and privacy amplification are then applied to remove discrepancies and eliminate any partial information an adversary may have gained, yielding a shared secret key ready for encryption.

The security of P&M protocols relies on the impossibility of perfectly discriminating non-orthogonal quantum states. Any eavesdropping attempt introduces errors that can be detected by estimating the quantum bit error rate (QBER). Subsequent classical post-processing steps (error correction and privacy amplification) are used to distill a shorter but secure secret key.

5.2.2 Entanglement-Based Protocols

Entanglement-based QKD protocols reformulate the key distribution in terms of shared quantum correlations. In the seminal E91 protocol proposed by Ekert [186], Alice and Bob receive entangled particle pairs from a source and perform measurements on randomly chosen bases. The correlations between their outcomes are used both to generate a secret key and to test for the presence of an eavesdropper, typically through the violation of a Bell inequality (BI).

From a conceptual standpoint, entanglement-based protocols emphasize the role of nonlocal quantum correlations as a resource enabling secure key distribution. They provide a natural framework for security proofs and form the basis for more advanced schemes such as device-independent QKD, where security is inferred directly from observed Bell violations rather than detailed device models. Table 5.2.1 summarizes the main conceptual differences between P&M and entanglement-based QKD protocols.

Table 5.2.1: Comparison between prepare-and-measure and entanglement-based QKD protocols.

Feature	**P&M**	**Entanglement-Based**
Quantum resource	Single quantum states prepared by Alice	Entangled quantum states shared by Alice and Bob
Conceptual picture	State preparation and measurement	Measurement of shared correlations
Security principle	Disturbance of non-orthogonal states	Monogamy of entanglement and nonlocal correlations
Eavesdropping detection	QBER	Error rates and BI violation
Source location	At Alice's station	Between Alice and Bob (possibly untrusted)
Relation to DI-QKD	Indirect; requires device assumptions	Natural starting point for DI-QKD
Practical maturity	Widely deployed in commercial systems	Increasingly mature; central for advanced protocols

Although P&M protocols are currently the most widely implemented due to their relative simplicity, entanglement-based schemes offer deeper insight into the fundamental origins of QKD security and provide the conceptual and experimental foundation for device-independent approaches. In the following sections, these ideas will be extended to scenarios where progressively fewer assumptions about the quantum devices are required.

5.2.3 Limitations of Standard QKD and Motivation for Device Independence

In its standard formulation, the security of QKD protocols relies on explicit assumptions about the internal functioning of the quantum devices employed in the protocol [193]. These assumptions typically include accurate models of state preparation, measurement operators, and detector behavior. While such assumptions are well justified in idealized theoretical descriptions, they become a significant source of vulnerability in practical implementations.

A series of experimental attacks exploiting imperfections in realistic QKD devices has demonstrated that deviations from idealized device models can be leveraged to compromise security without contradicting the underlying theoretical framework of standard QKD protocols. Examples include detector blinding attacks [194], time-shift attacks [195], and side-channel vulnerabilities [196], which collectively highlight that implementation security can be as critical as protocol security. As a consequence, closing the gap between theoretical security proofs and their physical realizations has emerged as a central challenge in quantum cryptography, motivating the development of approaches that reduce or eliminate trust in device models.

DI–QKD addresses this challenge by radically reducing the trust placed in the devices themselves. In DI–QKD, security is derived solely from the observation of nonlocal correlations that violate a Bell inequality, together with the validity of quantum mechanics and the assumption of no unwanted information leakage from the laboratories. Importantly, the internal workings of the state sources and measurement devices need not be characterized or trusted, as long as the observed statistics are consistent with a loophole-free Bell violation.

This conceptual shift has profound experimental consequences. Unlike standard QKD, where losses and inefficiencies can often be accommodated through post-selection or fair-sampling assumptions, DI–QKD strictly forbids such practices. Any post-selection based on detection events would open the detection loophole, allowing classical correlations to mimic quantum nonlocality. Consequently, DI–

QKD requires experiments capable of generating and measuring entanglement with sufficiently high efficiency to close all relevant loopholes in a Bell test.

In photonic platforms, these requirements represent a particularly stringent constraint. Photons are naturally well suited for long-distance quantum communication, but their generation and detection are inherently probabilistic, leading to significant losses. Overcoming these limitations requires experimental architectures that go beyond direct entanglement distribution and instead rely on heralded or event-ready schemes, in which successful trials are identified independently of the measurement outcomes used to generate the key.

Therefore, DI–QKD is not merely a more conservative security framework layered on top of existing QKD implementations. Rather, it constitutes a fundamentally different experimental paradigm, where the design and characterization of the physical platform, especially with respect to entanglement generation, detection efficiency, and loophole-free Bell tests, are integral to the security of the protocol itself. This perspective motivates the detailed examination of experimental DI–QKD architectures presented in the following sections.

5.2.4 Measurement-Device-Independent Quantum Key Distribution

Measurement-Device-Independent Quantum Key Distribution (MDI-QKD) was introduced to eliminate all security loopholes associated with the detection stage, which historically has been the most vulnerable component of practical QKD implementations [197, 198]. While standard prepare-and-measure protocols such as BB84 rely on trusted measurement devices at the receiver's station [185], numerous side-channel attacks, most notably detector blinding attacks, have demonstrated that realistic detectors can be externally controlled without revealing discrepancies in the observed statistics [199]. MDI-QKD removes this vulnerability by shifting the measurement to an untrusted relay and proving security independently of the internal functioning of the detection apparatus [197].

The conceptual foundation of MDI-QKD is time-reversed entanglement-based QKD [197]. Instead of distributing entangled photon pairs from a central source to two distant parties, Alice and Bob independently prepare quantum states and send them to a central node, commonly referred to as Charlie (see Fig. 5.2.2).

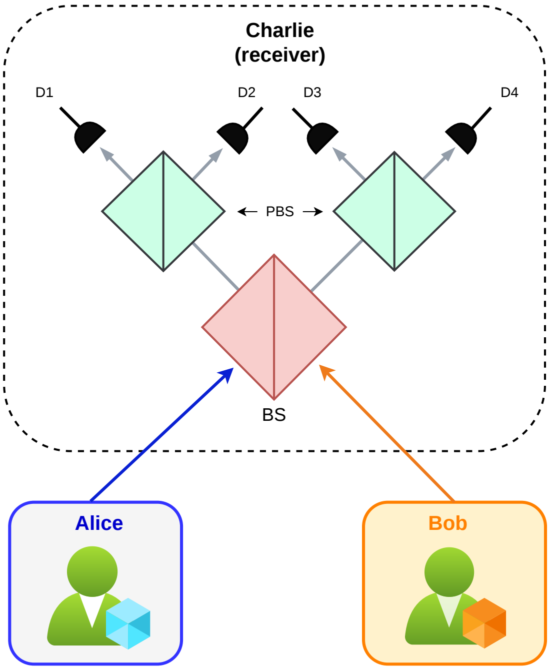

Figure 5.2.2: Typical MDI-QKD setup. Alice and Bob send out polarization encoded weak coherent pulses to Charlie, who is supposed to perform partial BSMs with a beam splitter (BS), polarizing beam splitters (PBS), and single photon detectors.

Charlie performs a Bell-state measurement on the incoming signals and publicly announces the measurement outcome. Crucially, Charlie is not required to be trusted; the security proof treats the measurement device as a black box potentially controlled by an adversary [197, 198]. Security is guaranteed as long as Alice's and Bob's state preparation devices are well characterized and trusted [198]. To clarify the hierarchy of trust assumptions across the main QKD paradigms, Table 5.2.2 summarizes the operational security models.

Table 5.2.2: Comparison of assumptions in different QKD protocols.

Protocol	**Trust Assumptions**
BB84	Trusted source and trusted detectors
MDI-QKD	Trusted sources; measurement devices untrusted
DI-QKD	No trust in source or measurement devices

As we can see, MDI-QKD occupies an intermediate position between conventional prepare-and-measure protocols and fully device-independent schemes [198].

In a typical implementation, Alice and Bob randomly prepare phase-randomized weak coherent pulses in complementary bases (e.g., Z and X bases in a BB84-type encoding) and vary the mean photon number using the decoy-state method [200, 201]. The decoy-state technique enables estimation of the single-photon contributions to the key rate, which is essential because weak coherent pulses contain multi-photon components that could otherwise be exploited by photon-number-splitting attacks [200, 201]. Upon interference at Charlie's station, coincident detection events corresponding to successful Bell-state projections post-select entangled correlations between Alice and Bob, even though no entangled source was directly distributed [197].

Let $Q_{\mu\nu}$ denote the gain when Alice and Bob use intensities μ and ν, respectively, and let $E_{\mu\nu}$ be the corresponding QBER. By applying decoy-state analysis, one can bound the yield Y_{11} and phase error rate e_{11}^{ph} of the single-photon pair contributions [197, 201]. The asymptotic secret key rate per pulse is then lower bounded by

$$R \geq S_{11}\left[1 - h\left(e_{11}^{\mathrm{ph}}\right)\right] - Q_{\mu\mu} f_{\mathrm{EC}} h\left(E_{\mu\mu}\right), \tag{5.2.1}$$

where S_{11} is the gain of single-photon pairs, $h(x)$ is the binary entropy function, and f_{EC} quantifies the inefficiency of classical error correction. This expression highlights that only the single-photon interference events contribute positively to the secure key, while overall observed errors determine the classical leakage during reconciliation [197].

Experimentally, MDI-QKD requires high-visibility two-photon interference between independent laser sources [198]. This imposes stringent constraints on spectral indistinguishability, temporal synchronization, polarization alignment, and phase stability. The central physical mechanism enabling security is Hong–Ou–Mandel interference [7]: when two indistinguishable photons impinge on a 50:50 beam splitter, they bunch, leading to correlated detection events that herald Bell-state projections. Imperfect indistinguishability directly reduces interference visibility, thereby increasing the QBER and reducing the achievable key rate [198].

One of the most significant advantages of MDI-QKD is its natural suitability for star-type quantum networks [198, 202]. Since the central measurement node can be untrusted, multiple users can connect to a common relay without compromising security. This architecture substantially lowers the security requirements for intermediate infrastructure, making MDI-QKD particularly attractive for metropolitan-scale quantum communication networks. However, compared to conventional QKD, the secret key rate typically scales less favorably with channel loss because successful events require simultaneous detection of photons from both users, leading to a quadratic dependence on transmission efficiency [203].

From a conceptual standpoint, MDI-QKD represents an intermediate step between standard QKD and fully Device-Independent QKD [198]. While it removes all detector side-channel vulnerabilities, it still assumes trusted and well-characterized state preparation devices. In contrast, DI-QKD aims to certify security solely from Bell inequality violations without trusting either preparation or measurement devices [180]. Nonetheless, MDI-QKD currently offers a practical and experimentally mature pathway toward side-channel-resistant quantum communication with rigorous composable security proofs [198].

5.3 Framework of Device-Independent QKD

5.3.1 Black-Box Model and the evolution of DI-QKD

The internal workings and security of the quantum devices involved in QKD protocols are often faulty and vulnerable to quantum hacking. DI-QKD provides cryptographic security without relying on any characterization of the internal functioning of the quantum devices used by legitimate parties. Instead, security is achieved through non-local correlations verified by BI violation, as shown in Fig. 5.3.1.

We consider two distant parties, Alice and Bob, who interact with uncharacterized devices modeled as black boxes. In each round i, Alice (Bob) chooses a classical input $x_i \in \mathcal{X}$ ($y_i \in \mathcal{Y}$) and obtains a classical output $a_i \in \mathcal{A}$ ($b_i \in \mathcal{B}$). The behavior of the devices is fully described by the conditional probability distribution

$$p(ab|xy), \tag{5.3.1}$$

which is estimated from experimental data. In general, the correlations, or *behaviors* are indicated as points $p = \{p(ab|xy)\}_{a,b,x,y}$ in the convex correlation space characterized by the regions $\mathcal{L} \subset \mathcal{Q} \subset \mathcal{NS}$ respectively for local and realistic, quantum, and no-signaling behaviors, respectively. A BI violation

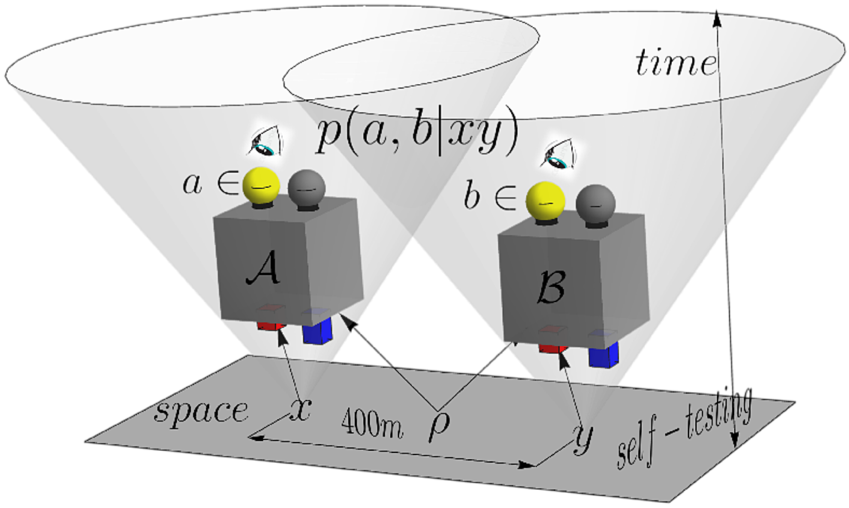

Non-local Bell-test

Figure 5.3.1: *DI-QKD and Bell's Theorem* — only by the observed correlations p from two causal cones, the security of DI-QKD is tested by BI determining if $p \notin \mathcal{L}$ (see Ref. [23], Chapter 2). Self-testing may also be possible, a time retroactive process that infers the inputs x, y, ρ from p [204].

($p \notin \mathcal{L}$), classified as "strongly non-classical" [205], implies one of two possibilities, or both: (*1*) a and b are determined only when observed; (*2*) a non-local influence ensures that the key is established solely through interactions between trusted parties. In either case, Eve cannot access the information without being detected because any interference would deviate from the expected non-local correlations.

The minimal assumptions underlying DI–QKD are:

1. *Quantum realizability*: the observed correlations admit a quantum mechanical realization.

2. *No-signalling within a round*: Alice's (Bob's) output is independent of Bob's (Alice's) input.

3. *Measurement independence*: the inputs (x, y) are chosen independently of the devices and any adversary.

4. *Authenticated classical communication*: public communication channels are authenticated but not necessarily secret.

No assumptions are made regarding the Hilbert space dimension, state preparation, measurement operators, or detector efficiencies.

Fig. 5.3.2 shows the evolution of DI-QKD, from the BB84 and E91 protocol [186] up to the formalization of theoretical techniques and the first implementations in 2022 [206, 207, 208] (details in Fig. 5.3.3).

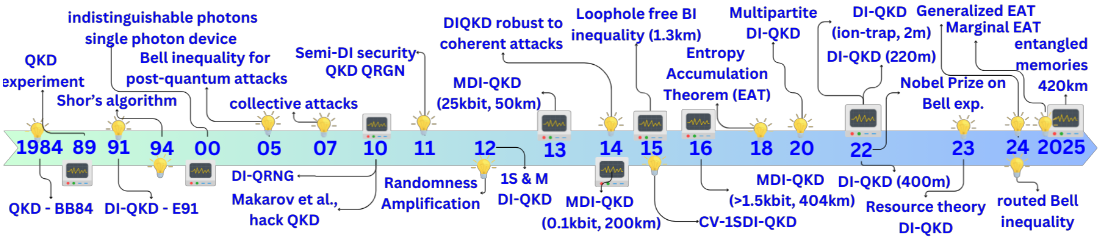

Figure 5.3.2: Timeline highlighting key events using a lamp and oscilloscope, distinguishes theoretical and experimental contributions (MDI - measurement device independent; 1S – One-sided; QRGN – Quantum random generator number; CV- continuous variable).

Remarkably, the first successful implementation of DI-QKD was reached after overcoming all the Bell test loopholes, highlighting the challenges in realizing DI-QKD and its connection with BI experiments. Fig. 5.3.3 compares the current experimental reach of DI-QKD - specifically, the distances of 2 m, approximately 200 m, and 400 m — with those achieved using MDI-QKD.

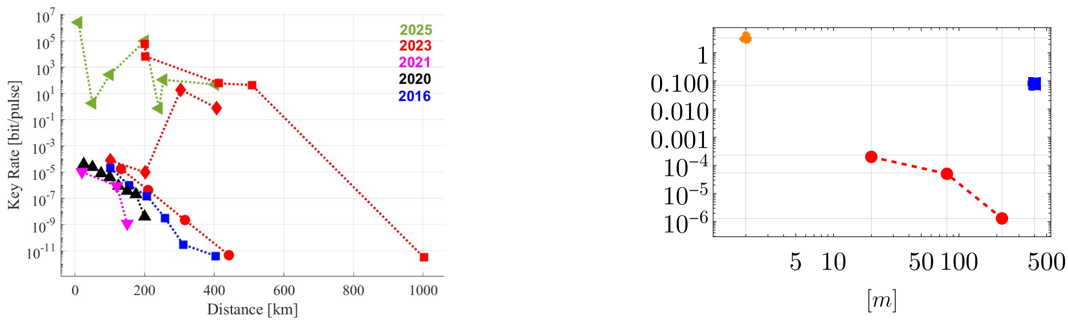

(a) *MDI–QKD* (b) *DI–QKD*

Figure 5.3.3: *Comparative Analysis of DI-QKD and MDI-QKD Experiments* – Fig. 5.3.3a encapsulates the progress in quantum communication distances achieved through MDI-QKD implementations [209, 210, 211, 212, 213, 18, 214, 215, 216, 217]. In contrast fully-DI-QKD in Fig. 5.3.3b at distances: 2 m (yellow)[206], 20 m, 100 m, and 200 m (red)[207], and 400 m (blue)[208].

Despite the challenges that lie ahead in terms of practical implementation and scalability, as the technology readiness level [218] currently stands at 2-3 (concept formulated/experimental proof of concept), with expectations to advance to level 4-5 in the coming years (technology validated in lab/relevant environment), the pursuit of DI-QKD continues to push the boundaries of what is possible for secure communications.

5.3.2 Bell Inequalities and Entropy Certification

5.3.2.1 CHSH Inequality

Bell inequalities provide experimentally testable criteria to distinguish local from nonlocal correlations [182, 219]. Among them, the Clauser–Horne–Shimony–Holt (CHSH) inequality plays a central role in DI–QKD due to its simplicity and robustness [183, 220]. Defining the CHSH parameter

$$S = E(x_0, y_0) + E(x_0, y_1) + E(x_1, y_0) - E(x_1, y_1), \tag{5.3.2}$$

where $E(x, y)$ denotes the correlation function for measurement settings x and y, local hidden-variable theories satisfy $|S| \leq 2$ [183]. Quantum mechanics, however, allows violations up to the Tsirelson bound $|S| \leq 2\sqrt{2}$ [221].

In the context of DI–QKD, the observation of a Bell inequality violation certifies the presence of intrinsically quantum correlations that cannot be reproduced by classical means [180, 220]. Importantly, this certification does not depend on the internal details of the devices, but only on the measured statistics [222].

5.3.2.2 Entropy Accumulation

A defining feature of DI–QKD is the direct link between Bell nonlocality and cryptographic security [180, 220]. A violation of a Bell inequality implies that the measurement outcomes possess intrinsic randomness that is inaccessible to any adversary, including one that may have partial or full control over the devices used by Alice and Bob [220].

Quantitatively, the observed Bell violation can be used to bound the min-entropy of the raw key, which in turn determines the maximum information available to an eavesdropper [220, 223]. Stronger Bell violations correspond to higher certified randomness and larger achievable secret key rates. From an experimental perspective, this establishes a direct connection between measurable quantities, such as the Bell parameter S, and the performance of the DI–QKD protocol [180].

Critically, Bell violation implies a lower bound on the conditional entropy of the outputs given an adversary's quantum side information [220, 222]. For appropriately chosen key-generating inputs, one can bound the per-round conditional min-entropy as

$$H_{\min}(A|E) \geq f(S), \tag{5.3.3}$$

where $f(S)$ is a monotonically increasing function of the Bell violation [220].

In realistic experiments, the devices are used sequentially and may exhibit arbitrary memory effects. Let (A^n, B^n, X^n, Y^n) denote the classical data obtained over n rounds, and let E represent the adversary's quantum system, potentially entangled with the devices.

Security analysis in this non-independent and identically distributed (non-i.i.d.) setting is enabled by the Entropy Accumulation Theorem (EAT) [224, 181]. Under the assumptions stated above, the EAT implies that the smooth min-entropy of the raw key string A^n conditioned on E satisfies

$$H^{\varepsilon}_{\min}(A^n|E) \geq nf(\bar{S}) - O(\sqrt{n}), \tag{5.3.4}$$

where $f(\bar{S})$ is the entropy rate function derived from the Bell inequality, ε is the smoothing parameter, and $O(\sqrt{n})$ accounts for finite-size statistical fluctuations [224]. The theorem therefore guarantees that entropy accumulates approximately linearly with the number of rounds, even without assuming independence between them. This result holds even in the presence of general coherent attacks and device memory, making it directly applicable to experimental implementations [181].

Following entropy estimation, Alice and Bob perform *error correction* and *privacy amplification* [223, 225]. The entropy bound

$$H^{\varepsilon}_{\min}(A^n|E) \geq \kappa \tag{5.3.5}$$

quantifies the amount of extractable randomness in Alice's raw string A^n conditioned on the adversary's quantum side information E.

Since Alice and Bob's raw strings are not perfectly correlated due to noise, they first execute an error correction protocol to reconcile their data. The classical communication exchanged during this step leaks information to the adversary, quantified by leak_{EC} [223].

After error correction, privacy amplification is applied using a randomness extractor (typically a two-universal hash function) to compress the reconciled string into a shorter secret key [226, 223]. By the leftover hash lemma, the final key length ℓ must satisfy

$$\ell \leq \kappa - \text{leak}_{\text{EC}} - O(\log(1/\varepsilon)), \tag{5.3.6}$$

in order to ensure that the output key is ε-secure in the universally composable sense, meaning that it is indistinguishable from an ideal uniformly random key and independent of the adversary's information [223, 225].

5.4 Experimental Constraints in DI–QKD

5.4.1 Detection Loophole

A central experimental challenge in DI–QKD is the closure of the *detection loophole*. This loophole arises when measurement devices fail to produce outcomes with sufficiently high probability. If detection events are selectively post-processed or discarded, an adversary could exploit the missing events to simulate nonlocal correlations using purely classical strategies [227, 228].

No Post-Selection. In standard Bell tests, it is common to post-select on coincident detection events, discarding rounds in which one or both detectors fail to click. This procedure implicitly assumes *fair sampling*, namely that the detected subset faithfully represents the entire ensemble [227]. In DI–QKD, however, such an assumption is not permitted [222, 180]. Since the devices are treated as untrusted black boxes, one cannot assume that detection failures occur independently of hidden variables controlled by an adversary. Therefore, every round of the protocol must be accounted for, and non-detection events must be assigned predetermined outcomes. Security proofs require that the observed Bell violation holds without conditioning on successful detection events [180].

Efficiency Thresholds. The necessity of including all rounds imposes strict requirements on the overall detection efficiency. If the efficiency is too low, a local hidden-variable model can reproduce the observed correlations by selectively producing outcomes only when doing so favors a Bell violation [228, 229]. For the CHSH inequality in a symmetric configuration with binary inputs and outputs, the minimum overall detection efficiency required to close the loophole is approximately

$$\eta_{\text{crit}} = \frac{2}{1+\sqrt{2}} \approx 82.8\%. \tag{5.4.1}$$

Below this threshold, no violation can exclude local models without invoking additional assumptions [228]. More generally, the critical efficiency depends on the specific Bell inequality and detection model [229, 219], but high efficiency is always required in DI protocols.

CHSH Efficiency Bounds. To understand this threshold, consider that detection inefficiencies effectively introduce additional outcome events ("no-click" outcomes). If these are deterministically assigned a fixed output value, the effective correlations are diluted by a factor proportional to η^2 in symmetric scenarios [228]. The observed CHSH parameter then scales approximately as

$$S_{\text{obs}} \approx \eta^2 S_{\text{ideal}}, \tag{5.4.2}$$

so that inefficiency reduces the attainable violation. A sufficiently low efficiency can always be exploited by a classical strategy that only produces detection events for favorable input settings [227]. Consequently, DI–QKD requires detection efficiencies exceeding the critical value in order to certify genuine nonlocality.

Why Standard QKD Tolerates Losses but DI Cannot. The strict efficiency requirements of DI–QKD contrast sharply with standard QKD protocols such as BB84 [185]. In prepare-and-measure QKD, photon losses simply reduce the raw key rate; lost signals are discarded without compromising security because the security proof assumes trusted device models and does not rely on Bell violations [230]. As long as the observed quantum bit error rate remains below the security threshold, arbitrarily high channel loss can in principle be tolerated, albeit at the cost of reduced key rates.

In DI–QKD, by contrast, security is certified exclusively through Bell inequality violation [180]. Detection inefficiencies directly weaken the observed correlations and may reopen the possibility of classical explanations. Losses therefore affect not only the rate but also the validity of the security certification itself. For this reason, closing the detection loophole (through high-efficiency detectors, heralded entanglement schemes, or quantum memories) is a fundamental requirement for practical DI–QKD implementations [219].

5.4.2 Locality and Memory Effects

Beyond the detection loophole, DI–QKD must address two additional conceptual challenges: enforcing locality conditions during each round of the protocol and accounting for possible memory effects arising from the sequential use of untrusted devices [220, 181].

Space-like Separation vs. Shielding. In foundational Bell tests, the locality loophole is closed by arranging the measurement events such that they are space-like separated [182, 187]. That is, the choice of measurement setting on one side and the outcome on the other side occur within time intervals that preclude any communication at or below the speed of light. Under this condition, relativistic causality guarantees that the observed correlations cannot arise from sub-luminal signaling between the devices [219].

In DI–QKD, strict space-like separation is sufficient but not always necessary [222]. Security proofs typically assume that, during each round, no unwanted communication occurs between Alice's and Bob's measurement devices [180, 181]. This condition can be enforced either physically, by ensuring relativistic separation, or operationally, by isolating the devices within well-shielded laboratories that prevent information leakage [222]. The essential requirement is that the input choice on one side cannot influence the output on the other side within the same round, except through pre-established correlations.

In long-distance photonic implementations, space-like separation is naturally achievable due to the propagation delay in optical fibers [187]. In contrast, memory-based or short-distance platforms may rely instead on electromagnetic shielding and carefully engineered timing constraints to enforce effective isolation [222]. From a cryptographic perspective, the assumption is that the laboratories do not leak information to the outside world and that any classical communication between Alice and Bob occurs only after measurement outcomes have been produced [180].

Sequential Use and Memory Effects. A more subtle issue arises from the sequential reuse of the same devices over many rounds. Since the devices are treated as black boxes, they may contain arbitrary internal memory and behave adaptively depending on previous inputs and outputs [231, 220]. In particular, an adversarially prepared device could correlate its behavior across rounds, invalidating security analyses that assume i.i.d. behavior.

Device-independent security proofs therefore make no independence assumption between rounds [181]. Instead, they model the entire protocol as a sequential quantum process, where the global state may evolve arbitrarily subject only to causality constraints. The Entropy Accumulation Theorem provides the essential tool to handle this setting: it guarantees that even when devices possess arbitrary memory, the total smooth min-entropy generated across n rounds grows approximately linearly with n, up to finite-size corrections [224, 181].

Operationally, the sequential structure of DI–QKD requires that input choices be generated freshly and independently in each round [220], and that no information about future inputs be accessible to the devices. Furthermore, classical communication used for sifting and parameter estimation must occur only after the measurement phase, preventing adaptive strategies within a single round [223].

Implications for Experimental Implementations. In practice, ensuring locality and controlling memory effects impose stringent requirements on experimental design [219]. Fast and independent random number generation is required for basis selection [220]. Timing constraints must guarantee that input choices are made after entangled states are distributed but before measurement outcomes are produced [187]. Shielding or physical separation must prevent unwanted cross-talk between devices [222].

Unlike standard QKD, where trusted device models allow more relaxed assumptions [230], DI–QKD must treat any unintended signaling or memory correlation as potentially adversarial [180]. Consequently, locality enforcement and robust handling of sequential device behavior are fundamental prerequisites for composable device-independent security [181].

5.5 Entanglement Sources for DI–QKD

High-quality sources of entangled quantum systems are a necessary resource for DI–QKD. Quality refers not only to robust violation of detection loophole-free Bell-inequalities, but also a high brightness B (or repetition rate R), as these two characteristics have a direct effect on the key rates obtained. In addition to the overall detection efficiency, decoherence in the channel (such as depolarization, dephasing, etc) will also degrade the quality of entanglement.

5.5.1 SPDC-Based Photonic Sources

A major step in experimental Bell tests was the development of spontaneous parametric down-conversion (SPDC) sources as a source of entangled photon pairs in the 1990's [232, 233], which offered much higher count rates than the first generation of experiments based on atomic cascade [234, 121]. The most efficient SPDC sources today are based on periodically poled nonlinear crystals in Sagnac interferometers, as shown in Fig. 5.5.1.

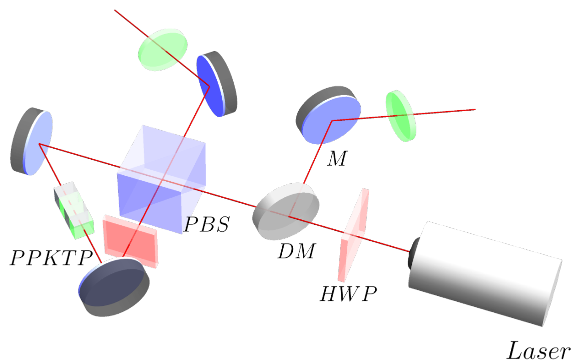

Figure 5.5.1: Sagnac source of entangled photons: A pump laser is directed through a half-wave plate (HWP) to control polarization, followed by a dichroic mirror (DM), which separates the pump beam by reflecting one wavelength while transmitting the other. The beam enters a polarizing beam splitter (PBS), splitting it into orthogonal polarization propagating paths. These paths pass through a periodically poled nonlinear crystal (PPKTP) inside the interferometer loop, generating photon pairs via SPDC. Mirrors (M) guide the beams, which recombine at the PBS. A HWP is placed in the reflecting path to adjust de polarization. The entangled photon pairs are separated using DMs and sent to high pass filters (green) to be detected at single-photon detectors. From Ref. [23].

An adequate choice of crystal length and optics produces highly pure entangled polarization states, reaching state fidelities over 99.5%, where the transverse spatial mode of the photons is optimized for coupling into single-mode fibers [235, 236, 207]. Coupling efficiencies over 95% have been achieved [207].

SPDC is a probabilistic source of photon pairs, and the state fidelities refer to the post-selected state obtained when two photons are registered. The full SPDC output is described by the two-mode squeezed vacuum state

$$|TMSV\rangle = \sum_{n=0}^{\infty} \frac{\bar{n}^{n/2}}{(1+\bar{n})^{(n+1)/2}} |n\rangle_1 \otimes |n\rangle_2, \tag{5.5.1}$$

where $\bar{n}$ is mean photon number in each mode $1, 2$. The ratio of multiple pair events to single pair events is $\bar{n}$, and the probability of a multi-pair event is $P_{n>1} = \bar{n}^2/(\bar{n}+1)^2$. Thus, there is a trade-off between the brightness achievable and the fidelity, since multiple-pair events become non-negligible at high pump beam intensity.

Since photons from different pairs are uncorrelated, multiple pair events limit the quality of the two-photon state, especially for pulsed sources [237]. Indeed, it has been shown that the absence of post-selection results in a limited violation of Bell inequalities [238]. The full photon statistics of state (5.5.1) have been considered in key rate analysis for DI-QKD [239], where it was shown that unity key rate is impossible, even with perfect detection efficiency. In addition, the authors showed that, by adding artificial noise, the critical detection efficiency can be lowered to 83.2%, even with the multi-photon events of SPDC sources.

SPDC sources have been used for point-to-point DI–QKD [207], and can also be incorporated into event-ready setups using absorptive quantum memories (see next section). The main parameters affecting performance of SPDC sources for point-to-point DI–QKD are the detection efficiency η, the overall brightness B (pairs emitted/time) and the quality of the entangled states reaching the measurement devices, which for simplicity we will describe in terms of a general decoherence channel $\mathcal{E}$, which may incorporate imperfections in the source as well as noise in the optical channel. The detection efficiency η affects the obtainable bit rate of these sources, since not only do both photons need to be detected to establish a key bit, but also through the obtainable loophole-free CHSH violation. Decoherence $\mathcal{E}$ can affect both the QBER as well as the CHSH violation. In some cases, decoherence is due to random unitaries operations (such as phase fluctuations or polarization rotations), which can be monitored and corrected. The source brightness B affects only the raw bit rate in principle, aside from multi-pair events that will result in uncorrelated events, increasing the QBER and lowering the CHSH value.

5.5.2 Stationary Nodes and Quantum Memories

Stationary quantum systems constitute a central building block for scalable DI–QKD and quantum networking [240, 241]. Platforms such as trapped ions, neutral atoms, nitrogen-vacancy (NV) centers in diamond, and semiconductor quantum dots combine high-fidelity local control with near-unity detection efficiencies [242, 243]. In contrast to purely photonic systems, these platforms also offer the crucial ability to store quantum states for extended periods of time, enabling heralded entanglement generation and repeater-based architectures [244, 241].

In such systems, a long-lived matter qubit serves as a *node* of the network. Through optical excitation and spontaneous emission processes, the internal state of the node can be entangled with a photonic qubit emitted into an optical channel [240]. The emitted photon carries quantum information over long distances, while the stationary qubit retains coherence locally. This hybrid matter–photon interface enables remote entanglement generation via photonic interference and Bell-state measurements, forming the basis of event-ready schemes [188, 244].

Coherence Time and Distance Limitations

The usefulness of stationary nodes is fundamentally determined by their coherence properties. Decoherence processes, such as magnetic field fluctuations, spontaneous emission, or interactions with the surrounding environment, limit the lifetime of stored quantum states [242, 241]. This is typically quantified by the coherence time T_2, defined as the characteristic time over which phase coherence of a superposition state is preserved [3].

In distributed architectures, T_2 directly constrains the maximum separation distance L between nodes. Entanglement generation via a central station requires classical communication of the heralding signal to the nodes before measurements are completed [244]. The stored quantum state must therefore remain coherent for at least the communication time, implying

$$L \ll vT_2, \tag{5.5.2}$$

where v is the speed of light in the optical channel.

Recent experimental advances have demonstrated long coherence times in a variety of platforms, including atomic ensembles, trapped ions, and NV centers [187, 242, 243]. In particular, coherence times in the millisecond regime enable potential node separations on the order of tens to hundreds of kilometers, depending on system parameters and architecture [241]. Techniques such as dynamical decoupling and improved material engineering have significantly extended coherence lifetimes, making long-distance entanglement distribution increasingly feasible [242]. Long T_2 times are essential for maintaining high-fidelity entanglement, preserving Bell violations, and achieving the low quantum bit error rates required for DI–QKD [180].

Beyond two-node links, quantum memories are indispensable for quantum repeater protocols [244, 241]. By storing entanglement locally while additional segments are established, repeaters enable entanglement distribution over distances exceeding direct transmission limits. The development of long-lived, high-fidelity quantum memories is therefore a prerequisite for scalable DI–QKD networks [241, 243].

Telecom Compatibility and Frequency Conversion

A practical challenge for many stationary platforms is that their native optical transitions occur outside the low-loss telecom bands. For example, atomic and solid-state systems often emit photons in the visible or near-infrared regime, where fiber attenuation can be one to two orders of magnitude higher than at telecom wavelengths.

Quantum frequency conversion has emerged as a key enabling technology to address this mismatch. Using nonlinear optical processes such as difference-frequency generation driven by a strong pump field, single photons emitted by a quantum memory can be converted to telecom wavelengths while preserving quantum coherence [245, 246]. This approach has enabled long-distance entanglement distribution for spin systems and atomic ensembles [247, 248, 249, 250].

Telecom conversion therefore plays a dual role: it reduces transmission losses in optical fibers and allows heterogeneous quantum platforms to interoperate within a common photonic infrastructure. Combined with long coherence times and high detection efficiencies, frequency-converted stationary nodes provide a technologically promising route toward scalable, loophole-free DI–QKD implementations.

5.6 Event-Ready Architectures

Two recent DI-QKD experiments employed so-called *event-ready* entanglement sources [206, 208]. The motivation for such architectures arises directly from the detection loophole: since DI security forbids post-selection on detection events, losses cannot simply be discarded without invalidating the Bell test. Event-ready schemes address this limitation by conditioning each experimental round on an externally generated heralding signal.

In an event-ready architecture, successful creation of entanglement between remote nodes A and B is announced by a classical signal from a central station, as illustrated in Fig. 5.6.1. Only after this heralding event do the nodes perform local measurements for key generation. Because the validity of a trial is determined independently of the local detection outcomes, the fair-sampling assumption is avoided and the detection loophole can be closed.

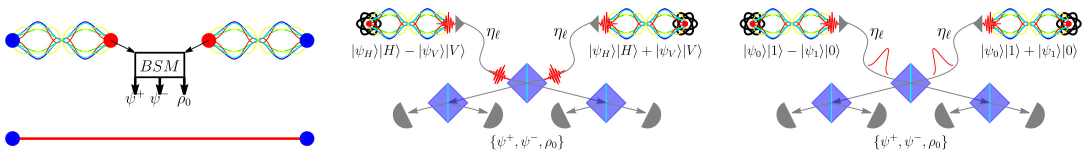

(a) *Basic concept* **(b)** *Polarization mode* **(c)** *Counting mode*

Figure 5.6.1: *Event–ready setups* – (a) Remote subsystems A and D of two entangled pairs are entangled via BSM on their entangled partners (B and C). (b) Event ready scheme with stationary qubits and two photon heralds. Stationary qubits are each entangled with the polarization state of a photon, which are are sent to a central station for the two-photon BSM. Joint detection events at pairs of detectors signal preparation of an entangled state $\psi^{\pm} = |\psi_H\rangle_A |\psi_H\rangle_B \pm |\psi_V\rangle_A |\psi_V\rangle_B$. (c) Stationary qubits each emit a photon with probability p. The optical modes are coupled, so that detection of one and only one photon results in an entangled state of the stationary qubits. Here, $\psi^{\pm} = |\psi_0\rangle_A |\psi_1\rangle_B \pm |\psi_1\rangle_A |\psi_0\rangle_B$.

All-photonic event-ready sources based on entanglement swapping have been demonstrated [40, 251, 252, 253, 254]. However, stationary quantum systems—such as trapped ions, neutral atoms, quantum dots, or NV centers—offer decisive advantages due to their near-unity detection efficiencies and ability to store quantum states. These properties make them particularly well suited for loophole-free Bell tests and DI-QKD implementations.

In practice, each node is locally entangled with a photonic qubit that is transmitted to a central station. A joint measurement performed on the photons heralds remote entanglement between A and B. With linear optics, the success probability of this BSM is fundamentally limited to at most 50% [23], and classical communication of the heralding outcome is required before proceeding. Optical decoherence in the channel, including phase or polarization fluctuations, directly reduces the fidelity of the distributed state.

Event-ready schemes fall into two main categories, distinguished by the number of photons required at the central station:

Double-Herald Schemes (Two-Photon Detection). In double-herald protocols, one photon from each node must arrive at the central station (Fig. 5.6.1b). Entanglement generation relies on two-photon interference, which is intrinsically robust against slow optical phase drifts [255]. Because both photons must be emitted, transmitted, and detected, the success probability scales as

$$p_{\mathrm{ent}} \sim \eta^2, \tag{5.6.1}$$

where η denotes the single-photon transmission and detection efficiency. Such schemes have enabled heralded entanglement over tens of kilometers using atomic ensembles and single atoms [248, 249].

Single-Photon Heralded Schemes. Single-photon protocols require detection of only one photon at the central station (Fig. 5.6.1c). Each node is prepared in a node–photon entangled state of the form

$$|\psi_0\rangle\,|1\rangle \pm |\psi_1\rangle\,|0\rangle\,, \tag{5.6.2}$$

where $|\psi_j\rangle$ are node states and $|n\rangle$ photonic Fock states. Interference of the optical modes ensures that the detection event does not reveal which node emitted the photon, thereby projecting the nodes into an entangled state. In this case,

$$p_{\mathrm{ent}} \sim \eta, \tag{5.6.3}$$

providing a linear scaling advantage in efficiency, at the expense of stringent phase stability requirements [256, 257, 258, 259, 260].

Event-ready protocols are inherently probabilistic and require repeated entanglement attempts separated by classical communication times. A central performance metric is the entanglement generation rate,

$$r_{\text{ent}} = p_{\text{ent}} R, \tag{5.6.4}$$

where R is the repetition rate. Decoherence competes with generation, and their ratio defines the link efficiency [257],

$$\eta_{\text{link}} = \frac{r_{\text{ent}}}{r_{\text{dec}}}, \tag{5.6.5}$$

with r_{dec} the memory decoherence rate. When $\eta_{\text{link}} \gtrsim 1$, entanglement can be delivered effectively deterministically by outputting a separable state upon failure.

Although heralding mitigates local detection inefficiencies, optical transmission losses remain a major scalability bottleneck. This limitation is particularly relevant because many quantum memories emit photons outside the telecom bands. Quantum frequency conversion to telecom wavelengths via difference-frequency generation [245, 246] has therefore become a key enabling technology, allowing long-distance entanglement distribution for spin systems and atomic ensembles [247, 248, 249, 250].

Alternative approaches include absorptive quantum memories coupled to SPDC sources [261, 262], direct photon-mediated memory entanglement [250], hybrid SPDC–memory interfaces over deployed fibers [263], and fully optical event-ready architectures based on qubit amplifiers [264, 265, 266, 267], derived from noiseless amplification concepts [268] and subject to stringent source and detection requirements [269].

Despite substantial progress and proof-of-principle demonstrations of DI-QKD using event-ready architectures [206, 208], present entanglement generation probabilities remain low, with reported values $p_{\text{ent}} \sim 10^{-4} - 10^{-6}$ [206, 208, 247, 270]. Bridging the gap toward practical long-distance DI-QKD will likely require major technical advances, including multiplexed entanglement generation and further improvements in photon collection and mode matching.

5.7 Entanglement Swapping

Entanglement swapping constitutes the fundamental mechanism underlying heralded entanglement distribution and quantum repeater architectures. It enables two systems that have never interacted directly to become entangled through a joint measurement performed on their respective partners [271, 89, 272].

Consider two independent maximally entangled pairs shared between systems (A, B) and (C, D),

$$\left|\Phi^+\right\rangle_{AB} \otimes \left|\Phi^+\right\rangle_{CD}, \tag{5.7.1}$$

where

$$\left|\Phi^\pm\right\rangle = \frac{1}{\sqrt{2}}(|00\rangle \pm |11\rangle), \qquad \left|\Psi^\pm\right\rangle = \frac{1}{\sqrt{2}}(|01\rangle \pm |10\rangle). \tag{5.7.2}$$

Rewriting the joint state in the Bell basis of systems B and C yields

$$\begin{aligned}\left|\Phi^+\right\rangle_{AB}\left|\Phi^+\right\rangle_{CD} = \frac{1}{2}\Big(&\left|\Phi^+\right\rangle_{BC}\left|\Phi^+\right\rangle_{AD} + \left|\Phi^-\right\rangle_{BC}\left|\Phi^-\right\rangle_{AD} \\ &+ \left|\Psi^+\right\rangle_{BC}\left|\Psi^+\right\rangle_{AD} + \left|\Psi^-\right\rangle_{BC}\left|\Psi^-\right\rangle_{AD}\Big).\end{aligned} \tag{5.7.3}$$

Equation (5.7.3) makes the swapping mechanism explicit: a BSM performed on subsystems B and C projects subsystems A and D onto the corresponding Bell state, conditioned on the measurement outcome. Thus, entanglement is transferred from the original pairs (A, B) and (C, D) to the previously independent pair (A, D).

The physical implementation of the BSM, typically relying on two-photon interference via the Hong–Ou–Mandel effect, was discussed in Chapter 2. Here we emphasize its architectural role. In practical DI–QKD implementations, the systems B and C correspond to photonic modes emitted from distant stationary nodes. A successful BSM event at a central station heralds the creation of entanglement between the remote matter qubits A and D. The classical announcement of the BSM outcome defines valid experimental rounds, enabling event-ready operation and eliminating reliance on fair-sampling assumptions.

From a networking perspective, entanglement swapping is the elementary step of quantum repeater protocols [272]. By concatenating multiple swapping operations, entanglement can be extended over distances exceeding the direct transmission length of optical fibers. In the context of DI–QKD, this scalability is essential:

maintaining a loophole-free Bell violation over large separations requires both heralded operation and the ability to distribute high-fidelity entanglement across extended networks.

Importantly, while the intrinsic success probability of linear-optical Bell-state measurements is limited, this constraint primarily affects the entanglement generation rate rather than the validity of device-independent security. The interplay between swapping efficiency, memory decoherence, and transmission losses ultimately determines whether practical long-distance DI–QKD can be achieved.

5.8 HOM Interference as an Enabling Resource

In photonic quantum communication, the primary experimental challenge is the simultaneous realization of high detection efficiency, high-fidelity entanglement, and loophole-free Bell violations without making assumptions about the internal functioning of the devices [219, 180]. This requirement is particularly stringent in DI–QKD, where security is certified directly from the observed Bell violation [180, 181]. Within this framework, Hong–Ou–Mandel (HOM) interference constitutes a central enabling resource [7].

Linear-optical Bell-state measurements, which are essential for entanglement swapping and event-ready architectures, rely fundamentally on two-photon interference at a beam splitter [273, 274]. The beam splitter itself performs only a linear mode transformation; the nonclassical projection onto symmetric or antisymmetric subspaces arises from the interference of indistinguishable two-photon probability amplitudes [7, 275]. Coincidence detection patterns then probabilistically identify specific Bell states [273]. The success probability and, more importantly, the fidelity of these projections depend directly on the degree of two-photon indistinguishability, quantified experimentally by the HOM visibility [275].

Imperfect indistinguishability reduces the interference contrast and therefore degrades the quality of the Bell-state projection [276]. In entanglement-swapping protocols, this translates into reduced fidelity of the swapped entangled state [188, 277]. In DI–QKD, the consequences are even more severe: any reduction in entanglement fidelity diminishes the achievable Bell violation, thereby weakening the bounds on an eavesdropper's information and potentially closing the security gap required for positive key rates [180, 220].

Crucially, the Bell-state measurement required for entanglement swapping involves interference between photons generated by independent and spatially separated sources [277, 278]. In this regime, two-photon indistinguishability is not merely a technical optimization parameter but a fundamental prerequisite for establishing nonlocal correlations [276]. High-visibility HOM interference ensures that the beam splitter implements the intended symmetry-sensitive projection, enabling heralded entanglement generation and event-ready Bell tests compatible with loophole-free operation [188, 187].

In this sense, HOM interference forms the physical backbone of photonic DI–QKD architectures: it mediates entanglement distribution, determines Bell-state discrimination fidelity, and ultimately governs the strength of the observed nonlocal correlations [219, 241].

5.9 Experimental Demonstrations of DI–QKD

The experimental realization of DI–QKD requires architectures capable of simultaneously generating entanglement, achieving high detection efficiencies, and enabling loophole-free Bell tests under realistic conditions. While the theoretical security of DI–QKD is independent of the internal functioning of the devices, the feasibility of its implementation is intrinsically tied to the physical platform and experimental design. In this section, we discuss the current outlook towards real-world implementation of DI-QKD, presenting the first set of DI-QKD experiments.

Table 5.9.1 lists the major fully DI-QKD experiments reported in the literature from 2022 to 2026. The table focuses on platforms that explicitly aim at device-independent security, event-ready architectures, and measurable Bell violations, along with the distances achieved and any available key rate information. Where specific values are not reported in the published accounts, the table indicates that data is unavailable ("n/a").

More recent experimental progress further demonstrates rapid advances toward scalable implementations, including long-distance DI–QKD with single atoms and photonic platforms achieving Bell violations and positive key rates over tens to

100 km scales [190].

Table 5.9.1: Key experimental DI-QKD demonstrations.

Experiment	Platform	Source type	Bell violation	Distance / Key rate
Liu et al. (2022)	Photonic entangled pairs	SPDC	n/a	up to 220 m, positive key rate (asymptotic)
Nadlinger et al. (2022)	Trapped ions	Atomic entanglement	$S > 2$	~ 2 m, ~ 0.064 bits/round
Zhang et al. (2022)	Trapped atoms	Single atoms	$S = 2.578(75)$	400 m (700 m fiber), ~ 0.07 bits/event
Lu et al. (2026)	Single atoms (networked)	Atom–photon interface	$S > 2$	~ 100 km, positive key rate

The first DI-QKD Experiments

In July 2022, three independent research groups (one based in the UK [206], one in Germany [208], and one in China [207]) successfully implemented DI-QKD in three different platforms. The first successful photonic-based experiment [207] demonstrated DI-QKD over fiber lengths of $d = 20, 100$ and 220 m and verified that the measured correlations between the entangled photons were strong enough to guarantee a positive secret key rate. Optimized high-efficiency entangled photon source and single-photon detectors resulted in a single photon heralding efficiency slightly greater than 87%. To address the locality loophole, the experiment employs a shielding assumption that prohibits unnecessary communications between untrusted devices and a potential adversary. Essentially, it ensures that the information about the input choices and output results of one party remains unknown to the other party and Eve.

Proof-of-principle memory-based experiments reported in Oxford [206] and Munich [208] used entangled strontium ions and entangled rubidium atoms, respectively. Each system has it's advantages and disadvantages. However, when compared to all-photonic implementations, these experiments have the advantage that they can be event-ready, so that link efficiencies can be partially mitigated. The Oxford-based experiment was the only one of the three to complete the entire DI-QKD protocol, with a generated secret key of 95 kbits between Alice and Bob achieved over about 8 hours and with a distance of $d = 2$ m between the two quantum memories. The Munich-based experiment created heralded entanglement between atoms separated by a line of sight distance of $d = 400$m (700m of optical fiber). An asymptotic security analysis was performed, and a secret key rate of 0.07 bits per entanglement generation event was obtained from results accumulated over 75 hours.

These three landmark experiments demonstrate that experimental DI-QKD is feasible. In addition, they highlight the technical challenges to be face in achieving real-world utility.

5.10 Toward Scalable DI–QKD Networks

Scaling DI–QKD to practical distances and key rates requires architectures that combine high-quality entanglement generation with efficient and robust distribution [241, 244]. Photonic platforms are particularly promising due to their compatibility with existing fiber-optic infrastructure, but scalability remains constrained by source quality, detection efficiency, and probabilistic operation [219, 279].

High-performance photon sources must simultaneously achieve high brightness, low multi-pair emission probability, and near-perfect indistinguishability [244]. Advances in engineered spontaneous parametric down-conversion and solid-state emitters provide viable routes toward these requirements [242]. In parallel, high-efficiency and low-noise single-photon detectors—particularly superconducting nanowire detectors—are essential to meet the stringent detection thresholds required for loophole-free Bell tests [280, 219].

A central limitation of current DI–QKD implementations is the extremely low secret key rate, primarily due to the probabilistic nature of entanglement generation and linear-optical Bell-state measurements [244]. Multiplexing techniques, including temporal, spectral, and spatial multiplexing, provide a natural route to overcome this limitation by enabling multiple parallel entanglement attempts [279, 281]. However, such architectures impose stringent requirements on photon indistinguishability, as high-visibility Hong–Ou–Mandel interference must be preserved across all modes.

Beyond rate enhancement, entanglement swapping based on HOM interference forms the basis of quantum repeater architectures, which are essential for extending DI–QKD beyond direct transmission limits [244, 241]. While full-scale repeaters remain experimentally challenging, intermediate repeater-like nodes based on heralded entanglement swapping already enable extended distances and improved loss tolerance.

Overall, scalable DI–QKD networks will require the integration of high-quality sources, efficient detectors, multiplexed architectures, and repeater-based designs within phase-stable and synchronized systems [241]. In this context, HOM interference remains a central resource, underpinning both entanglement distribution and Bell-state measurements, and thus governing the performance of large-scale device-independent quantum communication networks.

Summary

DI-QKD derives its security directly from the violation of a Bell inequality. The observed Bell parameter bounds the adversary's information through entropy relations, linking nonlocal correlations to certified randomness and secret key generation. However, the realization of loophole-free Bell violations in photonic systems is constrained by transmission losses and limited detection efficiencies, giving rise to the detection loophole.

Event-ready architectures address this challenge by heralding successful entanglement distribution before measurement choices are made. Entanglement swapping enables such heralded configurations by projecting two independently generated entangled pairs onto a Bell state, thereby creating remote entanglement between distant nodes. This projection is implemented through linear-optical Bell-state measurements, whose physical mechanism is two-photon interference at a beam splitter.

At the most fundamental level, Hong–Ou–Mandel interference provides the symmetry-sensitive projection that underpins Bell-state discrimination. High-visibility HOM interference between independent photons is therefore a prerequisite for high-fidelity entanglement swapping, strong Bell violations, and ultimately positive device-independent key rates. Experimental implementations must simultaneously ensure photon indistinguishability, low-loss transmission, high detection efficiency, and stable interference across all relevant degrees of freedom.

The primary technological bottlenecks remain transmission losses in optical fibers, limited detector efficiencies, imperfect photon indistinguishability, and reduced Bell-state measurement success probabilities inherent to linear optics. These constraints limit entanglement distribution rates and impose stringent requirements on source brightness, spectral purity, and interferometric stability.

Pathways toward practical deployment include improved single-photon sources with higher purity and indistinguishability, low-loss fiber infrastructures, high-efficiency superconducting detectors, multiplexing strategies in spatial and spectral domains, and integrated photonic platforms enabling stable large-scale interference. In particular, scalable architectures based on multicore and multimode fibers offer promising routes toward parallelized entanglement distribution and increased key rates.

In perspective, HOM interference emerges not merely as a textbook demonstration of two-photon quantum behavior, but as a foundational operational primitive for photonic quantum networks. Its faithful implementation determines the quality of Bell-state measurements, the viability of entanglement swapping, and the strength of device-independent security guarantees. Advancing the control of multi-photon interference in realistic, scalable platforms is therefore a central step toward practical, long-distance, and fully device-independent quantum communication.

Chapter 6

Conclusion

This thesis has explored the role of Hong–Ou–Mandel (HOM) interference as a fundamental and versatile resource in photonic quantum information, with particular emphasis on its extension to multiport photonic devices and its relevance for emerging quantum communication protocols.

From a theoretical perspective, we revisited the foundations of HOM interference, highlighting its dependence on photon indistinguishability and its sensitivity to temporal, spectral, and spatial mismatches. This analysis was extended to multiport interferometric architectures, where interference is no longer restricted to two modes, giving rise to higher-dimensional quantum effects. These results reinforce the interpretation of HOM interference as a powerful diagnostic tool for complex photonic systems, while also revealing the increased sensitivity of multiport configurations to experimental imperfections.

The main experimental contribution of this work was the demonstration of sub-picosecond inter-core skew characterization in multicore fibers using HOM interference. This result establishes HOM interference as a high-resolution metrological technique, capable of resolving ultrafine temporal delays that are otherwise challenging to access with classical methods. The ability to characterize multicore fibers with such precision is particularly relevant for the development of scalable photonic networks, where synchronization and indistinguishability across multiple channels are critical.

In addition, this thesis has positioned HOM interference within the broader landscape of quantum communication, particularly in the context of Device-

Independent Quantum Key Distribution (DIQKD). Through a structured review of the literature, we analyzed the current experimental state of the art, including implementations based on SPDC sources and the main limitations hindering practical deployment. The connections with Measurement-Device-Independent QKD (MDI-QKD) further highlight the central role of two-photon interference in enabling secure quantum protocols under realistic conditions.

Taken together, the results presented in this thesis establish a coherent link between fundamental quantum interference, scalable photonic architectures, and quantum communication technologies. In particular, the extension of HOM interference to multiport systems and its application to precise metrology demonstrate its relevance beyond foundational studies, positioning it as a key operational tool in future quantum networks.

Looking forward, several research directions naturally emerge from this work. First, the extension of HOM-based characterization techniques to more complex and reconfigurable integrated photonic platforms could enable real-time calibration of large-scale quantum circuits. Second, the integration of multicore fiber systems with multiport interferometers opens new possibilities for high-dimensional quantum interference experiments. Finally, further exploration of the interplay between HOM interference and MDI- and DIQKD protocols may provide practical pathways toward more robust and scalable implementations of quantum-secure communication.

In this context, HOM interference is not only a hallmark quantum effect, but also a practical and unifying tool bridging theory, experiment, and applications in quantum photonics.

Bibliography

[1] Rodney Loudon. *The quantum theory of light*. OUP Oxford, 2000.

[2] Christopher C Gerry and Peter L Knight. *Introductory quantum optics*. Cambridge university press, 2023.

[3] Michael A Nielsen and Isaac L Chuang. *Quantum computation and quantum information*. Cambridge university press, 2010.

[4] Thomas Young. "II. The Bakerian Lecture. On the theory of light and colours". In: *Philosophical transactions of the Royal Society of London* 92 (1802), pp. 12–48.

[5] Leonard Mandel and Emil Wolf. *Optical coherence and quantum optics*. Cambridge university press, 1995.

[6] Berthold-Georg Englert. "Fringe visibility and which-way information: An inequality". In: *Physical review letters* 77.11 (1996), p. 2154.

[7] Chong-Ki Hong, Zhe-Yu Ou, and Leonard Mandel. "Measurement of subpicosecond time intervals between two photons by interference". In: *Physical review letters* 59.18 (1987), p. 2044.

[8] Charles Santori et al. "Indistinguishable photons from a single-photon device". In: *nature* 419.6907 (2002), pp. 594–597.

[9] JC Loredo et al. "Generation of non-classical light in a photon-number superposition". In: *Nature Photonics* 13.11 (2019), pp. 803–808.

[10] Thomas Legero et al. "Quantum beat of two single photons". In: *Physical review letters* 93.7 (2004), p. 070503.

[11] Zhe Y Ou and Leonard Mandel. "Violation of Bell's inequality and classical probability in a two-photon correlation experiment". In: *Physical review letters* 61.1 (1988), p. 50.

[12] Benjamin J Puttnam et al. "Characteristics of homogeneous multi-core fibers for SDM transmission". In: *APL photonics* 4.2 (2019).

[13] Ruben S Luis et al. "Compensation of inter-core skew in multi-core fibers with group velocity dispersion". In: *Optics Express* 29.18 (2021), pp. 28104–28109.

[14] David J Richardson, John M Fini, and Lynn E Nelson. "Space-division multiplexing in optical fibres". In: *Nature photonics* 7.5 (2013), pp. 354–362.

[15] Benjamin J Puttnam, Georg Rademacher, and Ruben S Luís. "Space-division multiplexing for optical fiber communications". In: *optica* 8.9 (2021), pp. 1186–1203.

[16] Tetsuya Hayashi. "Accuracy of analytical expressions for Rayleigh backscattered crosstalk in bidirectional multi-core fiber transmissions". In: *Optics Express* 30.13 (2022), pp. 23943–23952.

[17] Meng Ye et al. "Experimental Hong—Ou—Mandel interference using two independent heralded single-photon sources". In: *Frontiers of Optoelectronics* 14.3 (2021), pp. 360–364.

[18] Xiao-Hai Zhan et al. "Experimental demonstration of long distance quantum communication with independent heralded single photon sources". In: *npj Quantum Information* 11.1 (2025), p. 73.

[19] Emanuel Knill, Raymond Laflamme, and Gerald J Milburn. "A scheme for efficient quantum computation with linear optics". In: *nature* 409.6816 (2001), pp. 46–52.

[20] Fabrice Devaux et al. "Imaging spatiotemporal hong-ou-mandel interference of biphoton states of extremely high schmidt number". In: *Physical Review X* 10.3 (2020), p. 031031.

[21] Guilherme B Xavier and Gustavo Lima. "Quantum information processing with space-division multiplexing optical fibres". In: *Communications Physics* 3.1 (2020), p. 9.

[22] Kunimasa Saitoh and Shoichiro Matsuo. "Multicore fiber technology". In: *Journal of lightwave technology* 34.1 (2016), pp. 55–66.

[23] Seyed Arash Ghoreishi et al. "The future of secure communications: Device independence in quantum key distribution". In: *Physics Reports* 1149 (2025). The future of secure communications: device independence in quantum key distribution, pp. 1–97. ISSN: 0370-1573. DOI: https://doi.org/10.1016/j.physrep.2025.09.006. URL: https://www.sciencedirect.com/science/article/pii/S0370157325002558.

[24] Zhe-Yu Jeff Ou. *Multi-photon quantum interference*. Vol. 43. Springer, 2007.

[25] Frédéric Bouchard et al. "Two-photon interference: the Hong–Ou–Mandel effect". In: *Reports on Progress in Physics* 84.1 (2021), p. 012402.

[26] Nicolas Fabre et al. "The Hong–Ou–Mandel experiment: from photon indistinguishability to continuous-variable quantum computing". In: *The European Physical Journal D* 76.10 (2022), p. 196.

[27] Agata M Brańczyk. "Hong-ou-mandel interference". In: *arXiv preprint arXiv:1711.00080* (2017).

[28] SP Walborn et al. "Multimode hong-ou-mandel interference". In: *Physical review letters* 90.14 (2003), p. 143601.

[29] Marlan O Scully and M Suhail Zubairy. *Quantum optics*. Cambridge university press, 1997.

[30] Anthony Mark Fox. *Quantum optics: an introduction*. Vol. 15. Oxford university press, 2006.

[31] Roy J Glauber. "The quantum theory of optical coherence". In: *Physical Review* 130.6 (1963), p. 2529.

[32] Matthias Englbrecht et al. "Indistinguishability of identical bosons from a quantum information theory perspective". In: *Physical Review Letters* 132.5 (2024), p. 050201.

[33] Christian Drago and Agata M Brańczyk. "Hong–Ou–Mandel interference: A spectral–temporal analysis". In: *Canadian journal of physics* 102.8 (2024), pp. 411–421.

[34] Roy Barzel and Claus Lämmerzahl. "Role of indistinguishability and entanglement in Hong-Ou-Mandel interference and finite-bandwidth effects of frequency-entangled photons". In: *Physical Review A* 107.3 (2023), p. 032205.

[35] H Ollivier et al. "Hong-Ou-Mandel interference with imperfect single photon sources". In: *Physical Review Letters* 126.6 (2021), p. 063602.

[36] Sonali Gera et al. "Hong-Ou-Mandel interference of single-photon-level pulses stored in independent room-temperature quantum memories". In: *npj Quantum Information* 10.1 (2024), p. 10.

[37] Fulvio Flamini, Nicolo Spagnolo, and Fabio Sciarrino. "Photonic quantum information processing: a review". In: *Reports on Progress in Physics* 82.1 (2019), p. 016001.

[38] Pieter Kok et al. "Linear optical quantum computing with photonic qubits". In: *Reviews of modern physics* 79.1 (2007), pp. 135–174.

[39] Anton Zeilinger. "Bell's theorem, information and quantum physics". In: *Quantum [Un] speakables: From Bell to Quantum Information*. Springer, 2012, pp. 241–254.

[40] Jian-Wei Pan et al. "Experimental entanglement swapping: entangling photons that never interacted". In: *Physical review letters* 80.18 (1998), p. 3891.

[41] Hoi-Kwong Lo, Marcos Curty, and Bing Qi. "Measurement-device-independent quantum key distribution". In: *Physical review letters* 108.13 (2012), p. 130503.

[42] Johannes Borregaard et al. "Efficient quantum computation in a network with probabilistic gates and logical encoding". In: *Physical Review A* 95.4 (2017), p. 042312.

[43] L Mandel. "Photon interference and correlation effects produced by independent quantum sources". In: *Physical Review A* 28.2 (1983), p. 929.

[44] Shi-Hai Wei et al. "Towards real-world quantum networks: a review". In: *Laser & Photonics Reviews* 16.3 (2022), p. 2100219.

[45] VS Shchesnovich. "Partial indistinguishability theory for multiphoton experiments in multiport devices". In: *Physical Review A* 91.1 (2015), p. 013844.

[46] Yoshiaki Tsujimoto et al. "High visibility Hong-Ou-Mandel interference via a time-resolved coincidence measurement". In: *Optics express* 25.11 (2017), pp. 12069–12080.

[47] Noah Crum, Md Mehdi Hassan, and George Siopsis. "Mode distinguishability in multiphoton interference". In: *Physical Review A* 113.1 (2026), p. 013734.

[48] Cyrus Bjurlin and Theresa Chmiel. "A versatile Hong–Ou–Mandel interference experiment in optical fiber for the undergraduate laboratory". In: *American Journal of Physics* 93.2 (2025), pp. 180–186.

[49] Yiwei Zhai et al. “Fiber-optic quantum gyroscope based on Hong-Ou-Mandel interferometry”. In: *Optics & Laser Technology* 187 (2025), p. 112846.

[50] Zhiguang Xia et al. “Dispersion broadening of the two-photon quantum interference width due to temporal filtering”. In: *Physical Review Applied* 20.4 (2023), p. 044080.

[51] Malte C Tichy et al. “Many-particle interference beyond many-boson and many-fermion statistics”. In: *New Journal of Physics* 14.9 (2012), p. 093015.

[52] Richard A Campos, Bahaa EA Saleh, and Malvin C Teich. “Quantum-mechanical lossless beam splitter: SU (2) symmetry and photon statistics”. In: *Physical Review A* 40.3 (1989), p. 1371.

[53] Toralf Gruner and Dirk-Gunnar Welsch. “Antibunching of distorted optical wave packets at a beam splitter”. In: *Optics communications* 154.5-6 (1998), pp. 300–306.

[54] A Ourjoumtsev et al. “Two-photon quantum interference for an undergraduate lab”. In: *European Journal of Physics* 36.6 (2015), p. 065034.

[55] Si Wang et al. “Research on the Hong-Ou-Mandel interference with two independent sources”. In: *Scientific Reports* 9.1 (2019), p. 3854.

[56] Audrey Eshun et al. “Investigations of molecular optical properties using quantum light and Hong–Ou–Mandel interferometry”. In: *Journal of the American Chemical Society* 143.24 (2021), pp. 9070–9081.

[57] Kevin A Fischer et al. “Dynamical modeling of pulsed two-photon interference”. In: *New Journal of Physics* 18.11 (2016), p. 113053.

[58] Rui-Bo Jin et al. “Spectrally resolved Hong-Ou-Mandel interference between independent photon sources”. In: *Optics Express* 23.22 (2015), pp. 28836–28848.

[59] A Ferreri et al. “Temporally multimode four-photon Hong-Ou-Mandel interference”. In: *Physical Review A* 100.5 (2019), p. 053829.

[60] Dmitry N Makarov. “Fluctuations in the detection of the HOM effect”. In: *Scientific Reports* 10.1 (2020), p. 20124.

[61] Urbasi Sinha and Debadrita Ghosh. “Interference in Quantum Mechanics: U. Sinha and D. Ghosh”. In: *Journal of the Indian Institute of Science* 105.1 (2025), pp. 63–83.

[62] Adeline Orieux et al. “Semiconductor devices for entangled photon pair generation: a review”. In: *Reports on Progress in Physics* 80.7 (2017), p. 076001.

[63] Thomas Gerrits et al. “Spectral correlation measurements at the Hong-Ou-Mandel interference dip”. In: *Physical Review A* 91.1 (2015), p. 013830.

[64] FW Sun and CW Wong. “Indistinguishability of independent single photons”. In: *Physical Review A—Atomic, Molecular, and Optical Physics* 79.1 (2009), p. 013824.

[65] Nijil Lal, Sarika Mishra, and RP Singh. “Indistinguishable photons”. In: *AVS Quantum Science* 4.2 (2022).

[66] Benjamin Kambs and Christoph Becher. “Limitations on the indistinguishability of photons from remote solid state sources”. In: *New Journal of Physics* 20.11 (2018), p. 115003.

[67] Yuanyuan Chen, Ling Hong, and Lixiang Chen. “Quantum interferometric metrology with entangled photons”. In: *Frontiers in Physics* 10 (2022), p. 892519.

[68] Ludwig Mach. “Ueber einen interferenzrefraktor”. In: *Zeitschrift für Instrumentenkunde* 12.3 (1892), p. 89.

[69] Max Born and Emil Wolf. *Principles of optics: electromagnetic theory of propagation, interference and diffraction of light*. Elsevier, 2013.

[70] Tareq Jaouni et al. “Tutorial: Hong–Ou–Mandel interference with structured photons”. In: *Nanophotonics* 14.23 (2025), pp. 4163–4175.

[71] Giuliana Di Martino. “Quantum plasmonics: from quantum statistics to quantum interferences”. In: *Reviews in Plasmonics 2015*. Springer, 2016, pp. 295–313.

[72] Zacharie M Léger et al. “Deterministically separable polarization-entangled photons from battery-powered diode lasers”. In: *npj Quantum Information* 11.1 (2025), p. 128.

[73] Niels Ubbelohde et al. “Two electrons interacting at a mesoscopic beam splitter”. In: *Nature Nanotechnology* 18.7 (2023), pp. 733–740.

[74] Zheshen Zhang et al. “Entanglement-based quantum information technology: a tutorial”. In: *Advances in Optics and Photonics* 16.1 (2024), pp. 60–162.

[75] Navin B Lingaraju et al. “Quantum frequency combs and Hong–Ou–Mandel interferometry: the role of spectral phase coherence”. In: *Optics express* 27.26 (2019), pp. 38683–38697.

[76] Salim Ourari et al. “Indistinguishable telecom band photons from a single Er ion in the solid state”. In: *Nature* 620.7976 (2023), pp. 977–981.

[77] Demid V Sychev et al. “Entanglement and teleportation between polarization and wave-like encodings of an optical qubit”. In: *Nature communications* 9.1 (2018), p. 3672.

[78] Michael G Raymer and Ian A Walmsley. “Temporal modes in quantum optics: then and now”. In: *Physica Scripta* 95.6 (2020), p. 064002.

[79] Kaisa Laiho et al. “Unfolding the Hong–Ou–Mandel interference between heralded photons from narrowband twin beams”. In: *New Journal of Physics* 25.8 (2023), p. 083008.

[80] Konstantin E Dorfman et al. “Hong-Ou-Mandel interferometry and spectroscopy using entangled photons”. In: *Communications Physics* 4.1 (2021), p. 49.

[81] Carl W Helstrom. “Quantum detection and estimation theory”. In: *Journal of statistical physics* 1.2 (1969), pp. 231–252.

[82] Samuel L Braunstein and Carlton M Caves. “Statistical distance and the geometry of quantum states”. In: *Physical Review Letters* 72.22 (1994), p. 3439.

[83] Vittorio Giovannetti, Seth Lloyd, and Lorenzo Maccone. "Quantum-enhanced measurements: beating the standard quantum limit". In: *Science* 306.5700 (2004), pp. 1330–1336.

[84] Yan Guo et al. "Comparison of multi-mode Hong-Ou-Mandel interference and multi-slit interference". In: *Optics Express* 31.20 (2023), pp. 32849–32864.

[85] Yongqiang Li et al. "Stable and High-Precision 3D Positioning via Tunable Composite-Dimensional Hong-Ou-Mandel Interference". In: *Physical Review Letters* 135.26 (2025), p. 260804.

[86] Harald Weinfurter. "Experimental Bell-state analysis". In: *EPL (Europhysics Letters)* 25.8 (1994), pp. 559–564.

[87] Yong-Su Kim et al. "Informationally symmetrical Bell state preparation and measurement". In: *Optics express* 26.22 (2018), pp. 29539–29549.

[88] Denis Sych and Gerd Leuchs. "A complete basis of generalized Bell states". In: *New Journal of Physics* 11.1 (2009), p. 013006.

[89] M. Żukowski et al. ""Event-ready-detectors" Bell experiment via entanglement swapping". In: *Phys. Rev. Lett.* 71 (26 Dec. 1993), pp. 4287–4290. DOI: 10.1103/PhysRevLett.71.4287. URL: https://link.aps.org/doi/10.1103/PhysRevLett.71.4287.

[90] Stefano Pirandola et al. "Advances in quantum teleportation". In: *Nature photonics* 9.10 (2015), pp. 641–652.

[91] John Calsamiglia and Norbert Lütkenhaus. "Maximum efficiency of a linear-optical Bell-state analyzer". In: *Applied Physics B* 72.1 (2001), pp. 67–71.

[92] Norbert Lütkenhaus, John Calsamiglia, and K-A Suominen. "Bell measurements for teleportation". In: *Physical Review A* 59.5 (1999), p. 3295.

[93] Matthäus Halder et al. "Entangling independent photons by time measurement". In: *Nature physics* 3.10 (2007), pp. 692–695.

[94] Christian Dangel et al. "Two-photon interference of single photons from dissimilar sources". In: *Physical Review Applied* 18.5 (2022), p. 054005.

[95] Rainer Kaltenbaek et al. "High-fidelity entanglement swapping with fully independent sources". In: *Physical Review A—Atomic, Molecular, and Optical Physics* 79.4 (2009), p. 040302.

[96] Yingwen Zhang et al. "Engineering two-photon high-dimensional states through quantum interference". In: *Science advances* 2.2 (2016), e1501165.

[97] Zhi-Feng Liu et al. "Hong-Ou-Mandel interference between two hyperentangled photons enables observation of symmetric and antisymmetric particle exchange phases". In: *Physical Review Letters* 129.26 (2022), p. 263602.

[98] Yuanyuan Chen et al. "Temporal distinguishability in Hong-Ou-Mandel interference for harnessing high-dimensional frequency entanglement". In: *npj Quantum Information* 7.1 (2021), p. 167.

[99] Ling Hong et al. "Fast Quantifier of High-Dimensional Frequency Entanglement through Hong–Ou–Mandel Interference". In: *Advanced Quantum Technologies* 6.6 (2023), p. 2300012.

[100] B. Ndagano and A. Forbes. "Entanglement distillation by Hong–Ou–Mandel interference with orbital angular momentum states". In: *APL Photonics* 4 (2019). DOI: 10.1063/1.5054275.

[101] K. Zielnicki and K. Garay-Palmett. "Joint spectral characterization of photon-pair sources". In: *Journal of Modern Optics* (2018). DOI: 10.1080/09500340.2018.1437228.

[102] P. Yepiz-Graciano and A. M. A. Martínez. "Spectrally resolved Hong–Ou–Mandel interferometry for quantum-optical coherence tomography". In: *Photonics Research* 8 (2020). DOI: 10.1364/PRJ.8.001023.

[103] Y. Chen et al. "Hong-Ou-Mandel interferometry on a biphoton beat note". In: *npj Quantum Information* 5 (2019). DOI: 10.1038/s41534-019-0161-z.

[104] X. Gao et al. "High-speed imaging of spatiotemporal correlations in Hong-Ou-Mandel interference". In: *Optics Express* 30 (2022). DOI: 10.1364/OE.456433.

[105] H. Scott et al. "Beyond coincidence in Hong-Ou-Mandel interferometry". In: *Physical Review A* 102 (2020). DOI: 10.1103/PhysRevA.102.033714.

[106] Y. Tsujimoto et al. "Quantum state tomography of qudits via Hong-Ou-Mandel interference". In: *Physical Review Applied* 19 (2023). DOI: 10.1103/PhysRevApplied.19.014008.

[107] E. Knill, R. Laflamme, and G. J. Milburn. "A scheme for efficient quantum computation with linear optics". In: *Nature* 409 (2001), pp. 46–52. DOI: 10.1038/35051009.

[108] P. Kok et al. "Linear optical quantum computing with photonic qubits". In: *Reviews of Modern Physics* 79 (2007), pp. 135–174. DOI: 10.1103/RevModPhys.79.135.

[109] T. C. Ralph, K. J. Resch, and A. Gilchrist. "Efficient Toffoli gates using qudits". In: *Physical Review A* 75 (2007). Early LOQC gate proposals based on post-selection.

[110] J. L. O'Brien et al. "Demonstration of an all-optical quantum controlled-NOT gate". In: *Nature* 426 (2003), pp. 264–267. DOI: 10.1038/nature02054.

[111] B. J. Metcalf et al. "Multiphoton quantum interference in a multiport integrated photonic device". In: *Nature Communications* 4 (2013), p. 1356. DOI: 10.1038/ncomms2349. URL: https://doi.org/10.1038/ncomms2349.

[112] K. M. Jordan, R. A. Abrahao, and J. S. Lundeen. "Quantum metrology timing limits of the Hong-Ou-Mandel interferometer and of general two-photon measurements". In: *Physical Review A* 106 (2022). DOI: 10.1103/PhysRevA.106.063715.

[113] A. Lyons et al. "Attosecond-resolution Hong–Ou–Mandel interferometry". In: *Science Advances* 4 (2018). DOI: 10.1126/sciadv.aap9416.

[114] S. Singh, V. Kumar, and G. K. Samanta. "Fast measurement of group index variation using Hong–Ou–Mandel interferometry". In: *APL Quantum* (2024). DOI: 10.1063/5.0220993.

[115] E. Descamps, A. Keller, and P. Milman. "Time-frequency metrology with two single-photon states: Phase-space picture and the Hong-Ou-Mandel

interferometer". In: *Physical Review A* 108 (2023). DOI: 10.1103/PhysRevA.108.013707.
[116] JG Rarity, PR Tapster, and R Loudon. "Non-classical interference between independent sources". In: *Journal of Optics B: Quantum and Semiclassical Optics* 7.7 (2005), S171–S175.
[117] S. Wengerowsky et al. "An entanglement-based wavelength-multiplexed quantum communication network". In: *Nature* 564 (2018), pp. 225–228. DOI: 10.1038/s41586-018-0766-y.
[118] J. F. Dynes et al. "Cambridge quantum network". In: *npj Quantum Information* 5 (2019), p. 101. DOI: 10.1038/s41534-019-0221-4. URL: https://doi.org/10.1038/s41534-019-0221-4.
[119] Hui Wang et al. "Scalable photonic quantum technologies". In: *Nature Materials* 24.12 (2025), pp. 1883–1897.
[120] Jeremy L O'brien, Akira Furusawa, and Jelena Vučković. "Photonic quantum technologies". In: *Nature photonics* 3.12 (2009), pp. 687–695.
[121] Alain Aspect, Jean Dalibard, and Gérard Roger. "Experimental test of Bell's inequalities using time-varying analyzers". In: *Physical review letters* 49.25 (1982), p. 1804. DOI: 10.1103/PhysRevLett.49.1804.
[122] Tavshabad Kaur, Daniel Peace, and Jacquiline Romero. "On-chip high-dimensional entangled photon sources". In: *Journal of Optics* 27.2 (2025), p. 023001.
[123] Yuchen Wang et al. "Qudits and high-dimensional quantum computing". In: *Frontiers in Physics* 8 (2020), p. 589504.
[124] Nicola Montaut et al. "Progress in integrated and fiber optics for time-bin based quantum information processing". In: *Advanced optical technologies* 14 (2025), p. 1560084.
[125] J Cariñe et al. "Multi-core fiber integrated multi-port beam splitters for quantum information processing". In: *Optica* 7.5 (2020), pp. 542–550.
[126] Haoqi Zhao et al. "Integrated preparation and manipulation of high-dimensional flying structured photons". In: *eLight* 4.1 (2024), p. 10.
[127] Jun Liu et al. "Multidimensional entanglement transport through single-mode fiber". In: *Science advances* 6.4 (2020), eaay0837.
[128] Pieter Kok and Brendon W Lovett. *Introduction to optical quantum information processing*. Cambridge university press, 2010.
[129] Fulvio Flamini et al. "Benchmarking integrated linear-optical architectures for quantum information processing". In: *Scientific Reports* 7.1 (2017), p. 15133.
[130] M. Erhard et al. "Twisted photons: new quantum perspectives in high dimensions". In: *Light: Science & Applications* 7 (2018), p. 17146. DOI: 10.1038/lsa.2017.146.
[131] MA Sagioro et al. "Time control of two-photon interference". In: *Physical Review A—Atomic, Molecular, and Optical Physics* 69.5 (2004), p. 053817.
[132] Guifang Li et al. "Space-division multiplexing: the next frontier in optical communication". In: *Advances in optics and photonics* 6.4 (2014), pp. 413–487.

[133] Takashi Matsui, Peter L Pondillo, and Kazuhide Nakajima. "Weakly coupled multicore fiber technology, deployment, and systems". In: *Proceedings of the IEEE* 110.11 (2022), pp. 1772–1785.

[134] Georg Rademacher et al. "A comparative study of few-mode fiber and coupled-core multi-core fiber transmission". In: *Journal of Lightwave Technology* 40.6 (2022), pp. 1590–1596.

[135] Peter J Mosley et al. "Heralded generation of ultrafast single photons in pure quantum states". In: *Physical Review Letters* 100.13 (2008), p. 133601.

[136] Sercan Ö Arık and Joseph M Kahn. "Coupled-core multi-core fibers for spatial multiplexing". In: *IEEE Photonics Technology Letters* 25.21 (2013), pp. 2054–2057.

[137] Andrew Wood, Yongmin Jung, and David J Richardson. "Multiport fiber optic beam splitters for space division multiplexed (SDM) systems". In: *IEEE Photonics Technology Letters* 32.13 (2020), pp. 795–798.

[138] Xinyu Wang et al. "Chip-based high-dimensional optical neural network". In: *Nano-Micro Letters* 14.1 (2022), p. 221.

[139] JG Rarity and PR Tapster. "Quantum interference: experiments and applications". In: *Philosophical Transactions of the Royal Society of London. Series A: Mathematical, Physical and Engineering Sciences* 355.1733 (1997), pp. 2267–2277.

[140] AR McMillan et al. "Two-photon interference between disparate sources for quantum networking". In: *Scientific reports* 3.1 (2013), p. 2032.

[141] DA Jackson, Anthony Dandridge, and Sang K Sheem. "Measurement of small phase shifts using a single-mode optical-fiber interferometer". In: *Optics Letters* 5.4 (1980), pp. 139–141.

[142] Leo Yu et al. "Two-photon interference at telecom wavelengths for time-bin-encoded single photons from quantum-dot spin qubits". In: *Nature Communications* 6.1 (2015), p. 8955.

[143] Osamu Shimakawa et al. "Connector type fan-out device for multi-core fiber". In: *SEI Technical Review* 77 (2013), pp. 23–28.

[144] Antonios Perperidis et al. "Characterization and modelling of inter-core coupling in coherent fiber bundles". In: *Optics Express* 25.10 (2017), pp. 11932–11953.

[145] Dong Yan et al. "Observation of split evanescent field distributions in tapered multicore fibers for multiline nanoparticle trapping and microsensing". In: *Optics Express* 29.6 (2021), pp. 9532–9543.

[146] H. A. Haus. *Waves and Fields in Optoelectronics*. Englewood Cliffs, NJ: Prentice-Hall, 1984.

[147] A. Yariv. "Coupled-mode theory for guided-wave optics". In: *IEEE Journal of Quantum Electronics* 9.9 (1973), pp. 919–933. DOI: 10.1109/JQE.1973.1077767.

[148] D. Marcuse. *Theory of Dielectric Optical Waveguides*. 2nd ed. San Diego: Academic Press, 1991.

[149] P Shlichta. "Higher-dimensional Hadamard matrices". In: *IEEE Transactions on Information Theory* 25.5 (1979), pp. 566–572.

[150] Christophe Couteau. “Spontaneous parametric down-conversion”. In: *Contemporary Physics* 59.3 (2018), pp. 291–304.

[151] SP Walborn and CH Monken. “Transverse spatial entanglement in parametric down-conversion”. In: *Physical Review A—Atomic, Molecular, and Optical Physics* 76.6 (2007), p. 062305.

[152] JG Rarity et al. “Two-photon interference in a Mach-Zehnder interferometer”. In: *Physical review letters* 65.11 (1990), p. 1348.

[153] Chandra M Natarajan, Michael G Tanner, and Robert H Hadfield. “Superconducting nanowire single-photon detectors: physics and applications”. In: *Superconductor science and technology* 25.6 (2012), p. 063001.

[154] R. S. Luis et al. “1 02 Petabit/s Transmission Over 1,808.1 km in a 19-Core Randomly-Coupled Multicore Fiber”. In: *Optical Fiber Communication Conference (OFC) Postdeadline Papers 2025*. Optica Publishing Group, 2025, Th4A.1. DOI: 10.1364/OFC.2025.Th4A.1. URL: https://opg.optica.org/abstract.cfm?URI=OFC-2025-Th4A.1.

[155] Arni F Alfredsson et al. “On the performance of joint-core carrier-phase estimation in the presence of intercore skew”. In: *Journal of Lightwave Technology* 37.20 (2019), pp. 5291–5298.

[156] Jiaqi Cai et al. “On the Impact of Inter-Core Skew on Multiple-Span Coupled-Core MCF Transmissions”. In: *2024 Asia Communications and Photonics Conference (ACP) and International Conference on Information Photonics and Optical Communications (IPOC)*. IEEE. 2024, pp. 1–4.

[157] Hitoshi Takeshita et al. “Demonstration of Uncoupled 4-Core Multicore Fiber in Submarine Cable Prototype With Integrated Multicore EDFA”. In: *Journal of Lightwave Technology* 41.3 (2023), pp. 980–988. DOI: 10.1109/JLT.2022.3195190.

[158] Yingyu Chen et al. “High-capacity optical communication relayed by multi-core amplifier on deployed submarine seven-core fiber cable”. en. In: *Communications Engineering* (Apr. 2026). ISSN: 2731-3395. DOI: 10.1038/s44172-026-00664-x. URL: https://www.nature.com/articles/s44172-026-00664-x.

[159] Tetsuya Nakanishi et al. “Advancements in Key Technological Building Blocks for Enabling MCF Implementation”. In: *Optical Fiber Communication Conference (OFC) 2024*. Optica Publishing Group, 2024, W4J.1. DOI: 10.1364/OFC.2024.W4J.1. URL: https://opg.optica.org/abstract.cfm?URI=OFC-2024-W4J.1.

[160] E.S. Gómez et al. “Multidimensional Entanglement Generation with Multicore Optical Fibers”. In: *Phys. Rev. Appl.* 15 (3 Mar. 2021), p. 034024. DOI: 10.1103/PhysRevApplied.15.034024. URL: https://link.aps.org/doi/10.1103/PhysRevApplied.15.034024.

[161] Evelyn A. Ortega et al. “Experimental Space-Division Multiplexed Polarization-Entanglement Distribution through 12 Paths of a Multicore Fiber”. In: *PRX Quantum* 2 (4 Dec. 2021), p. 040356. DOI: 10.1103/

PRXQuantum.2.040356. URL: https://link.aps.org/doi/10.1103/PRXQuantum.2.040356.
[162] G. Cañas et al. "High-dimensional decoy-state quantum key distribution over multicore telecommunication fibers". In: *Phys. Rev. A* 96 (2 Aug. 2017), p. 022317. DOI: 10.1103/PhysRevA.96.022317. URL: https://link.aps.org/doi/10.1103/PhysRevA.96.022317.
[163] J. F. Dynes et al. "Quantum key distribution over multicore fiber". In: *Opt. Express* 24.8 (Apr. 2016), pp. 8081–8087. DOI: 10.1364/OE.24.008081. URL: https://opg.optica.org/oe/abstract.cfm?URI=oe-24-8-8081.
[164] Takuma Nakamura et al. "Sub-femtosecond stabilization of multicore fiber for high-fidelity quantum networking at 100% duty cycle". In: *APL Photonics* 11.2 (Feb. 2026), p. 026113. ISSN: 2378-0967. DOI: 10.1063/5.0308068. eprint: https://pubs.aip.org/aip/app/article-pdf/doi/10.1063/5.0308068/20912603/026113_1_5.0308068.pdf. URL: https://doi.org/10.1063/5.0308068.
[165] Hee Jung Lee, Eunjoo Lee, and Hee Su Park. "Azimuth-rotated splicings of a four-core optical fiber for inter-core group delay compensation". In: *IEEE Photonics Technology Letters* 29.24 (2017), pp. 2250–2253.
[166] Florian Azendorf et al. "Group delay measurements of multicore fibers with correlation optical time domain reflectometry". In: *2020 22nd International Conference on Transparent Optical Networks (ICTON)*. IEEE. 2020, pp. 1–4.
[167] Linqi Jin et al. "Measurement of differential mode group delay in few-mode fiber with correlation optical time-domain reflectometer". In: *Applied Optics* 61.13 (2022), pp. 3579–3582.
[168] Hee Jung Lee et al. "Multi-core fiber interferometer using spatial light modulators for measurement of the inter-core group index differences". In: *Optics Express* 23.10 (2015), pp. 12555–12561.
[169] G. H. Aguilar et al. "Robust Interferometric Sensing Using Two-Photon Interference". In: *Phys. Rev. Appl.* 14 (2 Aug. 2020), p. 024028. DOI: 10.1103/PhysRevApplied.14.024028. URL: https://link.aps.org/doi/10.1103/PhysRevApplied.14.024028.
[170] Pierre Aboussouan et al. "High-visibility two-photon interference at a telecom wavelength using picosecond-regime separated sources". In: *Physical Review A—Atomic, Molecular, and Optical Physics* 81.2 (2010), p. 021801.
[171] Bahaa EA Saleh and Malvin Carl Teich. *Fundamentals of photonics, 2 volume set*. john Wiley & sons, 2019.
[172] C. D. Poole and R. E. Wagner. "Phenomenological approach to polarisation dispersion in long single-mode fibres". In: *Electronics Letters* 22.19 (1986), pp. 1029–1030. DOI: 10.1049/el:19860704.
[173] C. D. Poole. "Statistical treatment of polarization dispersion in single-mode fiber". In: *Optics Letters* 13.8 (1988), pp. 687–689. DOI: 10.1364/OL.13.000687.
[174] Kenneth M. Jordan, Romain A. Abrahao, and Jeff S. Lundeen. "Quantum metrology timing limits of the Hong–Ou–Mandel interferometer and of

general two-photon measurements". In: *Physical Review A* 106.6 (2022), p. 063715. DOI: 10.1103/PhysRevA.106.063715.

[175] Steven M. Kay. *Fundamentals of Statistical Signal Processing, Volume I: Estimation Theory*. Englewood Cliffs, NJ: Prentice Hall, 1993.

[176] Fibercore (Humanetics Group). *SM-4C1500(8.0/125)/001 Four-core Single-mode Fiber Datasheet*. https://fibercore.humaneticsgroup.com/products/multicore-fiber/multicore-fiber/sm-4c150080125001. Operating wavelength 1520–1650 nm; 4-core square arrangement; 50 μm core spacing; 125 μm cladding. 2024.

[177] J Cariñe et al. "Maximizing quantum discord from interference in multi-port fiber beamsplitters". In: *npj Quantum Information* 7.1 (2021), p. 172.

[178] Benjamin J Puttnam et al. "Inter-core skew measurements in temperature controlled multi-core fiber". In: *Optical Fiber Communication Conference*. Optica Publishing Group. 2018, Tu3B–3.

[179] BJ Puttnam et al. "Impact of temperature on propagation time and inter-core skew in a 19-core fiber". In: *Asia Communications and Photonics Conference*. Optica Publishing Group. 2018, S3K–4.

[180] Antonio Acin, Nicolas Gisin, and Lluis Masanes. "From Bell's theorem to secure quantum key distribution". In: *Physical review letters* 97.12 (2006), p. 120405.

[181] Rotem Arnon-Friedman et al. "Practical device-independent quantum cryptography via entropy accumulation". In: *Nature communications* 9.1 (2018), p. 459.

[182] John S Bell. "On the einstein podolsky rosen paradox". In: *Physics Physique Fizika* 1.3 (1964), p. 195.

[183] John F Clauser et al. "Proposed experiment to test local hidden-variable theories". In: *Physical review letters* 23.15 (1969), p. 880.

[184] Víctor Zapatero et al. "Advances in device-independent quantum key distribution". In: *npj quantum information* 9.1 (2023), p. 10.

[185] Charles H Bennett and Gilles Brassard. "Quantum cryptography: Public key distribution and coin tossing". In: *Theoretical computer science* 560 (2014), pp. 7–11.

[186] Artur K. Ekert. "Quantum cryptography based on Bell's theorem". In: *Physical Review Letters* 67 (6 Aug. 1991), pp. 661–663. DOI: 10.1103/PhysRevLett.67.661. URL: https://link.aps.org/doi/10.1103/PhysRevLett.67.661.

[187] Bas Hensen et al. "Loophole-free Bell inequality violation using electron spins separated by 1.3 kilometres". In: *Nature* 526.7575 (2015), pp. 682–686.

[188] Marek Żukowski et al. ""Event-ready-detectors"Bell experiment via entanglement swapping". In: *Physical review letters* 71.26 (1993), p. 4287.

[189] Xingjian Zhang et al. "Quantum complementarity approach to device-independent security". In: *Physical Review Letters* 131.14 (2023), p. 140801.

[190] Bo-Wei Lu et al. "Device-independent quantum key distribution over 100 km with single atoms". In: *Science* 391.6785 (2026), pp. 592–597.

[191] Valerio Scarani et al. “The security of practical quantum key distribution”. In: *Rev. Mod. Phys.* 81 (3 Sept. 2009), pp. 1301–1350. DOI: 10.1103/RevModPhys.81.1301. URL: https://link.aps.org/doi/10.1103/RevModPhys.81.1301.

[192] Peter W Shor and John Preskill. “Simple proof of security of the BB84 quantum key distribution protocol”. In: *Physical review letters* 85.2 (2000), p. 441.

[193] Nicolas Gisin et al. “Quantum cryptography”. In: *Rev. Mod. Phys.* 74 (1 Mar. 2002), pp. 145–195. DOI: 10.1103/RevModPhys.74.145. URL: https://link.aps.org/doi/10.1103/RevModPhys.74.145.

[194] Lars Lydersen et al. “Hacking commercial quantum cryptography systems by tailored bright illumination”. In: *Nature photonics* 4.10 (2010), pp. 686–689.

[195] Yi Zhao et al. “Quantum hacking: Experimental demonstration of time-shift attack against practical quantum-key-distribution systems”. In: *Physical Review A—Atomic, Molecular, and Optical Physics* 78.4 (2008), p. 042333.

[196] Feihu Xu et al. “Secure quantum key distribution with realistic devices”. In: *Reviews of modern physics* 92.2 (2020), p. 025002.

[197] Hoi-Kwong Lo, Marcos Curty, and Bing Qi. “Measurement-Device-Independent Quantum Key Distribution”. In: *Physical Review Letters* 108 (2012), p. 130503. DOI: 10.1103/PhysRevLett.108.130503.

[198] Feihu Xu et al. “Measurement-Device-Independent Quantum Cryptography”. In: *IEEE Journal of Selected Topics in Quantum Electronics* 21.3 (2015). arXiv:1409.5157, p. 6601111.

[199] Lars Lydersen et al. “Hacking Commercial Quantum Cryptography Systems by Tailored Bright Illumination”. In: *Nature Photonics* 4 (2010), pp. 686–689. DOI: 10.1038/nphoton.2010.214.

[200] Won-Young Hwang. “Quantum Key Distribution with High Loss: Toward Global Secure Communication”. In: *Physical Review Letters* 91 (2003), p. 057901. DOI: 10.1103/PhysRevLett.91.057901.

[201] Hoi-Kwong Lo, Xiongfeng Ma, and Kai Chen. “Decoy State Quantum Key Distribution”. In: *Physical Review Letters* 94 (2005), p. 230504. DOI: 10.1103/PhysRevLett.94.230504.

[202] Qiang Zhang et al. “Large Scale Quantum Key Distribution: Challenges and Solutions”. In: *Optics Express* 26 (2018), p. 24260.

[203] Marcos Curty. “Towards High-Performance Quantum Key Distribution with Implementation Security”. In: *SPIE Proceedings*. 2020.

[204] Dominic Mayers and Andrew Yao. “Self testing quantum apparatus”. In: *Quantum Inf. Comput.* 4.273–286 (2004). DOI: 10.48550/arXiv.quant-ph/0307205.

[205] Robert W. Spekkens Giulio Chiribella. *Quantum Theory: Informational Foundations and Foils*. Ed. by Springer. Springer Netherlands, 2016. ISBN: 9789401773034. DOI: 10.1007/978-94-017-7303-4.

[206] D. P. Nadlinger et al. “Experimental quantum key distribution certified by Bell’s theorem”. In: *Nature* 607.7920 (July 2022), pp. 682–686. ISSN: 1476-4687. DOI: 10.1038/s41586-022-04941-5.

[207] Wen-Zhao Liu et al. "Toward a Photonic Demonstration of Device-Independent Quantum Key Distribution". In: *Physical Review Letters* 129.5 (July 2022), p. 050502. ISSN: 1079-7114. DOI: 10.1103/physrevlett.129.050502.

[208] Wei Zhang et al. "A device-independent quantum key distribution system for distant users". In: *Nature* 607.7920 (July 2022), pp. 687–691. ISSN: 1476-4687. DOI: 10.1038/s41586-022-04891-y.

[209] Wenhan Yan et al. "A measurement-device-independent quantum key distribution network using optical frequency comb". In: *npj Quantum Information* 11.1 (2025), p. 97.

[210] Shan-Feng Shao et al. "High-rate measurement-device-independent quantum communication without optical reference light". In: *Physical Review X* 15.2 (2025), p. 021066.

[211] Wei Li et al. "Twin-field quantum key distribution without phase locking". In: *Physical Review Letters* 130.25 (2023), p. 250802.

[212] Lai Zhou et al. "Experimental quantum communication overcomes the rate-loss limit without global phase tracking". In: *Physical Review Letters* 130.25 (2023), p. 250801.

[213] Yang Liu et al. "1002 km twin-field quantum key distribution with finite-key analysis". In: *Quantum Frontiers* 2.1 (2023), p. 16.

[214] Likang Zhang et al. "Experimental mode-pairing quantum key distribution surpassing the repeaterless bound". In: *Physical Review X* 15.2 (2025), p. 021037.

[215] Adnan A E Hajomer, Ulrik L Andersen, and Tobias Gehring. "High-rate continuous-variable measurement device-independent quantum key distribution with finite-size security". In: *Quantum Science and Technology* 10.2 (Feb. 2025), p. 025032. DOI: 10.1088/2058-9565/adb2be. URL: https://dx.doi.org/10.1088/2058-9565/adb2be.

[216] Jingyang Liu et al. "Hybrid Implementation for Untrusted-node-based Quantum Key Distribution Network". In: *arXiv preprint arXiv:2503.05095* (2025).

[217] Mirko Pittaluga et al. "Long-distance coherent quantum communications in deployed telecom networks". In: *Nature* 640.8060 (2025), pp. 911–917.

[218] Mihály Héder. "From NASA to EU: the evolution of the TRL scale in Public Sector Innovation". In: *The Innovation Journal* 22.2 (Sept. 2017), pp. 1–23. URL: https://innovation.cc/document/2017-22-2-3-from-nasa-to-eu-the-evolution-of-the-trl-scale-in-public-sector-innovation/.

[219] Nicolas Brunner et al. "Bell Nonlocality". In: *Reviews of Modern Physics* 86 (2014), pp. 419–478. DOI: 10.1103/RevModPhys.86.419.

[220] Stefano Pironio et al. "Random Numbers Certified by Bell's Theorem". In: *Nature* 464 (2010), pp. 1021–1024. DOI: 10.1038/nature09008.

[221] Boris S. Tsirelson. "Quantum Generalizations of Bell's Inequality". In: *Letters in Mathematical Physics* 4 (1980), pp. 93–100. DOI: 10.1007/BF00417500.

[222] Valerio Scarani. "The Device-Independent Outlook on Quantum Physics". In: *Acta Physica Slovaca* 62 (2012), pp. 347–409.

[223] Renato Renner. "Security of Quantum Key Distribution". In: *International Journal of Quantum Information* 6.1 (2008), pp. 1–127. DOI: 10.1142/S0219749908003256.

[224] Frédéric Dupuis, Omar Fawzi, and Renato Renner. "Entropy Accumulation". In: *Communications in Mathematical Physics* 379 (2020), pp. 867–913. DOI: 10.1007/s00220-020-03839-5.

[225] Marco Tomamichel and Renato Renner. "Uncertainty Relation for Smooth Entropies". In: *Physical Review Letters* 106 (2011), p. 110506. DOI: 10.1103/PhysRevLett.106.110506.

[226] Charles H. Bennett et al. "Generalized Privacy Amplification". In: *IEEE Transactions on Information Theory* 41.6 (1995), pp. 1915–1923. DOI: 10.1109/18.476316.

[227] Philip M. Pearle. "Hidden-Variable Example Based upon Data Rejection". In: *Physical Review D* 2 (1970), pp. 1418–1425. DOI: 10.1103/PhysRevD.2.1418.

[228] Anupam Garg and N. David Mermin. "Detector Inefficiencies in the Einstein-Podolsky-Rosen Experiment". In: *Physical Review D* 35 (1987), pp. 3831–3835. DOI: 10.1103/PhysRevD.35.3831.

[229] Philippe H. Eberhard. "Background Level and Counter Efficiencies Required for a Loophole-Free Einstein-Podolsky-Rosen Experiment". In: *Physical Review A* 47 (1993), R747–R750. DOI: 10.1103/PhysRevA.47.R747.

[230] Valerio Scarani et al. "The Security of Practical Quantum Key Distribution". In: *Reviews of Modern Physics* 81 (2009), pp. 1301–1350. DOI: 10.1103/RevModPhys.81.1301.

[231] Jonathan Barrett, Lucien Hardy, and Adrian Kent. "No Signaling and Quantum Key Distribution". In: *Physical Review Letters* 95 (2005), p. 010503. DOI: 10.1103/PhysRevLett.95.010503.

[232] Paul G. Kwiat et al. "New High-Intensity Source of Polarization-Entangled Photon Pairs". In: *Phys. Rev. Lett.* 75 (1995), p. 4337. DOI: 10.1103/PhysRevLett.75.4337.

[233] Paul G. Kwiat et al. "Ultrabright source of polarization-entangled photons". In: *Phys. Rev. A.* 60 (1999), R773. DOI: 10.1103/PhysRevA.60.R773.

[234] S.J. Freedman and J.F. Clauser. "Experimental Test of Local Hidden-Variable Theories". In: *Phys. Rev. Lett.* 28 (1972), p. 938. DOI: 10.1103/PhysRevLett.28.938.

[235] S. Gómez et al. "Experimental investigation of partially entangled states for device-independent randomness generation and self-testing protocols". In: *Phys. Rev. A* 99 (3 Mar. 2019), p. 032108. DOI: 10.1103/PhysRevA.99.032108. URL: https://link.aps.org/doi/10.1103/PhysRevA.99.032108.

[236] Sandra Meraner et al. "Approaching the Tsirelson bound with a Sagnac source of polarization-entangled photons". In: *SciPost Phys.* 10 (2021), p. 017. DOI: 10.21468/SciPostPhys.10.1.017.

[237] Olavo Cosme et al. "Hong-Ou-Mandel interferometer with one and two photon pairs". In: *Physical Review A* 77 (5 May 2008), p. 053822. DOI: 10.1103/PhysRevA.77.053822. URL: https://link.aps.org/doi/10.1103/PhysRevA.77.053822.

[238] Yoshiaki Tsujimoto et al. "Optimal conditions for the Bell test using spontaneous parametric down-conversion sources". In: *Phys. Rev. A* 98 (6 Dec. 2018), p. 063842. DOI: 10.1103/PhysRevA.98.063842. URL: https://link.aps.org/doi/10.1103/PhysRevA.98.063842.

[239] M. Ho et al. "Noisy Preprocessing Facilitates a Photonic Realization of Device-Independent Quantum Key Distribution". In: *Physical Review Letters* 124.23 (June 2020), p. 230502. ISSN: 1079-7114. DOI: 10.1103/physrevlett.124.230502.

[240] H. J. Kimble. "The Quantum Internet". In: *Nature* 453 (2008), pp. 1023–1030. DOI: 10.1038/nature07127.

[241] Stephanie Wehner, David Elkouss, and Ronald Hanson. "Quantum Internet: A Vision for the Road Ahead". In: *Science* 362.6412 (2018). DOI: 10.1126/science.aam9288.

[242] David D. Awschalom et al. "Quantum Technologies with Optically Interfaced Solid-State Spins". In: *Nature Photonics* 12 (2018), pp. 516–527. DOI: 10.1038/s41566-018-0232-2.

[243] Jacob P. Covey, Harald Weinfurter, and Hannes Bernien. "Quantum networks with neutral atom processing nodes". In: *npj Quantum Information* 9.1 (2023), p. 90. DOI: 10.1038/s41534-023-00759-9.

[244] Nicolas Sangouard et al. "Quantum Repeaters Based on Atomic Ensembles and Linear Optics". In: *Reviews of Modern Physics* 83 (2011), pp. 33–80. DOI: 10.1103/RevModPhys.83.33.

[245] Felix Mann et al. "Low-noise quantum frequency conversion in a monolithic cavity with bulk periodically poled potassium titanyl phosphate". In: *Phys. Rev. Appl.* 20 (5 Nov. 2023), p. 054010. DOI: 10.1103/PhysRevApplied.20.054010. URL: https://link.aps.org/doi/10.1103/PhysRevApplied.20.054010.

[246] Jan Fabian Geus et al. "Low-noise short-wavelength pumped frequency downconversion for quantum frequency converters". In: *Optica Quantum* 2.3 (June 2024), pp. 189–195. DOI: 10.1364/OPTICAQ.515769.

[247] Arian J. Stolk et al. "Metropolitan-scale heralded entanglement of solid-state qubits". In: *Science Advances* 10.44 (2024). Open Access, eadp6442. ISSN: 2375-2548. DOI: 10.1126/sciadv.adp6442.

[248] Yong Yu et al. "Entanglement of two quantum memories via fibres over dozens of kilometres". In: *Nature* 578.7794 (2020), pp. 240–245. DOI: 10.1038/s41586-020-1976-7. URL: https://doi.org/10.1038/s41586-020-1976-7.

[249] Tim van Leent et al. "Entangling single atoms over 33 km telecom fibre". In: *Nature* 607.7917 (2022), pp. 69–73. DOI: 10.1038/s41586-022-04764-4. URL: https://doi.org/10.1038/s41586-022-04764-4.

[250] Xi-Yu Luo et al. "Postselected Entanglement between Two Atomic Ensembles Separated by 12.5 km". In: *Phys. Rev. Lett.* 129 (5 July 2022),

p. 050503. DOI: 10.1103/PhysRevLett.129.050503. URL: https://link.aps.org/doi/10.1103/PhysRevLett.129.050503.

[251] Hiroki Takesue and Benjamin Miquel. "Entanglement swapping using telecom-band photons generated in fibers". In: *Opt. Express* 17.13 (June 2009), pp. 10748–10756. DOI: 10.1364/OE.17.010748. URL: https://opg.optica.org/oe/abstract.cfm?URI=oe-17-13-10748.

[252] J. Jin et al. "Entanglement swapping with quantum-memory-compatible photons". In: *Phys. Rev. A* 92 (1 July 2015), p. 012329. DOI: 10.1103/PhysRevA.92.012329. URL: https://link.aps.org/doi/10.1103/PhysRevA.92.012329.

[253] Qi-Chao Sun et al. "Entanglement swapping over 100 km optical fiber with independent entangled photon-pair sources". In: *Optica* 4.10 (Oct. 2017), pp. 1214–1218. DOI: 10.1364/OPTICA.4.001214. URL: https://opg.optica.org/optica/abstract.cfm?URI=optica-4-10-1214.

[254] Farid Samara et al. "Entanglement swapping between independent and asynchronous integrated photon-pair sources". In: *Quantum Science and Technology* 6.4 (2021), p. 045024. DOI: 10.1088/2058-9565/abf599. URL: https://doi.org/10.1088/2058-9565/abf599.

[255] Klaus Mattle et al. "Dense Coding in Experimental Quantum Communication". In: *Phys. Rev. Lett.* 76 (1996), p. 4656. DOI: 10.1103/PhysRevLett.76.4656.

[256] R. Stockill et al. "Phase-Tuned Entangled State Generation between Distant Spin Qubits". In: *Phys. Rev. Lett.* 119 (1 July 2017), p. 010503. DOI: 10.1103/PhysRevLett.119.010503. URL: https://link.aps.org/doi/10.1103/PhysRevLett.119.010503.

[257] Peter C. Humphreys et al. "Deterministic delivery of remote entanglement on a quantum network". In: *Nature* 558.7709 (2018), pp. 268–273. DOI: 10.1038/s41586-018-0200-5. URL: https://doi.org/10.1038/s41586-018-0200-5.

[258] M. Pompili et al. "Realization of a multinode quantum network of remote solid-state qubits". In: *Science* 372.6539 (2021), pp. 259–264. DOI: 10.1126/science.abg1919. eprint: https://www.science.org/doi/pdf/10.1126/science.abg1919. URL: https://www.science.org/doi/abs/10.1126/science.abg1919.

[259] S L N Hermans et al. "Entangling remote qubits using the single-photon protocol: an in-depth theoretical and experimental study". In: *New Journal of Physics* 25.1 (Jan. 2023), p. 013011. DOI: 10.1088/1367-2630/acb004. URL: https://dx.doi.org/10.1088/1367-2630/acb004.

[260] A. J. Stolk et al. *Extendable optical phase synchronization of remote and independent quantum network nodes over deployed fibers*. 2024. arXiv: 2408.12464 [quant-ph]. URL: https://arxiv.org/abs/2408.12464.

[261] Dario Lago-Rivera et al. "Telecom-heralded entanglement between multimode solid-state quantum memories". In: *Nature* 594.7861 (2021), pp. 37–40. DOI: 10.1038/s41586-021-03481-8.

[262] Xiao Liu et al. "Heralded entanglement distribution between two absorptive quantum memories". In: *Nature* 594.7861 (2021), pp. 41–45. DOI: 10.1038/s41586-021-03505-3.

[263] Stephan Kucera et al. "Demonstration of quantum network protocols over a 14-km urban fiber link". In: *npj Quantum Information* 10.1 (2024), p. 88. DOI: 10.1038/s41534-024-00886-x. URL: https://doi.org/10.1038/s41534-024-00886-x.

[264] Nicolas Gisin, Stefano Pironio, and Nicolas Sangouard. "Proposal for implementing device-independent quantum key distribution based on a heralded qubit amplifier". In: *Physical review letters* 105.7 (2010), p. 070501. DOI: 10.1103/PhysRevLett.105.070501.

[265] Marcos Curty and Tobias Moroder. "Heralded-qubit amplifiers for practical device-independent quantum key distribution". In: *Physical Review A* 84.1 (2011), p. 010304. DOI: 10.1103/PhysRevA.84.010304.

[266] David Pitkanen et al. "Efficient heralding of photonic qubits with applications to device-independent quantum key distribution". In: *Phys. Rev. A* 84 (2 Aug. 2011), p. 022325. DOI: 10.1103/PhysRevA.84.022325. URL: https://link.aps.org/doi/10.1103/PhysRevA.84.022325.

[267] Evan Meyer-Scott et al. "Entanglement-based linear-optical qubit amplifier". In: *Phys. Rev. A* 88 (1 July 2013), p. 012327. DOI: 10.1103/PhysRevA.88.012327. URL: https://link.aps.org/doi/10.1103/PhysRevA.88.012327.

[268] T. C. Ralph and A. P. Lund. "Nondeterministic Noiseless Linear Amplification of Quantum Systems". In: *AIP Conference Proceedings* 1110.1 (Apr. 2009), pp. 155–160. DOI: 10.1063/1.3131295. eprint: https://pubs.aip.org/aip/acp/article-pdf/1110/1/155/11396998/155_1_online.pdf. URL: https://doi.org/10.1063/1.3131295.

[269] Víctor Zapatero and Marcos Curty. "Long-distance device-independent quantum key distribution". In: *Scientific Reports* 9.1 (2019), p. 17749. DOI: 10.1038/s41598-019-53803-0. URL: https://doi.org/10.1038/s41598-019-53803-0.

[270] Hans K.C. Beukers et al. "Remote-Entanglement Protocols for Stationary Qubits with Photonic Interfaces". In: *PRX Quantum* 5 (1 Mar. 2024), p. 010202. DOI: 10.1103/PRXQuantum.5.010202. URL: https://link.aps.org/doi/10.1103/PRXQuantum.5.010202.

[271] J.S. Bell. "Atomic-cascade photons and quantum-mechanical nonlocality". In: *Comments Atom. Mol. Phys.* 9 (1980), pp. 121–126. DOI: 10.1142/9789812795854_0082.

[272] Christoph Simon and William T. M. Irvine. "Robust Long-Distance Entanglement and a Loophole-Free Bell Test with Ions and Photons". In: *Phys. Rev. Lett.* 91 (11 Sept. 2003), p. 110405. DOI: 10.1103/PhysRevLett.91.110405. URL: https://link.aps.org/doi/10.1103/PhysRevLett.91.110405.

[273] Harald Weinfurter. "Experimental Bell-State Analysis". In: *Europhysics Letters* 25 (1994), pp. 559–564. DOI: 10.1209/0295-5075/25/8/001.

[274] Samuel L. Braunstein, Andrew Mann, and Mordecai Revzen. "Maximal Violation of Bell Inequalities for Mixed States". In: *Physical Review Letters* 68 (1992), pp. 3259–3261.

[275] Leonard Mandel. "Coherence and Indistinguishability". In: *Optics Letters* 16 (1991), pp. 1882–1883.

[276] Thomas Legero et al. "Time-Resolved Two-Photon Quantum Interference". In: *Physical Review Letters* 93 (2004), p. 070503. DOI: 10.1103/PhysRevLett.93.070503.

[277] Jian-Wei Pan et al. "Experimental Entanglement Swapping: Entangling Photons That Never Interacted". In: *Physical Review Letters* 80 (1998), pp. 3891–3894. DOI: 10.1103/PhysRevLett.80.3891.

[278] M. Halder and et al. "Entangling Independent Photons by Time Measurement". In: *Nature Physics* 3 (2007), pp. 692–695. DOI: 10.1038/nphys741.

[279] C. X. Zhang et al. "Research Progress in Quantum Key Distribution". In: *Chinese Physics B* 32 (2023). DOI: 10.1088/1674-1056/acfd16.

[280] Francesco Marsili et al. "Detecting Single Infrared Photons with 93% System Efficiency". In: *Nature Photonics* 7 (2013), pp. 210–214. DOI: 10.1038/nphoton.2013.13.

[281] M. Geng. "Advances of Quantum Key Distribution and Network Nonlocality". In: *Entropy* 27 (2025). URL: https://pmc.ncbi.nlm.nih.gov/articles/PMC12468356/.